

THE UNIVERSITY OF CALGARY

Intensity Modulated Optical Fiber Flowmeter

by

Ahmed Hisham E. A. Morshed

A THESIS

SUBMITTED TO THE FACULTY OF GRADUATE STUDIES
IN PARTIAL FULFILLMENT OF THE REQUIREMENTS FOR THE
DEGREE OF MASTER OF SCIENCE

DEPARTMENT OF ELECTRICAL AND COMPUTER ENGINEERING

CALGARY, ALBERTA

APRIL, 1992

© Ahmed Hisham E. A. Morshed 1992



National Library
of Canada

Bibliothèque nationale
du Canada

Canadian Theses Service Service des thèses canadiennes

Ottawa, Canada
K1A 0N4

The author has granted an irrevocable non-exclusive licence allowing the National Library of Canada to reproduce, loan, distribute or sell copies of his/her thesis by any means and in any form or format, making this thesis available to interested persons.

The author retains ownership of the copyright in his/her thesis. Neither the thesis nor substantial extracts from it may be printed or otherwise reproduced without his/her permission.

L'auteur a accordé une licence irrévocable et non exclusive permettant à la Bibliothèque nationale du Canada de reproduire, prêter, distribuer ou vendre des copies de sa thèse de quelque manière et sous quelque forme que ce soit pour mettre des exemplaires de cette thèse à la disposition des personnes intéressées.

L'auteur conserve la propriété du droit d'auteur qui protège sa thèse. Ni la thèse ni des extraits substantiels de celle-ci ne doivent être imprimés ou autrement reproduits sans son autorisation.

ISBN 0-315-75145-2

Canada

THE UNIVERSITY OF CALGARY
FACULTY OF GRADUATE STUDIES

The undersigned certify that they have read, and recommend to the Faculty of Graduate Studies for acceptance, a thesis entitled, "Intensity Modulated Optical Fiber Flowmeter" submitted by Ahmed Hisham E. A. Morshed in partial fulfillment of the requirements for the degree of Master of Science.

David Irvine - Halliday

Supervisor, Dr. D. Irvine - Halliday,
Department of Electrical and Comp. Engg.

Ronald H. Johnston

Dr. R. H. Johnston,
Department of Electrical and Comp. Engg.

Michel Fattouche

Dr. M. Fattouche,
Department of Electrical and Comp. Engg.

W. Svrcek

Dr. W. Y. Svrcek,
Department of Chemical and Petroleum
Engineering

Date 20 April 92

Abstract

Intensity-modulated optical fiber sensing of fluid flow rate was studied. Experimental investigations were carried out using a home-made flow rig. Measurement of flow rate by a vortex shedding optical fiber sensor was achieved using fiber tapers to detect the vortex shedding frequency.

Single-mode optical fiber tapers were made using available equipments and characterized for their bending loss at two different operating wavelengths where they act as multimode and single-mode light guides. These tapers were studied theoretically and modeled for their transmission-versus-bending characteristics. Results of the computations were compared to bending loss characteristics obtained experimentally and to data published in the literature.

Fiber tapers were installed in a prototype vortex shedding meter where they act either as shedding struts or secondary sensing struts. Both configurations were investigated under multimode and single-mode operation. The proposed vortex shedding meter was experimentally studied and proved feasible.

Acknowledgments

The author would like to express his gratitude to his research supervisor Dr. Dave Irvine - Halliday for advice and encouragement throughout this work. He is grateful to Dr. William Svrcek for his helpful advice on the design of the flow rig used in experimental investigations and to Dr. Rubert Streets for advice on using the Structural Dynamics Analyser.

He is thankful to the technical staff at the Faculty of Engineering for their help on many occasions during the experimental investigations particularly to Mr. Garry Harrington for making the flow rig, Mr. Larry Dornan for providing help with the choice and operation of the rotameter and Mr. Donn Anson for assistance in the rig calibration. He is also thankful to Northern Telecomm and Corning Glass for supplying the optical fibers.

He sincerely acknowledges the assistance and advice of Mr. Bryan Gooding of the Academic Computing Services and the invaluable help of his friends Husam Kinawi of the Computer Science Department and Khaled Elmetwally of the Electrical and Computer Engineering Department with the taper characteristics simulation program. He wishes to once more thank his previous research supervisor, Dr. Mahmoud H. Ahmed of The Electronics and Computer Engineering Dept, Ain Shams University, who helped build the author's background in modal analysis without which a part of this work could not have been completed.

Table of Contents

Thesis approval	ii
Abstract	iii
Acknowledgments	iv
Table of Contents	v
List of Tables	viii
List of Figures	ix
List of Symbols	xv
1. INTRODUCTION	1
2. OPTICAL FIBER INTENSITY AND PHASE SENSORS	4
2.1. Classification of Sensing Schemes	4
2.2. Intrinsic Intensity - and Phase - Modulated Sensors	5
3. FLUID FLOW RATE MEASUREMENT TECHNIQUES	13
3.1. Direct and Differential Pressure Flow Rate Measurement	13
3.2. Point Velocity Measurement Techniques	15
3.3. Average Velocity Measurement Techniques	16

4. OPTICAL FIBER FLOWMETERS	19
4.1. Application of Fibers to Fluid Flowmeters	19
4.2. Vortex Shedding Flowmeters	21
5. INVESTIGATION OF THE DIRECT INTENSITY-MODULATED EFFECTS OF PRESSURE ON OPTICAL FIBERS	26
5.1. Theoretical Estimation of the Change in Effective Refractive Index	27
5.2. Experimental Investigation	34
6. THE VORTEX SHEDDING PROCESS	45
6.1. Vortex Shedding Past an Infinite Circular Cylinder	45
6.2 Effects of Non-Ideal Conditions on Vortex Shedding	49
7. INTENSITY MODULATED FIBRE OPTIC VORTEX SHEDDING FLOWMETER	54
7.1. Optical Fiber Tapers	55
7.2. Theoretical Modeling of Bent Single - Mode Fiber Tapers	68

7.3. Fiber Taper Vortex Shedding Flowmeters	82
7.3.1. Rig Calibration	82
7.3.2. The Fiber Taper as a Shedding Strut	86
7.3.3. The Fiber Taper as a Secondary Strut	103
8. Conclusion	123
References	128
Appendix	137

List of Tables

Table 5.1. Summary of experimental results with the sensor of Fig. 5.2.	38
Table 7.1. Parameters of the single mode fiber used to make tapers	59
Table A.1. Rig calibration data	137

List of Figures

Fig. 2.1. Extrinsic intensity and phase pressure sensors using movable reflective diaphragms	6
Fig. 2.2. Intrinsic intensity and phase acoustic sensors	6
Fig. 2.3. A block diagram of a fiber optic intensity - modulated sensor	7
Fig. 2.4. A block diagram of a fiber optic phase - modulated sensor	7
Fig. 3.1. Differential pressure measurement using a Venturimeter	14
Fig. 3.2. Ultrasonic transit time and Doppler flowmeters	17
Fig. 4.1. A vortex shedding flowmeter using fiber microbends	24
Fig. 4.2. Vortex shedding flowmeters using external optical resonators using confocal mirrors and a fiber Fabry-Perot	24
Fig. 4.3. Intrinsic phase - modulated vortex shedding flowmeter using a single - mode fiber as the shedding strut	25
Fig. 5.1. A schematic and a photo of the flow rig used for experimental investigation	35

Fig. 5.2. A cross-section of the plexiglass test section	36
Fig. 5.3. Spectra of the mechanical and electrical channels with the flow rig turned off	40
Fig. 5.4. Spectra of the mechanical and electrical channels at different pressures and flow rates	42
Fig. 6.1.a. Development of vortex separation past a circular cylinder	47
Fig. 6.1.b. The vortex street	47
Fig. 7.1. The rig used to make fiber tapers	58
Fig. 7.2. Experimental relative transmission versus bending of a fiber taper with 30.48 μm waist diameter, 5.8 mm, and 4.65 mm to the ends of the taper at 633 nm and 1300 nm	61
Fig. 7.3. Experimental relative transmission versus bending of a fiber taper with 86.36 μm waist diameter, 3.22 mm, and 5 mm to the ends of the taper at 633 nm and 1300 nm	62
Fig. 7.4. Experimental relative transmission versus bending of a fiber taper with 28.96 μm waist diameter, 7.6 μm waist length, 5.8 mm, and 4.1 mm to the ends of the taper at 1300 nm	67

Fig. 7.5. Experimental relative transmission versus bending of a fiber taper with 22.86 μm waist diameter, 3 mm waist length, 5.8 mm, and 4.3 mm to the ends of the taper at 1300 nm	67
Fig. 7.6. Step - wise approximation of a bent fiber taper	70
Fig. 7.7. Mixing of local modes at the junction between two sections of a bent taper	71
Fig. 7.8. Relative power as a function of bending angle for a taper with 18.75 μm waist diameter made from a fiber that is single mode at 633 nm	76
Fig. 7.9. Relative transmission and fractional power guided in the modes considered in the analysis - for the taper of Fig. 7.4	77
Fig. 7.10. Relative transmission and fractional power guided in the modes considered in the analysis - for the taper of Fig. 7.5	77
Fig. 7.11. Simulated transmission versus bending characteristics for the fiber taper of Fig. 7.4	81
Fig. 7.12. Simulated transmission versus bending characteristics for the fiber taper of Fig. 7.5	81
Fig. 7.13. Rig calibration chart	84

Fig. 7.14. Reference curves; shedding frequencies as obtained by Roshko's formulae in the laminar range, and the transitional range of vortex shedding	85
Fig. 7.15. Spectra of the intensity modulated signal with a fiber taper of 25.4 μm waist as the shedding strut at 633 nm light wavelength	87
Fig. 7.16. Detected frequency peaks for Fig. 7.15 as compared to the shedding frequencies of a 125 μm strut	90
Fig. 7.17. Spectra of the intensity modulated signal at 1300 nm light wavelength using the same taper as Fig. 7.15	92
Fig. 7.18. Detected frequency peaks for Fig. 7. 17 as compared to the shedding frequencies of a 125 μm strut	95
Fig. 7.19. Spectra of the intensity modulated signal with the same taper of Fig. 7.15 at 633 nm, with a different optical receiver	96
Fig. 7.20. Detected frequency peaks for Fig. 7. 19 as compared to the shedding frequencies of a 125 μm strut	99
Fig. 7.21. Detected frequency peaks with a fiber taper of 40.13 μm waist as the shedding strut at 633 nm light wavelength	101

Fig. 7.22. Detected frequency peaks with a fiber taper of 40.13 μm waist as the shedding strut at 1300 nm light wavelength	101
Fig. 7.23. Spectra of the intensity modulated signal with a fiber taper of 23 μm waist as a secondary strut past a 750 μm primary strut, at 633 nm light wavelength	105
Fig. 7.24. Detected frequency peaks for Fig. 7.23 as compared to the shedding frequencies of 125 μm and 750 μm struts	108
Fig. 7.25. Spectra of the intensity modulated signal with the same taper of Fig. 7.23 as a secondary strut past a 750 μm primary strut, at 1300 nm light wavelength	109
Fig. 7.26. Detected frequency peaks for Fig. 7.25 as compared to the shedding frequencies of 125 μm and 750 μm struts	112
Fig. 7.27. Spectra of the intensity modulated signal with a fiber taper of 29 μm waist as a secondary strut past a 750 μm primary strut, at 633 nm light wavelength	114
Fig. 7.28. Detected frequency peaks for Fig. 7.27 as compared to the shedding frequencies of 125 μm and 750 μm struts	117

Fig. 7.29. Spectra of the intensity modulated signal with the same taper of Fig. 7.27 as a secondary strut past a 750 μm primary strut, at 1300 nm light wavelength 118

Fig. 7.30. Detected frequency peaks for Fig. 7.29 as compared to the shedding frequencies of 125 μm and 750 μm struts 121

Fig. 7.31. Detected primary strut shedding frequencies with four different tapers as secondary struts at both 633 nm and 1300 nm wavelengths as compared to theoretical shedding frequencies 122

Fig. 7.32. Detected frequency peaks with three different fiber tapers as secondary struts at 1300 nm light wavelength as compared to theoretical shedding frequencies of the primary strut 122

List of Symbols

- a core radius ; modal amplitude
- a_v^i the amplitude coefficient of the v th guided mode of the i th taper section
- $[a_v]$ column vectors of a_v
- b normalized propagation constant of the mode ; fiber outer radius
- β propagation constant of the mode
- $C_{\mu\nu}$ coupling coefficient
- $[C]$ coupling coefficients matrix
- D core diameter
- D_{st} diameter of the strut
- d stretch distance
- Δ differential change
- δ incremental bending between the taper sections
- E Young's modulus

E_{co} Young's modulus of the fiber core

E_{cl} Young's modulus of the fiber cladding

E_J Young's modulus of the fiber jacket

e transverse electric field

e_v^i the transverse electric field of the v th guided mode of the i th section

ε strain

ε_1 radial strain

ε_3 axial strain

F the vortex shedding frequency

f ratio of core to cladding radii

Φ the radiation field

ϕ phase angle ; azimuthal coordinate

h transverse magnetic field

I_t resultant intensity

- j the square root of -1.
- k_0 wavenumber in free space
- L path length
- λ_0 the free space wavelength of exciting wave
- M number of guided modes included in model
- μ Poisson's ratio ; modal index
- μ_{co} Poisson's ratio of the core
- μ_{cl} Poisson's ratio of the cladding
- μ_j Poisson's ratio of the fiber jacket
- NA the fiber numerical aperture
- n core refractive index
- n_{eff} effective refractive index for the propagating mode
- n_{cl} the refractive index of the fiber cladding

n_{ext} the refractive index of outer medium

ν Kinematic viscosity ; modal index

P pressure

$[P_{\nu}]$ diagonal matrix of the propagation factors

p_{ν} propagation factor of the ν th mode

p_{11}, p_{12} elements of the strain-optic tensor

θ oblique shedding angle

r radial transverse coordinate

S the Strouhal number

S_{θ} the Strouhal number for oblique shedding

S_t resultant optical signal

T temperature

t time

V normalized frequency of the fiber

V_{cl} normalized frequency of the fiber cladding

v velocity of approach of the fluid

ω angular frequency

X cross product sign

ψ resultant optical phase angle

z axial coordinate

Chapter 1

INTRODUCTION

The development of an optical fiber fluid flowmeter for applications in industrial remote process monitoring and control is a subject that has received considerable attention. Flow meter configurations employing fiber optic sensing of the flow effects have been reported [1-7] and of these, the vortex shedding flowmeters have the potential of low cost, easy fabrication and negligible flow blockage. Those were implemented using phase modulation of the optical signal [4-6] rather than intensity modulation sensing. The complexities of optical phase detection and sophistication of phase detection schemes balance out their improved sensitivity when only few components and limited resources are available. An intensity modulated vortex shedding meter using fiber microbends was also demonstrated [7]. The mechanical arrangement and need for fine predeformation for sensor operation are however basic limitations of the flowmeter.

A completely different sensor is proposed and investigated in this thesis, where a fiber taper is used to detect the shedding frequency using a simple mechanical arrangement and intensity detection scheme.

Being the first work on optical fiber sensors at the University of Calgary, the following chapter of this Thesis contains a basic review of optical fiber sensors and sensing techniques. A brief review on fluid flow rate measurement techniques

then follows in chapter 3 and in chapter 4 a discussion of how optical fiber sensing techniques were applied by other researchers to fluid flow rate measurement.

A theoretical and experimental investigation of the effect of hydrostatic pressure on optical fibers follows, in chapter 5. It is concluded that for intensity modulated direct sensing of the flow effects, a part of the fiber needs to be modified in order to act as a transducer imposing variations onto the light trapped in the fiber. A flowmeter using fiber tapers as transducers to sense vortex shedding of the flow past an obstructing strut is proposed and investigated in detail, in the following chapters. The process of vortex shedding past a strut is described and the related literature reviewed in chapter 6, within the limits of space available for the topic in an M. Sc. Thesis in Electrical Engineering.

Chapter 7 then addresses the proposed flowmeter, in three sections. In the first section, experimental work with fiber tapers is reported and their transmission characteristics at two different wavelengths explained qualitatively. Tapers with waist diameters having a normalized frequency less than unity are found to be more sensitive to bending, with wider ranges of monotonic decrease in transmission. These tapers are studied theoretically and modeled for their transmission versus bending characteristics, using local normal modes and modal coupling techniques. Simulation results using this model are compared to experimentally obtained characteristics resulting in very good agreement. The model and comparison of simulation results to experiment are reported in the second section of the chapter. The third section reports on the realization of a prototype flowmeter and conduction of proof-of-concept experiments.

Two configurations of the flowmeter were investigated; one using the fiber taper as a shedding strut as well as a bending vibration detector. This arrangement has the disadvantage of having the taper interacting with the fluid wake resulting in shifting of the shedding frequencies from those predicted by the well-established rigid strut vortex shedding theory. This interaction gives rise to shedding frequencies dependent on the dimensions of taper and its mounting tension. The situation is even more complicated with the highly non-linear taper transmission characteristics at the shorter wavelength. The second arrangement uses a rigid shedding strut with the fiber taper being a secondary strut mounted to sense vibrations of the fluid wake past the first strut. This arrangement enables a detection of the shedding frequencies throughout the investigated flow range. The shedding frequencies detected follow very closely those predicted theoretically with minimal taper-to-taper variations.

The investigated vortex shedding flowmeter has the advantages of simplicity of fabrication and detection scheme as compared to other flowmeters reported previously in the literature. In addition, it has the features of very low flow blockage and low cost of other vortex shedding meters. It may also be a strong candidate for the networking of such devices.

Chapter 2

OPTICAL FIBER INTENSITY AND PHASE SENSORS

Both the intensity and phase of the signal travelling in an optical fiber can be used to sense the fiber environmental conditions. Changes in these conditions can bring about modulation of the optical signal amplitude or phase, that can be detected and demodulated remotely so as to enable measurement of an environmental parameter which is called the measurand.

Being sensitive to changes in the propagation conditions inside the fiber, the phase of an optical signal is affected by changes in the fiber temperature and pressure. With the aid of a suitable optical phase detection system, these changes can be detected, enabling phase modulation sensing. Transducing mechanisms that convert changes in the measurand to changes in optical signal intensity are used to enable intensity modulation sensing

2.1. Classification of sensing schemes

Many sensing schemes of both kinds have been investigated and reported in the literature. These can be classified into two categories, extrinsic and intrinsic sensing schemes. This depends on the way of transduction of measurand changes onto changes of the optical signal. In extrinsic sensing schemes, a transducer external to the fiber is used to modulate the optical signal. The function of the fiber

then is to carry the light in and out of this transducer. Examples of extrinsic intensity and phase sensors are movable reflective diaphragm pressure sensors [8], illustrated in Fig.2.1. Intrinsic sensing schemes, on the other hand, utilize a part of the fiber to modulate the optical signal with changes of the measurand. In indirect sensing schemes, a transducer that converts these changes to changes in the fiber parameters is used. In direct sensing schemes, this transducer is not needed and the fiber parameters are affected directly by the surrounding conditions. Examples are microbending, and fiber coil microphones. These are shown in Fig.2.2. Due to their improved sensitivity and practicality, intrinsic fiber sensors have been receiving greater research efforts, while many extrinsic sensing schemes are still developed, and applied to existing optical fiber sensor systems.

2.2. Intrinsic intensity- and phase-modulated sensors

A block diagram of an intrinsic intensity modulated sensor is shown in Fig.2.3, and that of a phase modulated sensor in Fig.2.4. Two important issues in comparing these schemes to one another are system complexity, and sensitivity. Intensity modulated schemes depend on the direct detection of variations in light intensity. In some systems, a wavelength selective filter may be needed but neither polarization, nor coherence control is required. Intensity modulated schemes are not subject to polarization and phase fading as will be discussed shortly. They are generally operated by light emitting diodes (LEDs), or laser diodes (LDs) when single mode fibers have to be used.

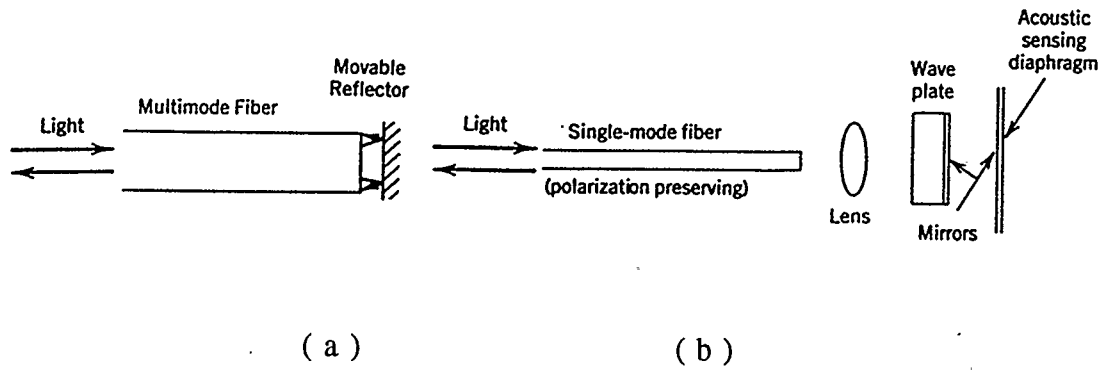


Fig. 2.1. Extrinsic intensity (a), and phase (b) pressure sensors using movable reflective diaphragms

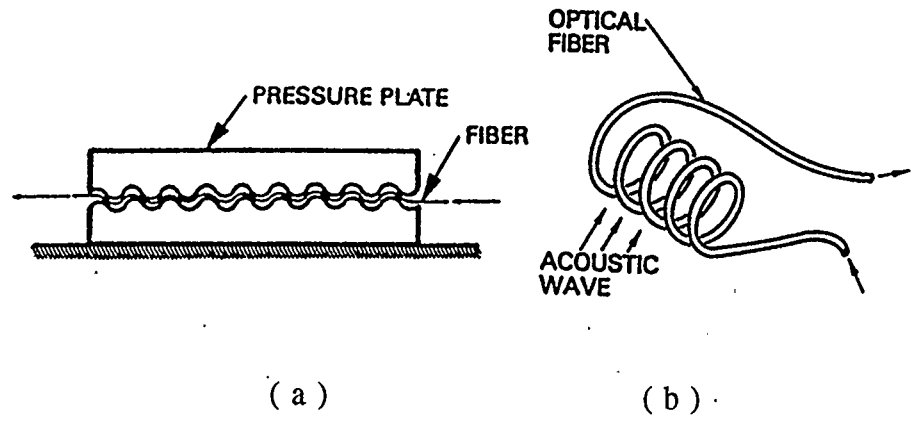


Fig. 2.2. Intrinsic intensity (a), and phase (b) acoustic sensors

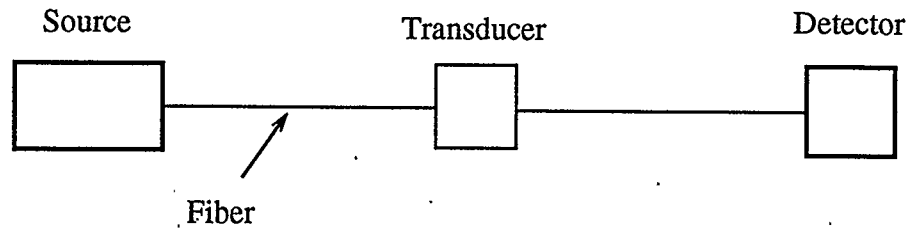


Fig. 2.3. A block diagram of a fiber optic intensity - modulated sensor

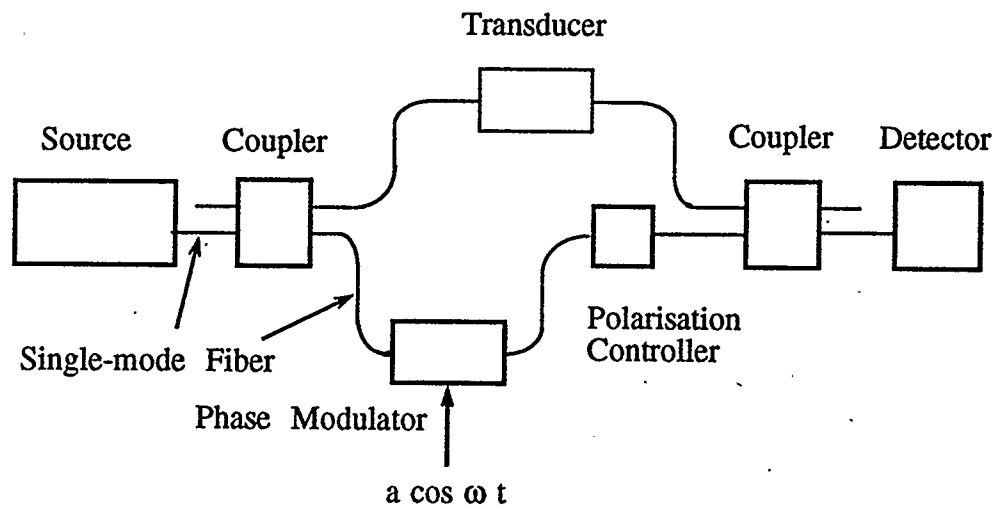


Fig. 2.4. A block diagram of a fiber optic phase - modulated sensor

Phase modulated sensors are, in principle, interferometers in which the detection of phase variations is carried out by adding up, or mixing, two optical signals shifted in phase with respect to one another by the phase angle to be detected [9]. Two such coherent optical signal , with the same polarization are added up as :

$$\begin{aligned}
 S_t &= A \cos(\omega t) + B \sin(\omega t + \phi) \\
 &= A \cos(\omega t) + B[\cos(\omega t) \cos(\phi) - \sin(\omega t) \sin(\phi)] \\
 &= [A + B \cos(\phi)] \cos(\omega t) - B \sin(\phi) \sin(\omega t) \\
 &= \sqrt{A^2 + B^2 + 2 A B \cos(\phi)} \cos(\omega t + \psi) \quad (2.1)
 \end{aligned}$$

where

$$\psi = -\tan^{-1} \frac{B \sin(\phi)}{A + B \cos(\phi)} \quad (2.2)$$

The resulting intensity is given by :

$$\begin{aligned}
 I_t = \langle S_t^2 \rangle &= \frac{A^2 + B^2}{2} + A B \cos(\phi) \\
 &= a + b \cos(\phi) \quad (2.3)
 \end{aligned}$$

where A, B, a, and b are constants.

In order to be able to detect the phase difference as given above, the two optical signals must add coherently i.e. they must have nearly the same phase except for the phase caused by the sensed quantity. This requires the difference in path length between them to be smaller than the source coherence length. In addition to containing information about the parameter being measured, the phase difference between the two interfering optical signals practically contains an arbitrary low frequency phase contribution, principally due to the differing environments of the two sensor arms. Since the output intensity I_t is a sinusoidal function of the phase difference, signal fading at the output occurs. In order to have an output intensity that is independent of such a phase contribution, optical phase modulation is used. A phase modulator can be used to apply phase modulation to one of the two interfering signals. Alternatively, with significant path difference between the two interfering signals, frequency modulation of the laser source can be used. In either case, only the phase difference due to sensing controls the resulting interferometric output, provided that the modulation frequency is much higher than the phase drifting frequency, and well above the frequency band of the sensed variations [10] hence the resulting frequency component in the detector output can be filtered out.

Another method to overcome phase fading is to employ feedback compensation for the measurement of the sensed phase. In this method, a phase modulator which is a part of a feedback loop is used to null out the phase difference between the two sensor arms. The signal input to the phase modulator, which indicates the phase being nulled, is filtered and monitored as the sensor output [9].

It is also implied above that both interfering signals have the same state of polarization. Since even a single mode (SM) optical fiber can support two orthogonal optical field polarizations, the two optical fields coming out from the interferometer arms need not have the same polarization. Furthermore, the state of polarization at the output of each arm changes with different environmental effects along this arm. In particular, the state of polarization of a guided field in a SM optical fiber is sensitive to mechanical effects, e.g. bending, as well as electric and magnetic fields. Also most kinds of phase modulators induce polarization modulation [11]. Polarization state changes cause signal fading. If the two interfering signals are orthogonal to each other, no interference signal will result at all.

To overcome this difficulty, polarization maintaining fibers (e.g. elliptical core) should be used throughout. However, polarization maintaining optical fibers and components technology is still relatively immature, and other methods must be used. Methods proposed for polarization state control for heterodyne optical fiber communication systems can be used for output polarization control of the interferometer arms [12].

Single mode fibers are needed for phase modulated sensors unless interference between different modes in a multimode fiber is employed. Except for in gyroscopes, where the two interfering signals are counter propagating waves in the same fiber and the difference in path is very small [13], laser sources are required for operation of a phase modulated sensor. Multimode lasers suffer from mode partition noise which falls exponentially with sidemode suppression ratio [14]. Mode partition effectively decreases the source coherence length.

The optical output power of the laser source must be high enough to allow for sufficient fiber attenuation, and hence greater sensitivity of the FO sensor, without going beyond the receiver thermal and shot noise limit. Typical single longitudinal mode SC lasers have output powers of the order of 1 mW , and a coherence length of several meters.

Thus, a phase modulated sensing scheme is far more complicated than an intensity modulated one.

As for the sensitivity phase modulated sensors are generally more sensitive than intensity modulated sensors this being due primarily to the sensitivity of optical signal phase to minute changes in fiber parameters. Two performance parameters of an interferometric scheme are : Fringe visibility, and minimum detectable phase. Fringe visibility depends on the state of polarization and degree of coherence of the two interfering optical signals, while minimum detectable phase depends on optical power level, fringe visibility, and total noise level of the system.

Transduction of changes in the measurand to changes in the signal phase is characterized by a sensitivity coefficient which is measured in radians per meter (of fiber length) per unit of the measurand. The minimum detectable phase thus translates into a minimum detectable or resolvable change in the measurand.

Performance of an intensity detection scheme is expressed in terms of unity SNR power level, which is equivalent to a minimum detectable optical power. The

transduction is characterized by a sensitivity factor measured in optical power per unit of the measurand. These give the minimum detectable change in the measurand.

Phase modulated acoustic sensors of minimum detectable pressure of 20 to 40 dB relative to 1 μPa have been reported [9, 15]. This means that an acoustic wave with pressure variations of 20 to 40 dB more than that of a wave of 1 μPa root mean square pressure variations would be detected. A -10 dB figure is theoretically expected based on a minimum detectable phase of 10^{-7} radians [9]. Microbending acoustic sensors having 70 dB relative to 1 μPa minimum detectable pressure were reported [16], while 25 dB relative to 1 μPa is theoretically expected.

Phase modulated sensors are more sensitive to surplus lead environmental fluctuations, while these fluctuations can have only minor effects on the performance of intensity modulated sensors [17].

While phase modulated sensors are very promising, they are relatively complicated, and yet far from being practical for most industrial applications. On the other hand, intensity modulated sensors still need more research and development efforts and are expected to provide practical sensor systems for many industrial applications. These sensors can be implemented and investigated using a minimum number of components, in relatively simple system configurations. These facts were the main factors directing the research reported in this thesis.

Chapter 3

FLUID FLOW RATE MEASUREMENT TECHNIQUES

Flow rate measurement is one of the most important industrial applications since a knowledge of fluid flow rate in pipes is necessary for both monitoring and process control.

There are many well established techniques to measure fluid flow rate in closed pipes and these can be grouped in four major groups : Direct flow rate measurement, Differential pressure, Point velocity measurement, and Average velocity measurement techniques [18].

3.1. Direct and differential pressure flow rate measurement

Direct flow rate measurement techniques depend on measuring the volume of the fluid flowing in unit time directly, by forcing the flow into chambers of known volume. These techniques are practical only for a very limited range of flow rates, and can not be used in most industrial applications. Direct meters include turbine and vanemeters. Differential pressure techniques are the most popular. A contraction of the flow cross section is used to produce a difference in pressure between two sections of the pipe and this difference in pressure can be measured and used to extract the flow rate. Many designs have been studied thoroughly, of which the Venturimeter is the most advantageous, yet most expensive. This is shown in Fig. 3.1.

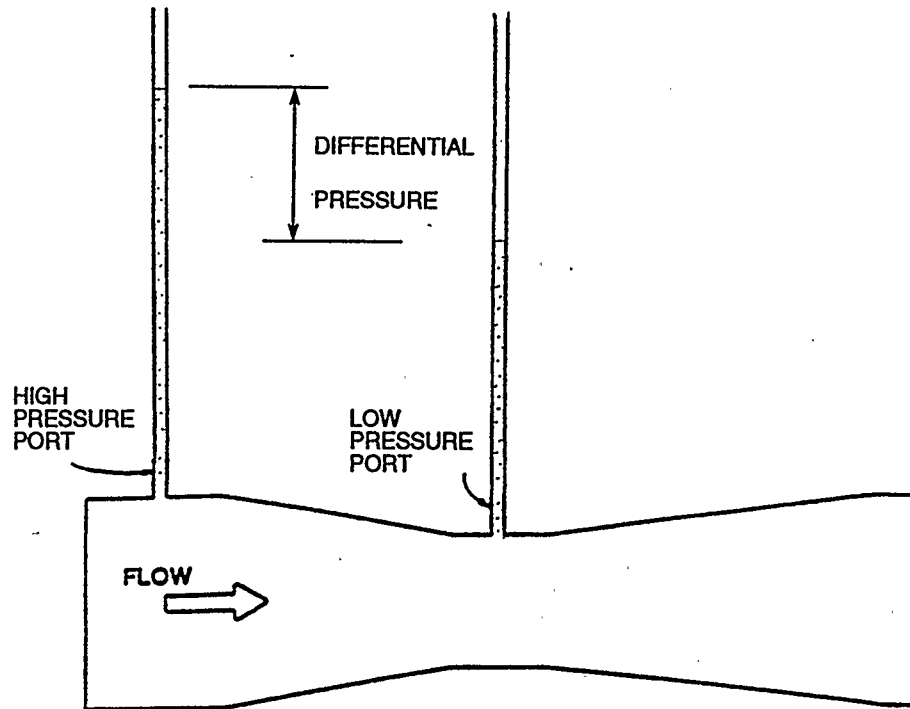


Fig. 3.1. Differential pressure measurement using a Venturimeter

3.2. Point velocity measurement techniques

Point velocity measurement techniques use measurement of the flow velocity at a specific point of the pipe cross-section to deduce the flow rate. This is carried out using a laser beam, a short heating wire, or Pitot tubes. In Laser Doppler Anemometry light scattered by particles in the fluid is detected and its Doppler Shift in wavelength is measured. This shift is proportional to the particle velocity hence to the flow velocity. In Hot Wire Anemometry a heating wire is inserted into the flow and the amount of electrical power required to keep the wire in equilibrium is measured. This amount is equal to the rate with which heat is lost by convection, and is calibrated to give the velocity of flow at the measurement point.. In Dynamic Pressure Measurement tiny tubes named Pitot tubes are installed in the pipe. One tube measures the stagnation pressure, that is the pressure at a point in the fluid inside the flow forced to have zero velocity in front of the tube. Another tube, or more than one other tube, is used to measure the static pressure at the same location. The difference between these two values of pressure gives the dynamic pressure head which is directly related to the flow velocity at the measurement point [19].

One of the main disadvantages of a Laser Doppler Anemometer is its need of a narrow linewidth laser for the detection of low velocities. With a linewidth of 5 MHz, which is typical of semiconductor index guiding lasers, the minimum detectable velocity is 1.1 m/s (at 870 nm). Another disadvantage is the need for optical spectral analysis, or interferometric detection both of which are sophisticated techniques. Laser Doppler Anemometers (LDAs) have received much development and are used for fluid flow rate measurement in blood vessels [20,21].

3.3. Average velocity measurement techniques

These techniques are very diverse since they include : Ultrasonic flow meters, Magneto-inductive meters, Vortex Shedding, and Mass flow meters. In each of these devices an effect of the flow is measured from which knowledge of the average flow velocity, and hence flow rate, is possible. Ultrasonic meters utilize high frequency pressure waves to detect flow, either by transit time, or Doppler effects. Transit time flow meters transmit and receive pressure waves diagonally across the flow where the flight time of these waves across the pipe depends on the flow velocity. The difference in flight time between two oppositely transmitted wave packets is directly proportional to the average flow velocity. Doppler ultrasonic meters measure the Doppler shift in frequency of pressure waves scattered back by particles flowing in the fluid, which gives an average flow velocity. Both flow meters are illustrated in Fig. 3.2. The operation of ultrasonic flow meters is sensitive to solid or bubble content of the fluid.

Magneto-inductive flow meters measure the voltage induced due to the passage of an ionic fluid in a magnetic field perpendicular to the direction of flow. They are restricted in operation to ionic fluids and require a high power voltage supply for the operation of the magnets.

Vortex Shedding meters measure the frequency at which vortices are shed i.e. separated past an obstacle inserted into the flow. The presence of this obstacle, called a strut, generates vortices in the flow which are shed at a constant rate, depending only on the flow velocity, and the corresponding Reynolds number. The

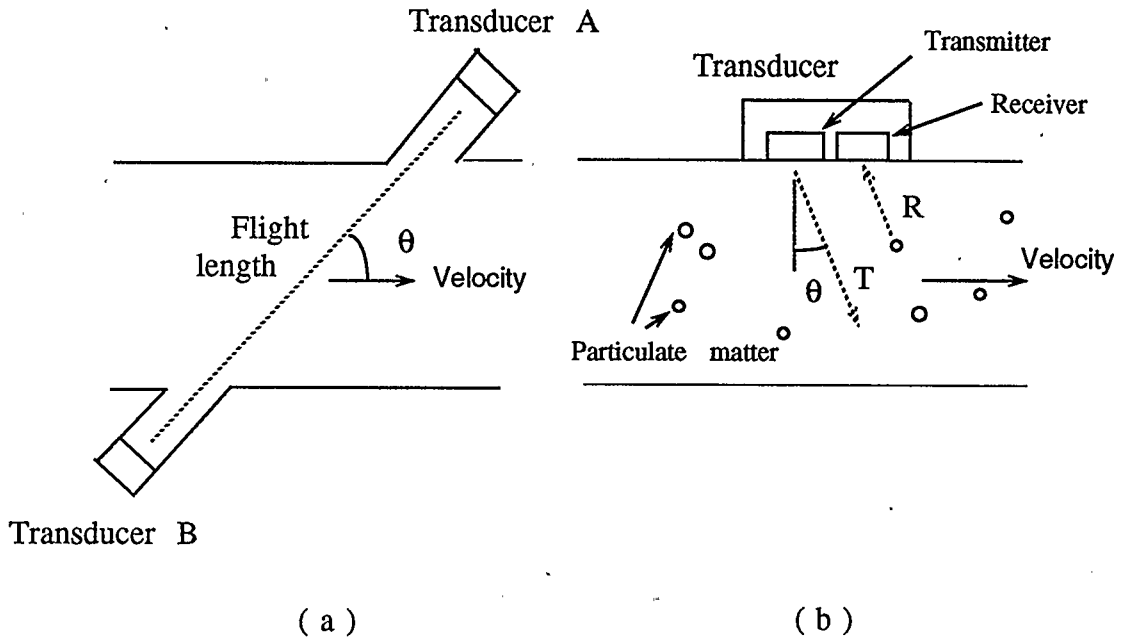


Fig. 3.2. Ultrasonic transit time (a), and Doppler (b) flowmeters

detection of the vortex shedding frequency can be carried out by piezoelectric, mechanical, or optical vibration detection techniques, and by band-pass filtering the vortex shedding frequency can be extracted and the flow rate deduced. Vortex shedding flow meters can be used with liquids, gases, mixed flows, and dirty liquids and they have gained larger popularity in recent years. Detailed discussion of these flow meters will be given later in this thesis.

Mass flow meters depend on measuring the momentum of the flowing fluid thus giving the mass flow rate in the pipe. This can be done by forcing the fluid to rotate along the rim of a floating mass in a diverging tube, by forcing the flow into a turbine using a constant speed motor, or by measuring the reaction force due to local rotation or vibration in a direction normal to the flow. These reaction forces are called Coriolis forces. Coriolis mass flow meters measure such forces by measuring the induced vibrations of a flow pipe driven by a constant excitation, normal to the flow direction, from which the mass flow rate can be deduced. Coriolis flow meters that use optical fibers in detecting vibrations have been reported in the literature. The systems used are rather complicated [2].

Despite this wide variation in flow rate measurement techniques and devices, there is still a need for measuring devices suited for particular applications such as sewage water and mixed flow. Moreover, the detection techniques used with various devices can be developed towards more simple and efficient techniques, which in general include optical sensing and detection techniques [22, 23].

Chapter 4

OPTICAL FIBER FLOWMETERS

With the increasing application of optical fibers in sensing, remote process monitoring, and control, many optical fiber flowmeter configurations have been proposed and investigated. Many of these, however, are extrinsic sensing schemes that utilize the fiber only for conducting light in and out of a light operated transducer.

4.1. Application of fibers to fluid flow meters

Fibers have been used to read out turbine meters, by chopping the light in a fiber gap at a rate proportional to the impeller speed. This can be done by using the impeller blades to chop the light, or a diaphragm switch driven by a magnetic coded disc coupled to the impeller shaft. Both reflective, and transmissive modes of speed detection have been used [1].

Laser Doppler Anemometers that make use of fibers to conduct laser light to the measurement point have been reported and used in medical and industrial applications [24 - 26]. Heterodyne detection using bulk optics, and Integrated Optics modules, together with polarization maintaining fibers was applied to these velocimeters. Balanced mixing was used to enhance the sensitivity of detection to near the shot noise limit [27, 28].

The use of a controlled balance arm in the heterodyne interferometer has enabled a selection of the measurement point, so that velocity profiling is possible [29], and this overcomes the presence of a stagnation region close to the fiber tip in a flow measurement. Sophisticated photon correlation techniques have been used to characterize particle size and flow velocity [30, 31].

Intrinsic phase modulated sensing of pressure differentials has recently been applied to dynamic pressure measurements [3]. A double Mach-Zehnder interferometer composed of two different reference fiber coils and two sensing coils similar to the reference ones, was used to produce two linearly independent phase shifts induced by differentials in pressure and temperature thus enabling a determination of the pressure differential. With fiber coils of a length of 5 meters a minimum detectable dynamic differential pressure of 1000 Pa was achieved. The system can, in principle, be applied in a static differential pressure measurement as well. It, however, needs cyclic drift correction and is limited by high temperature and vibration sensitivity of the phase detection scheme.

Extrinsic phase modulation sensing was used to detect the amplitude of vibration in a coriolis mass flow meter [2] where optical fibers were used to remotely excite the mechanical vibration driver, and to detect the phase modulation in an interferometric arrangement. Frequency demodulation, and phase comparing electronics were used to give a voltage signal proportional to the flow rate.

4.2. Vortex shedding flowmeters

Vortex shedding meters utilizing optical fibers have also been reported [1, 4, 5]. Flexible diaphragms mounted on the shedding strut were used to drive a rod interrupting the transmission of light in a fiber gap with fibers being inside the strut. Alternatively, a reflective diaphragm pressure sensor was used to detect pressure variations brought about by the vortex shedding.

An intensity - modulated vortex shedding flowmeter was realized using fiber microbends to detect the vibration of a secondary bar past the strut [7]. This sensor design is illustrated in Fig. 4.1. The mounting of the microbends sensor inside the meter provides for a certain amount of fiber predeformation and is a very important and difficult part of the meter realization.

Phase sensing techniques have been used to detect the vortex shedding frequency either by sensing the vibration of a secondary sensing bar mounted past the shedding strut, or by direct sensing of the vibration of the fiber used as the shedding strut.

Using a Fabry-Perot interferometer composed of a single mode fiber and a matching confocal mirror mounted on the sensing head of a vortex shedding flowmeter the shedding frequency was detected. Another arrangement overriding the need for fine mechanical adjustment uses part of the fiber as the Fabry-Perot interferometer. The two reflecting facets in this arrangement are the fiber end, and a semicleaved facet made at the other end of the fiber part on joining it to the rest of the fiber. The

fiber Fabry-Perot was mounted on the meter body, stretched between a fixture to the body and a vibrating stem, driven by the sensing head. These two configurations are illustrated in Fig. 4.2. The resulting frequency measurements compare very well to the measurements with a piezoelectric transducer detector and a signal component of 15 to 25 dBV greater than the noise background was obtained. Both systems, however, used complicated phase detection arrangements involving frequency modulation of the laser source.

Another implementation was to use the fiber itself as the shedding strut by stretching the fiber, under tension, across the flow. A single mode fiber comprising a fiber Fabry-Perot was used [5]. The length of this interferometer was modified by the response of the part installed across the flow to the vortex shedding forces. A long coherence-length gas laser was used to operate the fiber Fabry-Perot interferometer. The intensity of the shedding frequency signal was 20 dB greater than background noise level. This system is illustrated in Fig. 4.3.

Multimode fibers were used in a transmissive arrangement [6] and phase changes due to forces on the fiber, induced by vortex shedding, were detected by observing changes in the speckle pattern at the fiber output end. Such a detection scheme is known as the fiberdyne technique [32] and is relatively complicated, having multiple fading and distortion problems. Nevertheless, the shedding frequency was detectable over a range limited by the flow rig and a hiatus existed at a flow velocity around 1 m/s, within which no distinct frequency peaks were observed. This hiatus can also be seen in the results of the single mode fiber Fabry-Perot arrangement and it was also observed in the experimental investigations conducted in

our work, with a fiber taper as the strut, and at higher flow velocities. This confirms the suggestion that it is due to an antiresonance effect of the compound wake-fiber mechanical system, that results in very small vibration amplitude of the fiber at these velocities.

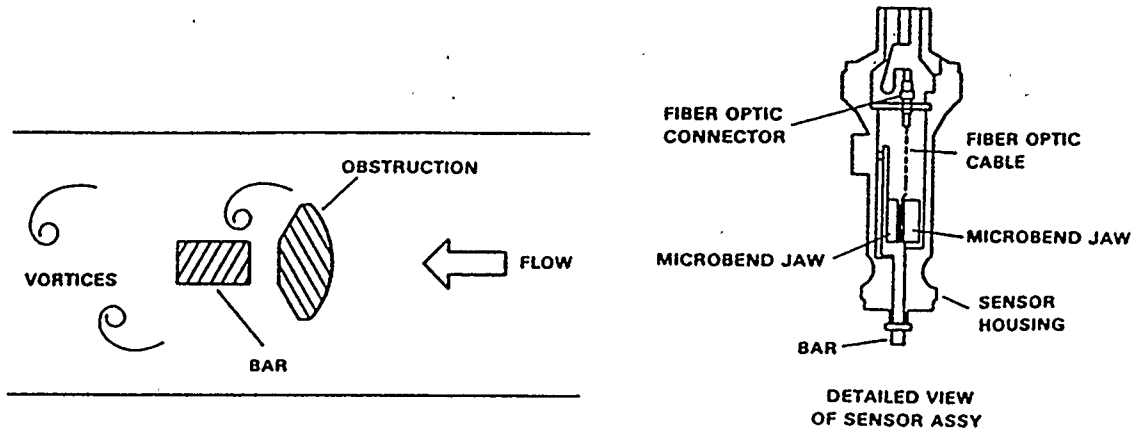


Fig. 4.1. A vortex shedding flowmeter using fiber microbends

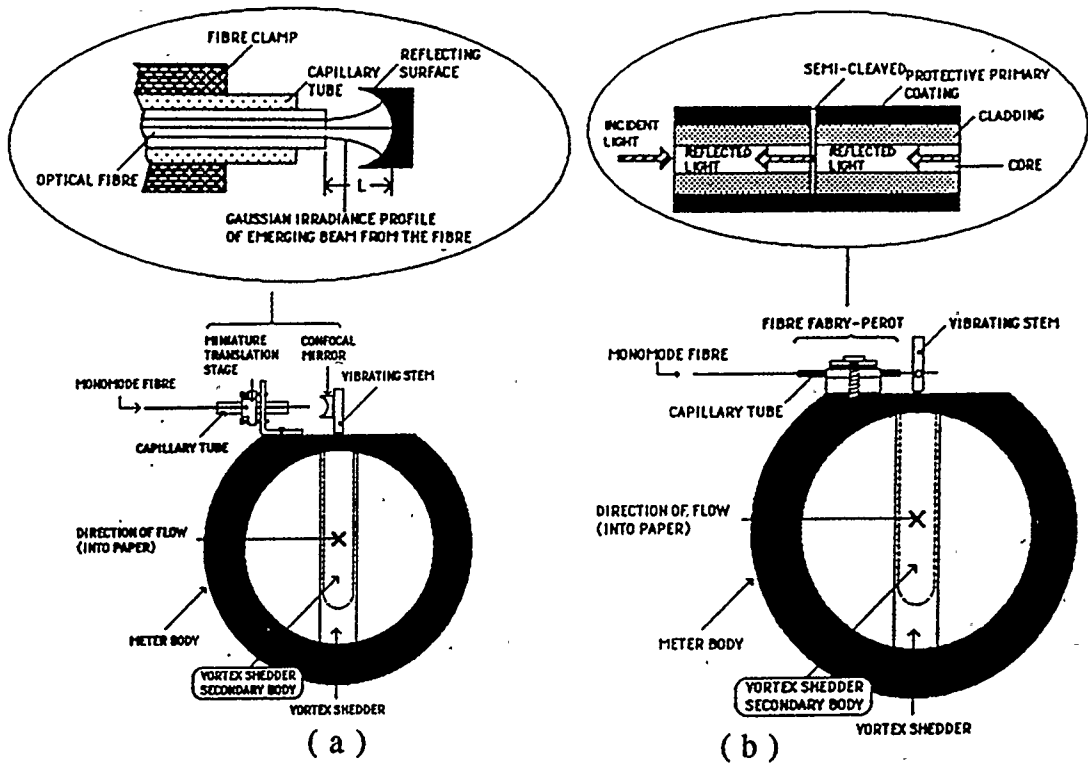


Fig. 4.2. Vortex shedding flowmeters using external optical resonators :

using confocal mirrors (a), and a fiber Fabry-Perot (b)

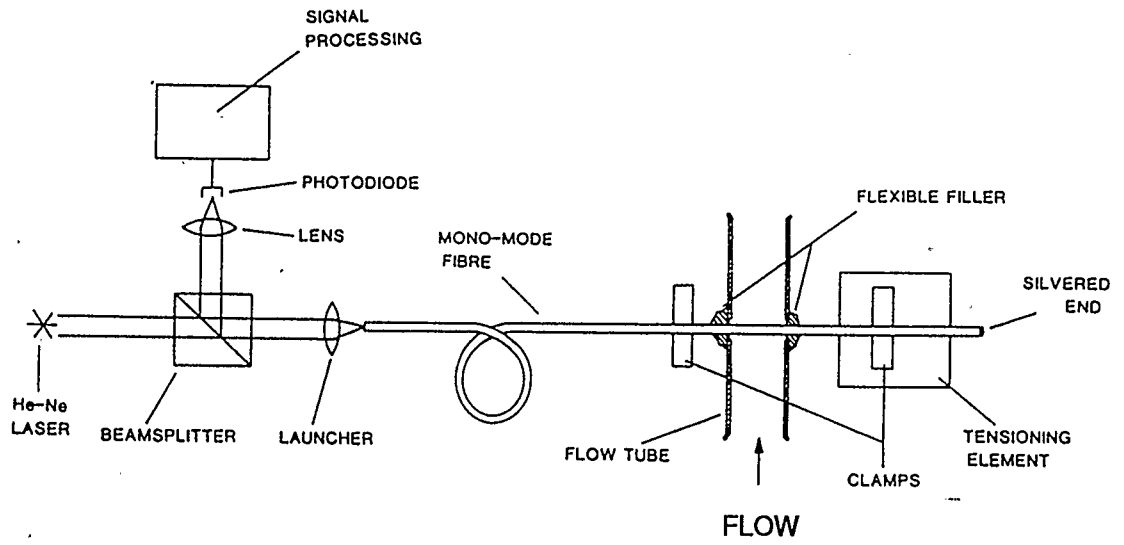


Fig. 4.3. Intrinsic phase - modulated vortex shedding flowmeter using a single - mode fiber as the shedding strut

Chapter 5

INVESTIGATION OF DIRECT INTENSITY - MODULATED EFFECTS OF PRESSURE ON OPTICAL FIBERS

In searching for an effective fiber-optic intensity sensing technique for the measurement of flow rate, the effect of pressure on optical fibers was investigated. Detection of pressure differences would enable a measurement of flowrate with a static differential pressure arrangement, for example a venturimeter with the fiber used to sense pressures at the venturi sections. A dynamic differential pressure arrangement similar to that reported for phase modulation sensing [3] could also be used. While the effect of fiber pressure on the phase of an optical signal travelling in a single mode fiber has been well covered in the literature [33 - 37], intensity modulation effects have not been so well addressed. In this chapter, these effects are investigated.

Pressure stresses induce strains in the fiber which are accompanied by a change in the refractive index of the fiber material through the photoelastic effect. The resulting phase shift has contributions from the axial strain (axial elongation) and the change in modal effective refractive index. The change in refractive index of the fiber core and contraction of the fiber diameter contribute to the latter effect.

In intensity-sensing rather than phase sensing of pressure variations, it is the change of effective refractive index that accounts for expected reflection or radiation of

light at the junction between two fiber parts exposed to different pressures. While the sensitivity of a phase sensor can be increased by increasing the length of the sensing fiber coil, the sensitivity of an intensity-modulated sensor depends only on the effect of pressure differences at the input and output sections of the sensing coil. A pressure of at most 1 atmosphere (100,000 Pa) should be sensed effectively in order that the sensor is useful for differential pressure flowrate measurements in general water flow applications.

5.1. Theoretical Estimation of the Change in Effective Refractive Index

It is intended here to isolate the terms contributing to the change in effective refractive index for the modal wave in a fiber, from calculations of phase changes appearing in the literature [33 - 37], and give an idea about its magnitude.

We have for the optical phase, ϕ :

$$\phi = k_0 n_{\text{eff}} L \quad (5.1)$$

where

$$k_0 = \text{wavenumber in free space} = 2\pi / \lambda_0$$

$$n_{\text{eff}} = \text{effective refractive index for the propagating mode}$$

$$L = \text{path length}$$

Differentials are accordingly related by :

$$\Delta \phi = k_0 n_{\text{eff}} \Delta L + k_0 L \Delta n_{\text{eff}} \quad (5.2)$$

The first term on the right hand side is the contribution of axial fiber elongation to the phase shift and the second term is contributed by the change in effective index.

The effective refractive index for the mode depends on the refractive indices and the diameters of the fiber core and cladding. A first approximation would ignore the effect of changes in refractive index and diameter of the cladding and consider only those of the core [33]. The effect of cladding and coatings on the fiber will be addressed later. Thus, we can write :

$$\Delta n_{\text{eff}} = \frac{dn_{\text{eff}}}{dn} \Delta n + \frac{dn_{\text{eff}}}{dD} \Delta D \quad (5.3)$$

where n and D are the fiber core refractive index and diameter, respectively. The change in refractive index is related to strains in the fiber by the strain-optic tensor. For a fiber under isotropic pressure there are no shear strains and the strain in any direction inside the fiber is given by :

$$\epsilon = - \frac{P}{E} (1 - 2\mu) \quad (5.4)$$

where

P = pressure

E = Young's modulus, the proportionality constant between axial stress and axial elastic strain

μ = Poisson's ratio, the ratio of radial contraction to axial elongation.

Considering the fiber to be optically homogeneous and isotropic [34], the change in refractive index seen by a wave travelling in the fiber is calculated from :

$$\Delta\left(\frac{1}{n^2}\right) = -\frac{P}{E}(1-2\mu)(p_{11}+2p_{12}) \quad (5.5)$$

where p_{11} , and p_{12} are elements of the strain-optic tensor. Thus :

$$\Delta n = -\frac{n^3}{2}\frac{P}{E}(1-2\mu)(p_{11}+2p_{12}) \quad (5.6)$$

The change in fiber diameter is :

$$\Delta D = \epsilon D = -\frac{P}{E}(1-2\mu)D \quad (5.7)$$

thus $\frac{dn_{\text{eff}}}{dD}$ can be calculated as follows :

$$\frac{dn_{\text{eff}}}{dD} = \frac{dn_{\text{eff}}}{db}\frac{db}{dV}\frac{dV}{dD} \quad (5.8)$$

where b and V are the normalized propagation constant of the modal wave, and normalized frequency of the fiber, respectively. We have [38] :

$$\frac{dV}{dD} = \frac{V}{D} \quad (5.9.a)$$

and

$$\frac{dn_{\text{eff}}}{db} = \frac{2V^2}{k_0^2 D^2 n_{\text{eff}}} \quad (5.9.b)$$

$\frac{db}{dV}$ is the slope of the b - V curve at the point describing waveguiding

conditions. Substituting equations (5.6-9) into (5.3) gives :

$$\Delta n_{\text{eff}} = \left\{ \frac{d n_{\text{eff}}}{d n} \frac{n^3}{2} (p_{11} + 2 p_{12}) - \frac{2 V^3}{k_0^2 D^2 n_{\text{eff}}} \frac{d b}{d V} \right\} (1 - 2 \mu) \quad (5.10)$$

Two cases can now be considered :

For single mode fibers with $n_{\text{eff}} \approx n$, $V \approx 2.4$, $\frac{d b}{d V} \approx 0.5$, and if $n = 1.458$, $E = 7 \times 10^{10}$ N/m², $\mu = 0.16$, $p_{11} = 0.126$, $p_{12} = 0.27$, are typical values for fused silica fibers [35,39], then we get :

$$\frac{\Delta n_{\text{eff}}}{P} = 10^{-11} - 2.325 \times 10^{-12} \left(\frac{\lambda_0}{D} \right)^2 \text{ Pa}^{-1} \quad (5.11)$$

where all quantities are in SI units.

The first term is contributed by the photoelastic effect, whereas the second, which is much smaller, by the change in core diameter.

For a fiber of 5 μm core diameter at a wavelength of 0.633 μm , which is the optimum case to maximize the RHS of equation (5.11), we get :

$$\frac{\Delta n_{\text{eff}}}{P} = 9.6937 \times 10^{-12} \text{ Pa}^{-1} \quad (5.12)$$

The other case is that of multimode fibers; for which $V \frac{db}{dV}$ is very small, and only the first term of equation (5.10) would contribute to the change in effective index. With $\frac{dn_{\text{eff}}}{dn} \approx 1$, $n = 1.46$, and taking an extreme case of parameters [33] :

$E = 5 \times 10^{10} \text{ N/m}^2$, $\mu = 0.17$, and $p_{11} = p_{12} = 0.3$, we get :

$$\frac{\Delta n_{\text{eff}}}{P} = 1.85 \times 10^{-11} \text{ Pa}^{-1} \quad (5.13)$$

which in this case represents an average amount over the propagated modes in the fiber.

The above values are really very small if changes of one atmospheric pressure are to be detected. For $\Delta n_{\text{eff}} = 10^{-5}$, which is the finest difference in index measurable by Frequency Domain Reflectometry [40] and Refractometer sensor configurations [41,42], a difference in pressure of at least 5 atmospheres is needed. It is also important to note that for fused silica fibers the rate of change in refractive index with temperature is high compared to the pressure sensitivity. At a wavelength of $0.63 \mu\text{m}$ this is

$$\frac{dn}{dT} \approx 10^{-5} / ^\circ\text{C}$$

So, variations in temperature can cause confusion in investigations of the

above reported pressure effect.

The effect of changes in the parameters of the cladding, with pressure, can be taken into account using complicated mechanical modeling of the fiber [36]. Single and multiple elastic coatings can also be used to enhance the fiber response to pressure variations. Two and three dimensional models have been studied for phase modulated sensing applications [37].

Ignoring the term due to changes in the fiber core and cladding diameters, and assuming that $n_{\text{eff}} \approx n$, a two dimensional model gives [36] :

$$\Delta n_{\text{eff}} = \frac{n^3}{2} \{ \epsilon_1 (p_{11} + p_{12}) + \epsilon_3 p_{12} \} \quad (5.14)$$

where

$$\epsilon_1 = - \frac{\mu_{\text{co}} (1 - 2 \mu_{\text{cl}})}{f E_{\text{co}} + (1-f) E_{\text{cl}}} P \quad (5.15.a)$$

and

$$\epsilon_3 = - \frac{1 - 2 \mu_{\text{cl}}}{f E_{\text{co}} + (1-f) E_{\text{cl}}} P \quad (5.15.b)$$

are the resultant radial and axial strains in the fiber core, respectively. The photoelastic constants p_{11} , and p_{12} are those of the core whilst μ_{co} and E_{co} are Poisson's ratio and Young's modulus of the core, and μ_{cl} and E_{cl} are those of the cladding. f is the ratio of core to cladding radii.

The conditions :

$$f \ll 1, \quad \text{and} \quad \frac{E_{cl}}{E_{co}} \ll 1 \quad (5.16)$$

have been assumed to hold for (5.14). This means that the cladding outer radius is much larger, and it is made of a highly compliant material as compared with the core, e.g. plastic clad glass fibers. It can be shown that these are the conditions for maximum fiber response to the pressure.

Taking $n = 1.46$, $p_{11} = 0.126$, and $p_{12} = 0.27$ gives :

$$\frac{\Delta n_{eff}}{P} = -0.6162 \epsilon_1 - 0.42 \epsilon_3 \quad (5.17)$$

For a fiber with plastic cladding having : $E_{cl} = 0.076 \times 10^{10} \text{ N/m}^2$, $\mu_{cl} = 0.458$, which are for a polyethylene cladding, and taking $f = 0$, $\mu_{co} = 0.17$, we get :

$$\epsilon_1 = -1.88 \times 10^{-11} P, \quad \epsilon_3 = -1.1 \times 10^{-10} P$$

Thus,

$$\frac{\Delta n_{eff}}{P} = 5.8 \times 10^{-11} \text{ Pa}^{-1} \quad (5.18)$$

This gives an enhancement of about 6 over the optimum case in the fiber sensitivity to pressure, yet it is much smaller than suitable for optical intensity detection. A minimum change of 1.7 atmospheres is required to give Δn_{eff} of 10^{-5} .

Fibers jacketed with Teflon are expected to give maximum response to

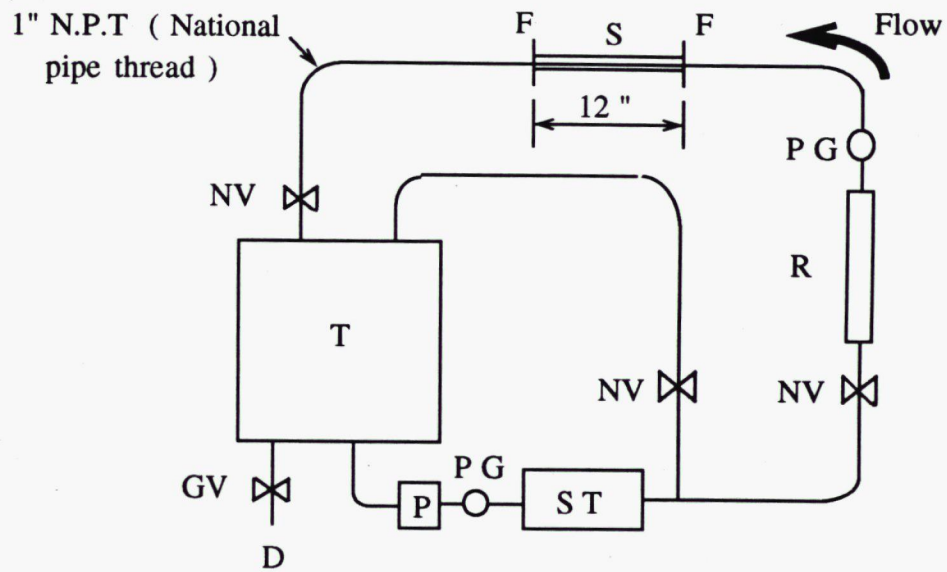
pressure [37]. The same formulae (5.12 - 5.17) can be used to estimate the response of such fibers, modeling the jacketed fiber as a two layer cylinder with the fiber core and cladding considered as an elastically homogeneous glass cylinder. Using the parameters of Teflon: $E_J = 0.306 \times 10^{10} \text{ N/m}^2$, and $\mu_J = 0.317$, gives :

$$\frac{\Delta n_{\text{eff}}}{P} = 6.27 \times 10^{-11} \text{ Pa}^{-1} \quad (5.19)$$

which is still much too small to yield practical intensity sensing of pressure variations.

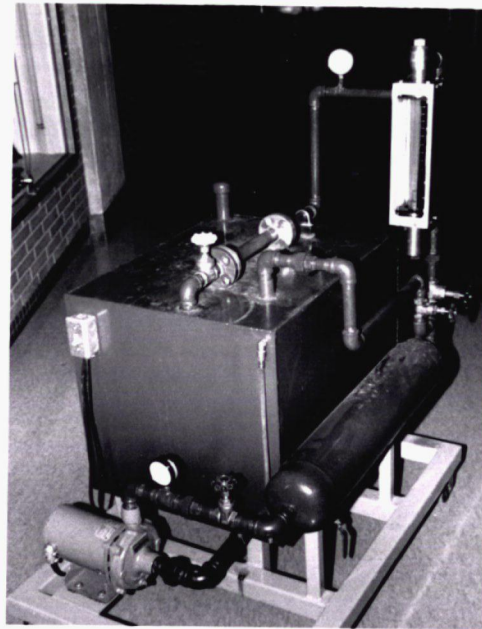
5.2. Experimental Investigation

The prediction that pressure variations will not have an effect on the intensity of light propagating in an optical fiber was confirmed experimentally using a water flow rig. The rig consisted of 1 inch pipes, with a replaceable plexiglass test section, 1 cubic meter tank, and a pump capable of delivering 30 pound per square inch of pressure. Valves for the control of flow rate, and pressure in the test section, and a rotameter for flowrate indication were installed. The same rig was used in investigating vortex shedding flowmeter configurations using different test sections. Fig. 5.1 gives a schematic and a photo of this rig. The test section used is illustrated in Fig. 5.2. The fiber used was a multimode fiber with core and cladding diameters of 50, and 125 μm respectively, and a numerical aperture of 0.19. The coating appeared to be very compliant since it obviously gave flexibility to the fiber which was otherwise very brittle. Unfortunately no information was available about its material and no other multimode fiber with similar coating was available for our use at that



D	system drain	NV	needle valve	R	rotameter	T	tank
F	flange	P	pump	S	sensor		
GV	gate valve	PG	press. gauge	ST	surge tank		

(a)



(b)

Fig. 5.1. A schematic (a), and a photo (b) of the flow rig used for experimental investigation

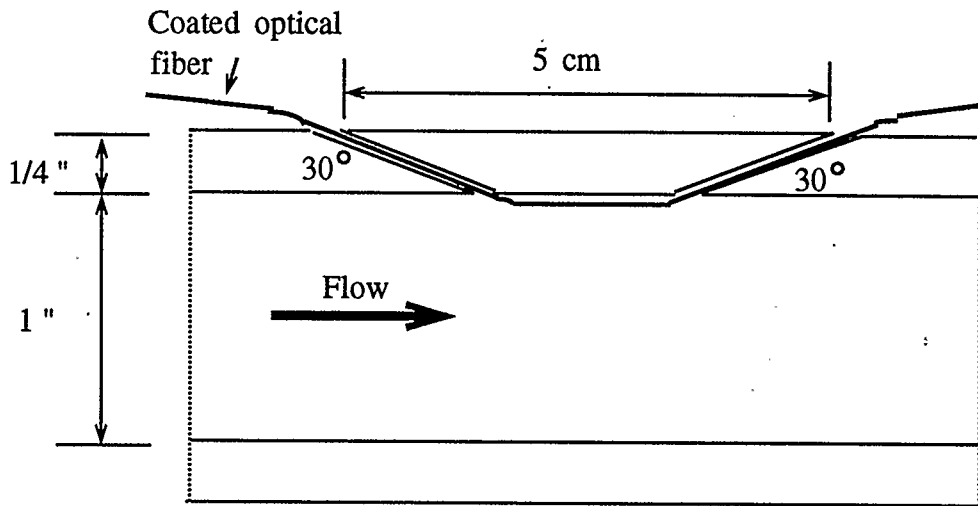


Fig. 5.2. A cross-section of the plexiglass test section with the fiber sensor

time. The fiber was brought into the test section using 30° bends, as indicated in the figure, to minimize losses due to cornering in and out of the plexiglass holes. After installing the fiber, it was epoxied to the plexiglass at the outside hole openings.

Pressures ranging from 0 to 30 Psi, i.e., 0 to 207 kPa, were applied to the test section, at zero, as well as nonzero flow rates. Intensity of the optical signal transmitted through the fiber was monitored for corresponding variations. A light emitting diode (LED) source emitting at 0.82 μm was used, and when no signal changes resulted, a He-Ne laser diode emitting at 0.633 μm was used. Coupling to the fiber was done by using SMA connectors in the first case, and bulk-optics components for the He-Ne laser. The transmitted power was 1.45 μW , for the LED, and about 0.5 mW, for the He-Ne laser. Pressure and flowrate variations had almost no effect on the average transmitted optical power. The detected signal waveform was observed on the CRO. For the LED source no specific waveform was seen except for a very low noise signal. For the He-Ne laser source, variations at low periodicity were seen. Table 5.1 summarizes the results obtained. Waveform variations, in the case of the He-Ne source, were further investigated using a Hewlett Packard signal analyser, the Structural Dynamics Analyser 5423A. An Optikon 1500XP optical waveform analyser was used for the detection and amplification of the intensity signal. A frequency component related to the flow, and its dependence on the pressure were looked for. Since bulk optics could couple mechanical vibrations into the system, another channel of the signal analyser was used to monitor mechanical vibrations on the optical bench. Bruel and Kjaer accelerometer, type 4370, and charge amplifier, type 2635, were used for mechanical

Table . 5.1. Summary of experimental results with the fiber sensor of Fig. 5.2

LED at $\lambda = 0.82 \mu\text{m}$			LD at $\lambda = 0.633 \mu\text{m}$		
* Output (μW)	Press.	** F. R.	* Output (μW)	Press.	** F. R.
1.45	0	0	508 - 555	0	0
1.45	30 psi	0	508 - 555	30 psi	0
1.45	0	20 %	511.3 - 549.7	0	20 %
1.45	28 psi	20 %	510.6 - 550.3	28 psi	20 %
1.45	0	100 %	505.3 - 544.3	0	100 %
1.45	24 psi	100 %	504.7 - 549.1	24 psi	100 %

* Transmitted optical power as detected at the output of the fiber installed in the test section. ** F. R. = Flow rate

vibration pick up and amplification. The following summarizes the results obtained. As a reference for the measurements, spectra of the mechanical and electrical channels were traced with the accelerometer disconnected from the charge amplifier and the fiber disconnected from the waveform analyser input. A black cap provided with the waveform analyser was used to block any input light. These traces are displayed in Fig. 5.3.b. Fig. 5.3.a displays the parameters of the signal analyser equipment for the whole spectral measurements. The two traces display the spectra of the received signals from the mechanical channel connected to the B&K charge amplifier (upper), and the electrical channel connected to the Optikon waveform analyser (lower), respectively. The largest peak at low frequency in Fig. 5.3.b is at 60 Hz, and is due to electrical wiring pick up of main frequency in the lab environment since batteries were used to power both the charge amplifier and optical waveform analyser. Fig. 5.3.c gives the spectra with the accelerometer mounted on the optics bench, connected to the charge amplifier, and the fiber mounted to the input of the waveform analyser. It seemed that connecting the accelerometer increased the pick up of the 60 Hz hum, as can be seen from the trace. The spectra with the laser turned on and the rig still off are given in Fig. 5.3.d. Low frequency laser noise is now added up to the electrical channel noise, while the mechanical channel noise is unaffected. Fig 5.4 displays the traces obtained with different flowrates, and pressures. With flow many low frequency peaks appear on the spectrum of the mechanical channel in addition to the large 60 Hz peak which appears not to change in magnitude. These vibration peaks are coupled into the electrical channel through the bulk optics mounted on the bench, through the fiber immersed into the flow, and maybe, through the receiver connector.

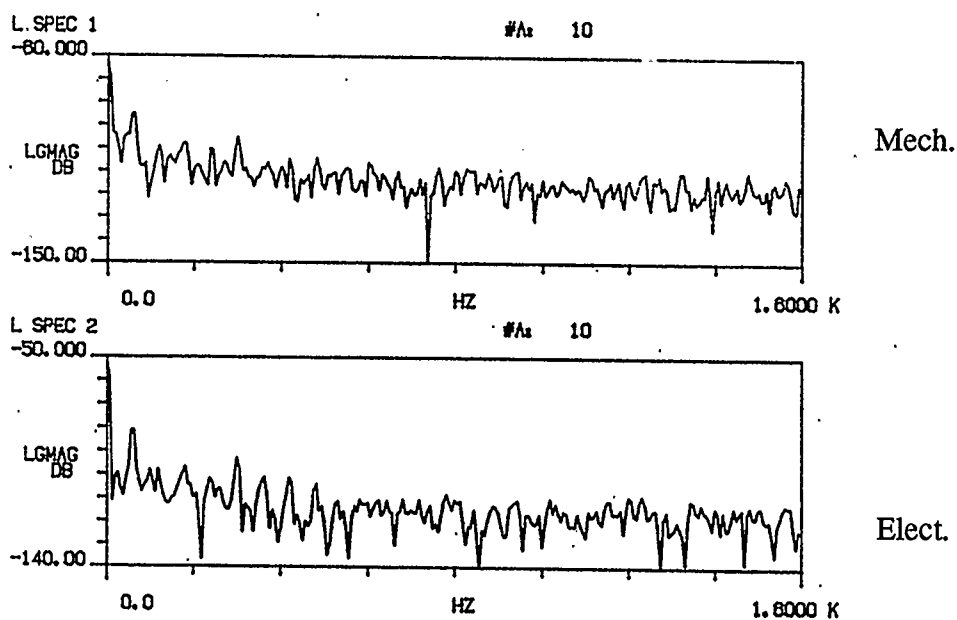
MEASUREMENT STATE

MEASUREMENT :	LINEAR SPECTRUM	
AVERAGE :	10	STABLE
SIGNAL :	RANDOM	
TRIGGER :	INTERNAL	CHNL 1

CENT FREQ :	0.0 HZ	ΔF :	8.25000 HZ
BANDWIDTH :	1.80000 KHZ		
TIME LENGTH :	180.000 mS	ΔT :	158.250 μS

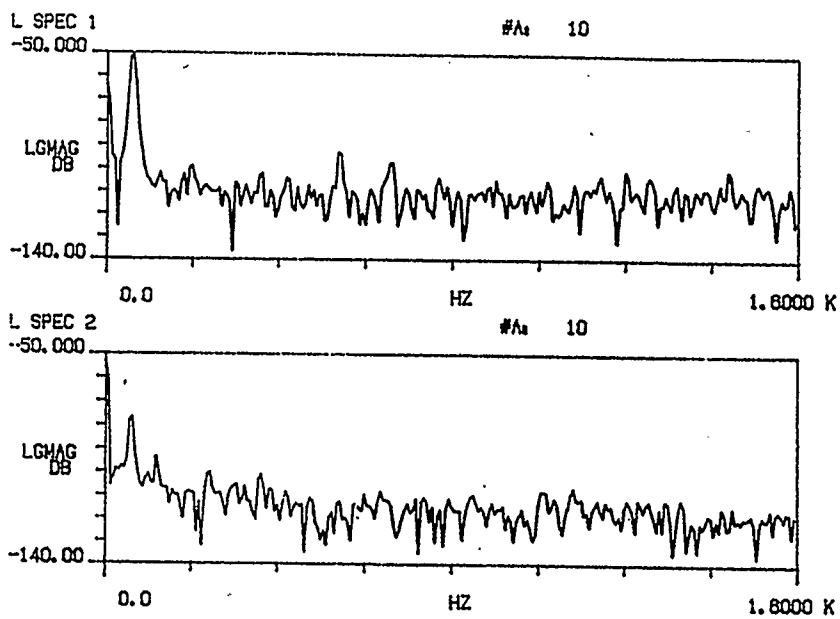
CHAN #	RANGE	AC/DC	DELAY	CAL (EU/V)
* 1	500 mV	AC	0.0 S	1.00000
* 2	500 mV	AC	0.0 S	1.00000

(a)

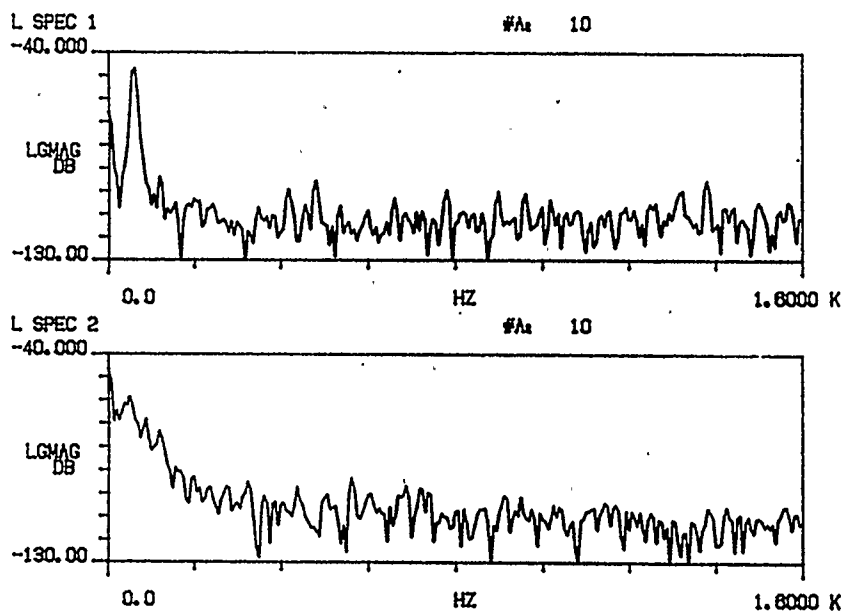


(b)

Fig. 5.3. Spectra of the mechanical (upper) and electrical (lower) channels with flow rig turned off : (a) Display parameters (b) Accelerometer disconnected (c) Accelerometer on optics bench, connected to the amplifier (d) Laser turned on, Accelerometer as in (c)



(c)



(d)

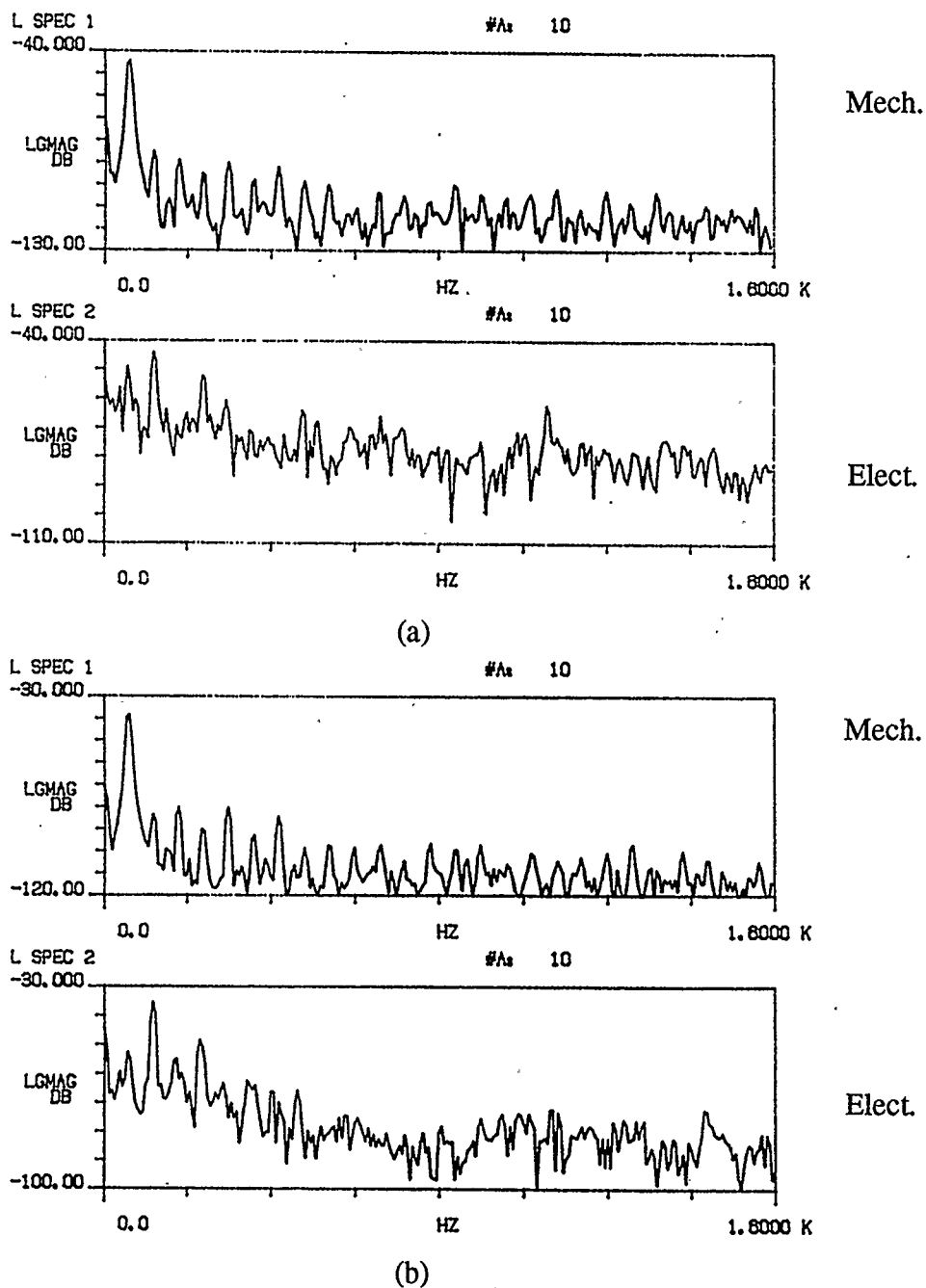
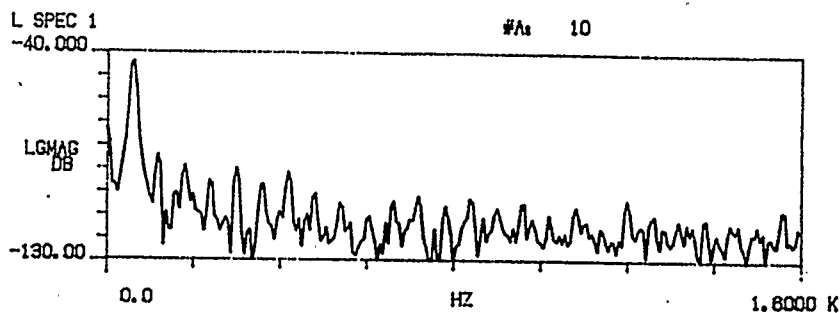
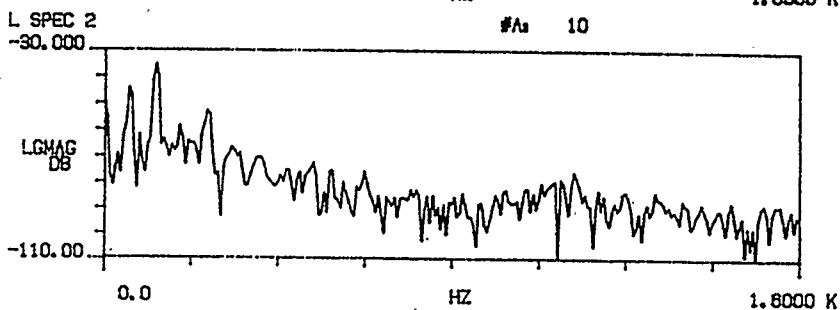


Fig. 5.4. Spectra of the mechanical (upper) and electrical (lower) channels at different pressures and flow rates : (a) Full rotameter range, 24 psi
 (b) Same flow rate as (a), 0 psi (c) 40 % of rotameter range, 25 psi
 (d) 20 % of rotameter range, 28 psi

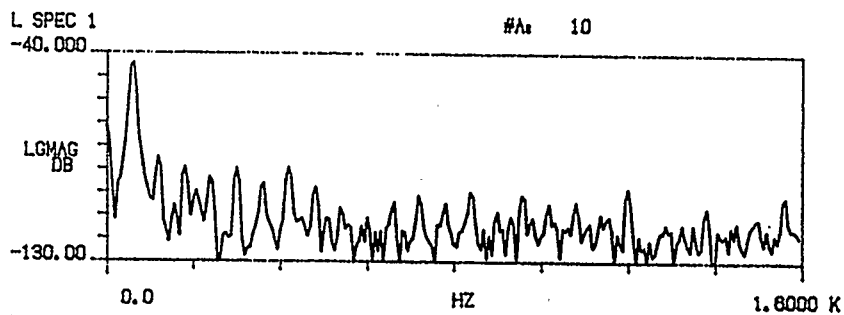


Mech.

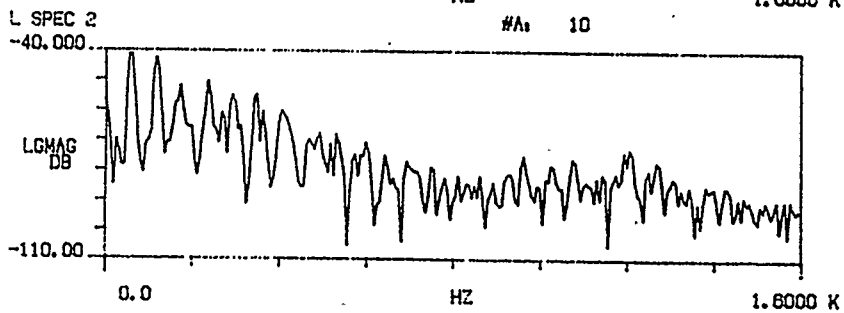


Elect.

(c)



Mech.



Elect.

(d)

Contrasting to the conditions of zero flow and zero pressure at the test section of Fig. 5.3.d, Fig. 5.4.a gives the spectra obtained with a flow of full rotameter range, at the highest possible pressure. With the pressure reduced to zero, at the same flow rate, Fig. 5.4.b is obtained. With the flow rate reduced at the nearest possible pressures Fig. 5.4. c and d are obtained. Obviously, the amount of vibration coupling depends on the conditions on the test section. However, no frequency component can be found that shifts consistently with the rate of flow, or pressure, nor a frequency peak that changes in amplitude in such a way. The coupling of vibrations to the optical and electrical channel through the fiber can be explained by the changes in the speckle pattern. This is the modal power distribution in the fiber induced by the fiber vibration inside the flow and on the test section and since this depends on the pressure and flow conditions, it can give rise to the observed spectra.

It is thus concluded that a normal fiber cannot, by itself, be a sensitive intensity transducer in a flowrate measurement, nor in a pressure measurement in the corresponding range. A part of the fiber modified in some way as to be sensitive to flowrate effects must be used to enable intensity-modulated sensing of the flowrate. The possibility of having a tapered section of the fiber in a vortex shedding meter configuration is investigated thoroughly in the following chapters.

Chapter 6

THE VORTEX SHEDDING PROCESS

Among the flowmeter configurations utilizing optical fibers as sensing elements vortex shedding arrangements are seen to be most suited to general industrial applications. If an intensity-modulated sensing scheme can be devised so as to be used in these meters they would be realizable as simple systems as well. The principle of operation and basic design considerations of vortex shedding meters are presented in this chapter. The use of optical fiber tapers, as intensity-modulated sensing elements, to detect the shedding frequency in such flow meters is discussed in detail in the next chapter.

6.1. Vortex shedding past an infinite circular cylinder

When an obstructing object is inserted into a uniform flow, the flow pattern and forces exerted on the object depend on its shape and the corresponding Reynolds number. For a circular cylinder the Reynolds number is defined as :

$$\text{Re}_{st} = D_{st} \frac{v}{\nu} \quad (6.1)$$

where,

D_{st} = diameter of the cylinder,

v = velocity of approach of the fluid,

ν = Kinematic viscosity,

and the subscript "st" refers to the obstructing strut. At a Reynolds number in the range 2 to 30, boundary layer separation takes place at some point before reaching the rear end of the cylinder and a closed wake with two eddies rotating in opposite direction form past the cylinder. With increasing Reynolds number the wake elongates and finally becomes unstable, oscillating periodically for a Reynolds number of 40 to 70. Starting in the range of Reynolds number from 45 to 90 depending on the turbulence in the main stream and the nearness of other solid bodies or walls, eddies break off, at a constant frequency, alternately from each side of the cylinder. These wash downstream forming a stable vortex street past the cylinder known as the Von Karman Vortex Trail [43,44]. Fig. 6.1 illustrates the development of vortex separation and the vortex street.

A regular vortex street can be observed up to a Reynolds number of 120 to 180 [19,45], in the so called laminar vortex shedding range. In this range, vortices are shed in phase along the circular cylinder, and the flow pattern is still two dimensional. Beyond the above range and up to a critical value of 200000 or so, vortices continue to separate from the cylinder at constant frequency, but they form random turbulence down stream, and a regular vortex street is not perceived.

The frequency of vortex shedding is given by :

$$F = S \frac{v}{D_{st}} \quad (6.2)$$

where S is the Strouhal number, given by the empirical formula :

Fig. 6.1.a. Development of vortex separation past a circular cylinder

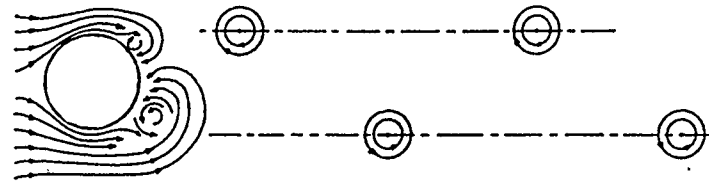
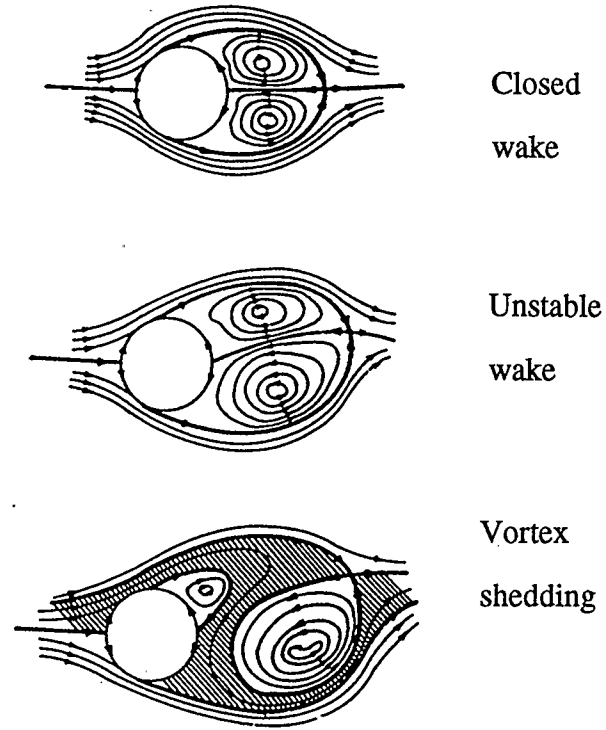


Fig. 6.1.b. The vortex street

$$S = \frac{A}{Re_{st}} + B + C Re_{st} \quad (6.3)$$

with A, B, and C being constants. In the laminar range, these constants take the following values [45] :

$$A = -3.3256, \quad B = 0.1816, \quad \text{and} \quad C = 1.6 \times 10^{-4}$$

A two term approximate formula is given by Roshko [46] :

$$S = 0.212 \left(1 - 21.2 / Re_{st} \right) \quad (6.4)$$

While in the range $300 < Re_{st} < 2000$, the Strouhal number is approximated by :

$$S = 0.212 \left(1 - 12.7 / Re_{st} \right) \quad (6.5)$$

Increasing the value of Re_{st} causes a sharp drop in the Strouhal number to be observed at some critical value. In the super critical range the viscous forces become negligible compared with fluid inertia and eddies form and leave the cylinder almost randomly.

The forces exerted on the obstructing cylinder are composed of two components - drag and lift forces. Drag forces push the cylinder in the flow direction whereas lift forces act cross wise. In the range before boundary layer separation friction forces dominate and there are no lift forces. With boundary layer separation drag forces deviate largely from following the skin friction theory. The start of wake

oscillation marks the appearance of a time varying drag component with oscillating lift forces. The shedding of each vortex off the strut induces an unbalanced lateral force on it giving rise to a periodic lift. Drag forces on the cylinder are affected by the flow pattern and a periodic component of the drag with a frequency of twice the vortex shedding frequency is produced. In the super critical range the boundary layer around the cylinder becomes turbulent and a sharp decrease in the drag coefficient is observed.

Alternating lift forces may cause forced vibration of the cylinder. Complicated situations result with flexible cylinders where the cylinder vibration affects flow and vortices are shed at a shifted frequency. Such effects are discussed in the following part of this chapter.

6.2. Effects of non-ideal conditions on vortex shedding

In a practical application of the vortex shedding phenomenon it is not expected that the ideal conditions of a two dimensional unconstrained flow exist. Moreover, a strut is not always rigid enough that the vortex shedding frequency is not affected by its vibration. In fact, in some optical fiber vortex shedding flow meter realizations the optical fiber itself is used as a strut to detect the vortex shedding frequency. The vibration of the fiber can not be avoided and is used to modulate the optical signal travelling through it. The main factors affecting the vortex shedding process are lateral confinement of the flow, strut vibration, end conditions and velocity and diameter variation along the strut.

Lateral confinement results generally in an increase in the Strouhal number over that of unconfined flow and an increase in the drag. In the case of a rigid circular cylindrical strut [47], an increase in the Strouhal number from around 0.2 to 0.325 is induced by confining the flow to a width of twice the strut diameter. The mean drag and lift forces are enhanced by confinement while fluctuating drag becomes less and the bandwidth of lift fluctuations increases. The value of the critical Reynolds number decreases with confinement. A reduction from a value 280,000 to 100,000 was reported when confining the flow to two strut diameters. The effects of channel confinement can be considered very small for channel widths of 6 strut diameters or more.

When a flexible or flexibly mounted strut is used in a vortex shedding arrangement the oscillating lift forces force it into crosswise vibration whilst the effect of oscillating drag forces is normally smaller and less effective. Vibration of the strut affects flow pattern, hence drag and lift forces [48], and a phenomenon known as lock-in takes place when a strut oscillates at frequencies near the expected rigid-strut, Strouhal frequency. Vortices are then shed at the frequency of strut oscillation. In the general case, the complex system of flexible strut and fluid wake oscillates in a lock-in mode at a frequency shifted from the Strouhal frequency towards the nearest resonant frequency of natural vibration of the strut. The amplitude of oscillation of the strut becomes largest when both frequencies coincide. The oscillation frequency of the system locks to the strut resonance frequency over a range of expected Strouhal frequencies and for a flexibly mounted rigid cylinder this range extends from 0.95 to 1.28 of the resonance frequency[49,50]. For a minimum effect on the shedding

frequency the natural resonance frequencies of the strut must be as far as possible from the Strouhal frequency.

Conditions at the end of the strut affect homogeneity of the vortex formation and shedding frequency span wise and in the areas adjacent to walls or end plates the shedding frequency is lowered from the frequency at the middle of the strut. Mixing of the two frequencies occurs at the junction points, or nodes and the affected area along a circular strut depends on its diameter. For small diameters, 2 mm or less, in the laminar range of vortex shedding this area extends to 15 diameters or less on each side of the strut [51]. The extent of the region relative to the strut diameter gets less with larger strut diameter. This also depends on the plate diameter in case of end plates. When the length of the strut is short so that the two end nodes coincide they cancel out. In this case, vortices are shed from the whole span at a new frequency which is less than the Strouhal frequency but larger than that observed in the end regions before. The laminar range of vortex shedding is then extended to Reynolds number of around 250 with onset of shedding at 60.

In order to take these end effects into consideration for the case of a strut spanning a pipe for velocity measurement, the strut must have a diameter less than one thirtieth of the pipe diameter and the frequency measuring detector must be located at the middle point of the strut. This arrangement will detect the frequency at the area far from ends as the shedding frequency. On the other hand if it is preferred that the whole strut is affected and there be no nodes, the strut diameter must be much larger than the above value so that vortices are shed at a single frequency all along the strut. In this case the position of the frequency detector is rather arbitrary

but it would limit the range of the measurement to lower velocities if the laminar range is not to be exceeded. The author of this thesis did not succeed in getting hold of data, in the published literature, describing the extent of end regions beyond this range. It is expected though that these regions become more confined to the strut ends due to the lack of formation homogeneity and in-phase shedding of vortices in the transition range. End conditions also affect the direction of vortex shedding along the strut, which in turn affects the frequency of vortex separation and the frequency decreases as the shedding angle increases. The Strouhal number corresponding to oblique shedding S_{θ} is related to the Strouhal number for parallel shedding, S by the relation :

$$S = S_{\theta} / \cos(\theta) \quad (6.6)$$

θ being the oblique shedding angle [45].

A model of cell formation in the laminar range, past a rigid circular strut with span wise variation in the flow velocity and diameter was recently investigated [52]. The model is based on representing wake oscillation as infinitesimal coupled oscillators. This accounts for cell formation along the strut. The frequency spectrum of layer displacement past a tapered strut is shown to be composed of multiple discrete peaks corresponding to dominant frequencies of the cells. We have conducted experiments with a fiber taper as the strut and obtained similar spectra. These experiments are discussed in detail in the following chapter of this thesis. A model for such a flexible taper strut is however expected to be more complicated than the model mentioned above.

As a conclusion to this section, it is seen that due to the effects described on the vortex shedding process, a vortex shedding flow meter must be calibrated throughout its range before being used for flow measurement.

Chapter 7

INTENSITY MODULATED FIBER OPTIC VORTEX SHEDDING FLOWMETER

Investigation of the effect of pressure and flow rate on a normal fiber immersed in the flow has indicated that intensity modulated sensing of these parameters could only be possible by incorporating special fiber parts, transducing these parameters into variations of the intensity of light within the fiber. A pressure sensor that utilizes bent tapered single mode fibers has recently been reported [53]. This initiated our interest in using fiber tapers as sensing elements in flowmeter arrangements, the simplest of which was the vortex shedding flowmeter.

Single mode fiber tapers were made using available equipments and characterized for their bending loss at two different operating wavelengths, where they act as multimode and singlemode light guides. Their characteristics are qualitatively explainable based on studies previously published in the literature. Local normal modes and modal coupling techniques were studied and applied to the modeling of fiber tapers under single mode operation. A numerical model was implemented and results of the computations compared to experimental bending loss characteristics. The proposed vortex shedding meter was experimentally studied and proved feasible.

7.1. Optical fiber tapers

Changing the diameter of an optical fiber causes its propagation modes to reconfigure in profile and propagation constant so as to propagate along the new guiding structure. At the same time nonuniform taper boundaries induce mode coupling between modes which were otherwise uncoupled. A gradual taper can induce very small coupling between the modes. Such tapers were studied for use as mode transformers [54-56] to facilitate coupling light in and out of single mode fibers whereas up-tapering of these fibers has been used to achieve beam expansion [56-58]. Reducing the diameter of single mode fibers was also used for beam expansion [59,60].

Other devices make use of the coupling between modes as well as modal size expansion. In a fused taper coupler guided modes are coupled to each other while overlapping, in the tapered region. In a single fiber taper guided modes are coupled to cladding modes and since this coupling depends on the geometry of the taper it can be used to sense geometrical deformations such as bending of the taper [61,62].

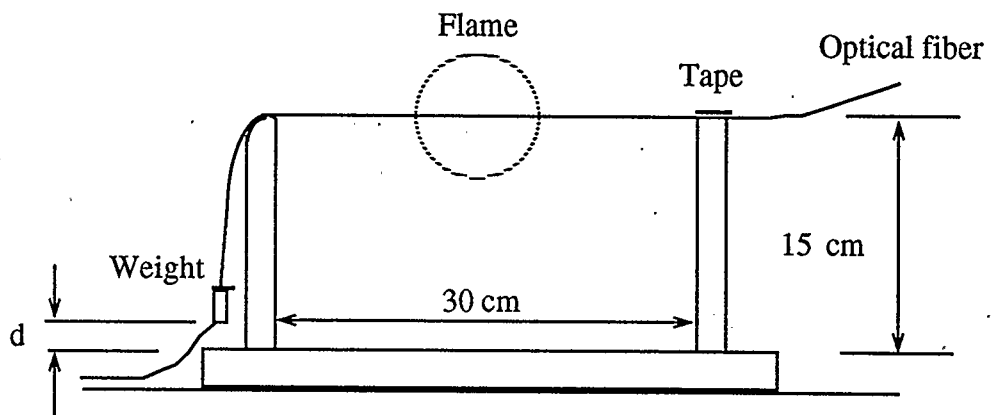
Fiber tapers are made by applying tension to the fiber while exposing the section where a taper is to be produced, stripped of its coatings, to a heat source. Stripping the primary coating off the fiber was our first step to produce tapers. Initially chemical methods for removing the coating from the fiber taper sections were investigated. However since the coating is intended to be chemically resistant this was not achieved. Fiber coatings are usually made of silicone, polymers such as perfluorinated ethylene propylene (FEP), polyurethane, or plastics [63]. We had no

data describing the coating of the fibers available for our use, and these fibers were actually discontinued in production. Toluene, acetone, and hydrochloric acid were tried and no satisfactory effect produced. Chemical experts advised the use of boiling Toluene, or Xylene to get rid of the coating. These are very dangerous and would have required special handling and safety arrangements. Contacting the technical staff of Northern Telecom we were advised not to try chemical treatments since the primary jacket is intended to be very resistant, and hard to etch, thus any substance that is harsh enough to remove the coating will be very dangerous to work with. A mechanical removal of the coating is thus preferred. A Miller Stripper type 103-5 was suggested but it was not available at local distribution agencies. We decided to try removing the coating manually, which actually can be done with some patience and experience as well. We discovered later on that burning the coating was the best way to remove it as it had been noticed that when heating the fiber the primary coating gets burnt off at temperatures too low to melt the fiber.

A bare nickel chromium wire cord coiled in a 5 mm diameter and 1.5 cm in length was used to heat the fiber. No effect other than burning the coating resulted. A smaller coil of 3 mm diameter, and 1 cm in length was also used and the fiber did not soften. High currents up to 40 Amps in a cross section of 0.785 mm^2 were applied to the heater until the wire melted without affecting the fiber. Despite the fact that the melting point of nickel chromium is higher than that for silica it seems that the presence of an air gap between the fiber and the cord prohibited the reaching of sufficiently high temperatures to melt the fiber.

Finally we tried using a burning flame to soften the fiber and it did work. An oxygen - natural gas flame was used to produce tapers with the help of a small wooden rig which was used to apply weights to the fibers, so as to stretch them when they softened. This rig is drawn in Fig. 7.1. The fiber used was a communications fiber that is single mode at 1300 nm. This enabled us to investigate both single mode and multimode tapers using sources at 1300 nm, and 633 nm wavelengths with the same fiber taper parameters. Table 7.1 gives data on the fiber used. Stretch distances of 0.5, 1, and 1.5 cm were tried with weights ranging from 5 to 16 grams. Tapers that survived the careful but inexperienced handling were almost all only those produced with 0.5 cm stretch distance. Increasing the stretch distance for a given weight or decreasing the weight for the same stretch distance elongates the taper, giving thinner and longer narrow parts. The dimensions of the produced tapers were measured under a precision Mitutoyo TM-101 microscope. A taper waist and distance to the beginning, and end of the taper were measured, since it was thought unnecessary to measure profiles point by point. Preliminary review of the published analysis of tapers revealed that a linear taper model gives good agreement between theory and experiment.

Surviving tapers were characterized for their transmission versus bending characteristics using a manual method where the fiber on one side of the taper was held under a grooved holder, and on the other side, the fiber was taped on a plate indicating the bending angle. The holder used was made of brass with a trapezoidal groove of approximately 450 μm opening, 220 μm base, and 200 μm depth, so that the 125 μm diameter fiber resided unstressed in the groove. Transmission, relative to



d = stretch distance

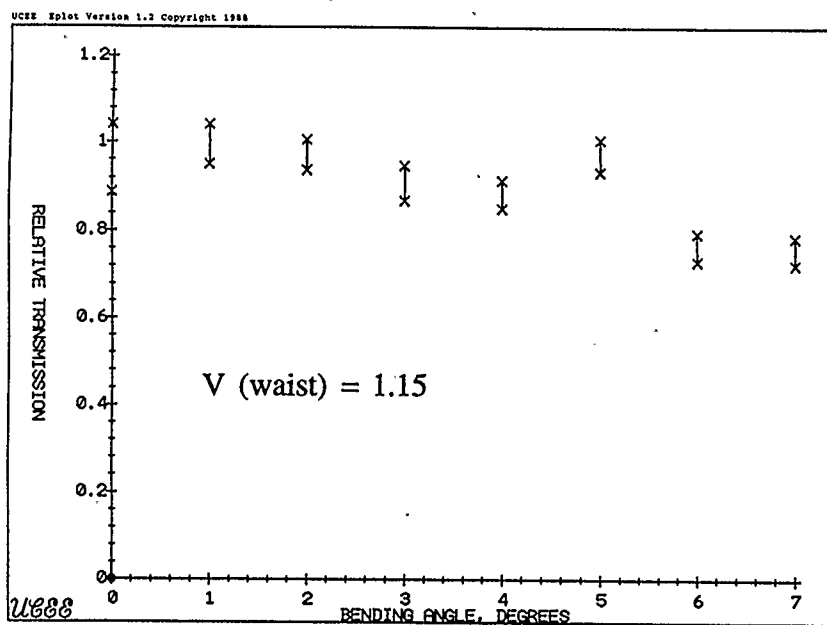
Fig. 7.1. The rig used to make fiber tapers

Table 7.1. Parameters of the single mode fiber used to make tapers

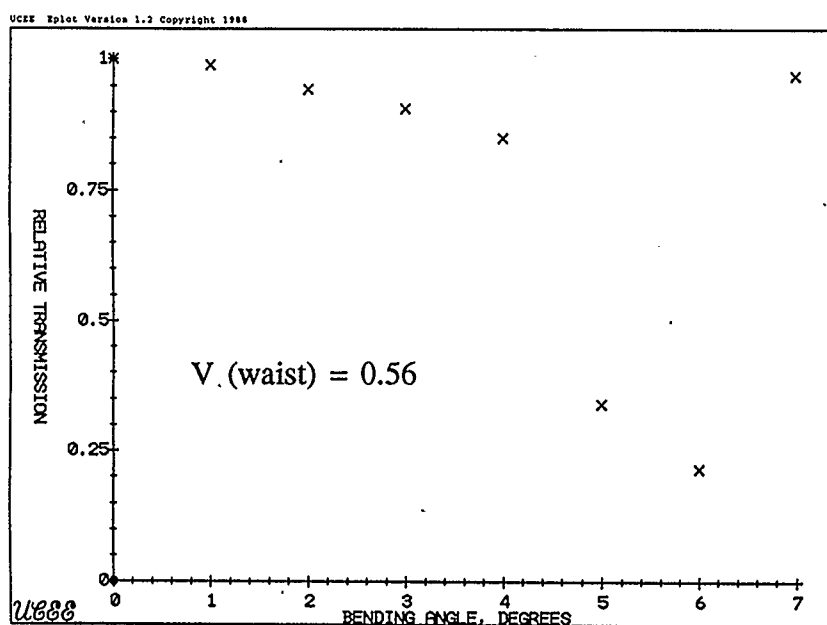
Parameter	Value
Cladding diameter	$125 \pm 2.0 \mu\text{m}$
Mode Field Diameter	$9.5 \pm 1.0 \mu\text{m}$
Zero Dispersion wavelength	$1310 \pm 10 \text{ nm}$
Cutoff Wavelength	$1245 \pm 65 \text{ nm}$
Coating Diameter	$250 \pm 15 \mu\text{m}$
Attenuation	1 - 2 dB / km

zero-bending transmission was measured at bending angles spaced 1 degree. Since connectors and fiber end quality added an undetermined amount of loss it was not possible to measure the zero bending taper loss, by comparing the taper transmission to that of a similar, untapered fiber part.

Transmission versus bending characteristics of a taper with 30.48 μm waist diameter, 5.8 mm, and 4.65 mm distances to the ends of the taper, which was then at about 110 μm diameter, at wavelengths of 633 nm and 1300 nm are shown in Fig. 7.2. a and b, respectively (vertical bars indicate the range of variation in transmitted power). This taper was produced with a tension weight of 12.4 grams and a 0.5 cm stretch distance. For the 633 nm wavelength bulk optics were used to couple the He-Ne laser light into the fiber and the maximum transmitted power through the taper was 14 μW . Fluctuations in transmitted power were unavoidable and were believed to be due to small vibrations of the taper part under the holder and the fiber at the taped end. For the 1300 nm wavelength, mechanical alignment of the laser pigtail and the fiber in a grooved Aluminum fixture were used to couple light in and the maximum transmitted power in this case was 19.4 nW. Fluctuations in transmitted power were too small to be detected. Fig. 7.3. a and b shows the characteristics of a taper with 86.36 μm waist diameter, 3.22 mm, and 5 mm distances to the ends of the taper, at 120 μm diameter, at wavelengths of 633 nm and 1300 nm respectively. The taper was produced with the same weight and stretch distance as the previous one but happened to have different dimensions and the maximum transmitted power through the taper was 17.13 μW at 633 nm and 26.7 nW at 1300 nm.



(a)



(b)

Fig. 7.2. Experimental relative transmission versus bending of a fiber taper with $30.48 \mu\text{m}$ waist diameter, 5.8 mm , and 4.65 mm to the ends of taper at 633 nm (a), and 1300 nm (b)

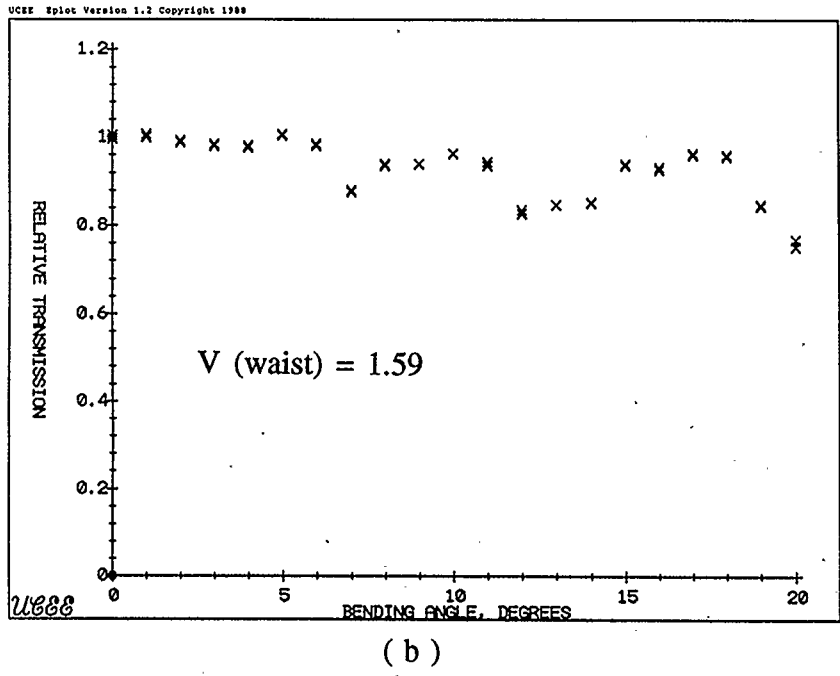
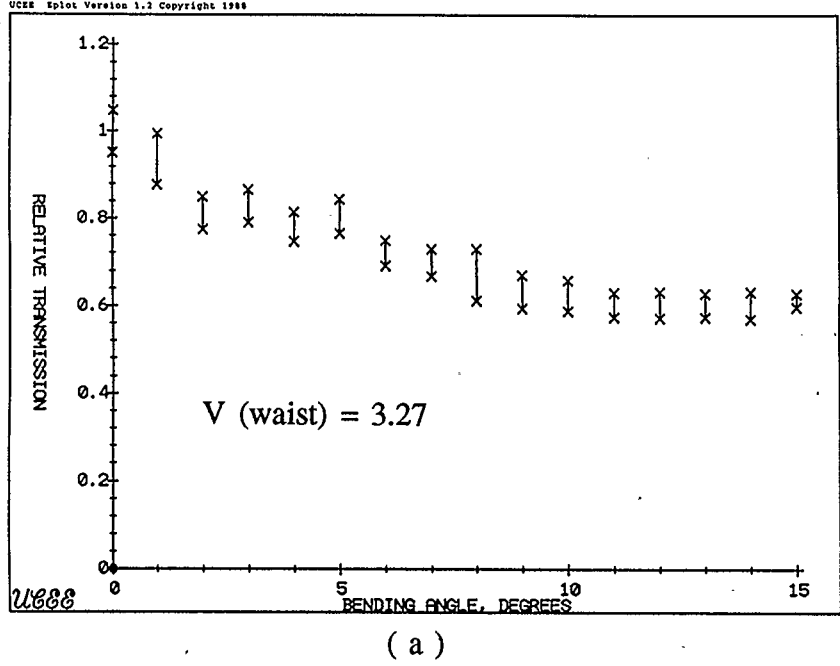


Fig. 7.3. Experimental relative transmission versus bending of a fiber taper with 86.36 μm waist diameter, 3.22 mm, and 5 mm to the ends of taper at 633 nm (a), and 1300 nm (b)

When the diameter of an optical fiber is reduced along a taper its waveguiding properties change. The normalized frequency, at any section of the taper, is defined as :

$$V = \frac{2 \pi}{\lambda_0} (N A) \cdot a \quad (7.1)$$

where λ_0 is the free space wavelength of the exciting wave, a is the core radius and $N A$ is the fiber numerical aperture. In a multimode fiber where V is large, thus allowing many modes to propagate, the effect of tapering is to cause coupling among these modes and coupling to cladding modes of the fiber. These are modes guided by the fiber - outer medium interface, which defines another multimode waveguide, with normalized frequency V_{cl} , given by :

$$V_{cl} = \frac{2 \pi}{\lambda_0} (n_{cl}^2 - n_{ext}^2)^{1/2} \cdot b \quad (7.2)$$

where n_{cl} is the refractive index of the fiber cladding, n_{ext} is that of the outer medium, and b is the fiber cladding outer radius. A part of the core power coupled to cladding modes is normally coupled back to the core modes whilst the rest of it stays in the cladding until eventually lost by coupling to radiation or by absorption. Bending of the taper can significantly affect coupling between modes. Modes of different azimuthal periodicities which are not coupled in a straight taper now couple to each other and this modulates the amount of power eventually lost from guided modes in the coupling process.

When the V -number is reduced so that one of the guided modes of the fiber

passes through its cutoff this mode now couples all of its power to the cladding modes [54], while other modes participate only partially in the coupling process and suffer partial profile deformation. This enhances the power exchange in the taper giving rise to more modulation of transmission with bending. At 633 nm the fiber used has four guided modes, three of which are almost degenerate, the TM₀₁, TE₀₁, and HE₂₁ composing the LP₁₁ mode and it can be assumed that along a taper the core to cladding radii ratio is constant [55,64]. For the taper of Fig. 7.2 at 633 nm, the V-number at the taper waist is 1.15, hence, these modes participate with all their guided power in the coupling process. This is why we have more modulation of the taper transmission with bending, as compared to the transmission of the taper of Fig. 7.3.a, where $V = 3.27$ at the taper waist, and all guided modes participate less effectively in the coupling.

In the case of single mode operation, the normalized frequency is already smaller than 2.405 allowing only one guided mode, the HE₁₁ mode, to propagate in the core. This mode deforms in profile and couples to cladding modes as the normalized frequency decreases. At a value of 1.0 the modal profile resembles that of the fundamental cladding mode, and couples completely to it [64]. Actually, at such low V-number, the core is so small that it has insignificant effect on the guiding properties of the outer guide composed of the cladding and the external medium. For the fiber used this corresponds to an outer cladding diameter of 54.262 μm . For fiber diameters larger than this value the coupling of the guided mode to cladding modes is partial. At the above value of $V = 1.0$ very efficient coupling of power to cladding modes occurs. The power coupled is exchanged among cladding modes in the taper

part where V is less than 1, and the amount contained in the fundamental cladding mode at the up-tapering section with $V = 1$, is coupled to the guided core mode. This process seems to dominate coupling at other sections of the taper [65] and it accounts for the larger modulation of transmission, in the case of Fig. 7.2.b, while not that much modulation appears in Fig. 7.3.b.

Since the periodicity of coupling with bending angle is different for each guided mode the transmission characteristics in multimode operation has more minima, and maxima, in the same bending range, than in single mode operation. In particular, the first minimum of transmission, which determines the range most useful for sensing applications, occurs at lower bending values.

Based on the above explanations it is concluded that single mode fiber tapers with waist diameters giving rise to V -numbers less than unity give maximum modulation of transmission with bending allowing for higher bending-sensor sensitivities. The range of linearity of operation of sensors based on these tapers is expected to be wider, both in transmission variation and angle domain, as compared to using other tapers. It is hard to explain every detail of the taper transmission curves since the coupling process involves power exchange among many modes and is quite complicated. Fortunately for the case of most interest, the single mode fiber tapers having waist regions of $V < 1$ the coupling is dominated by power transfer between the fundamental core, and cladding modes at the ends of these regions and modal coupling among only cladding modes within these regions. Numerical modeling of these tapers was carried out and gives very good agreement with experiment. This model and the underlying theory are discussed in the next section

of this chapter.

Further experimental investigation was carried out on single mode fiber tapers satisfying the above criterion. Figs. 7.4 and 7.5 give the transmission characteristics for two such tapers. A linear approximation to the taper profile for each case is given in the insert and for these tapers the waist region length was also measured. A very short waist, as for the taper of Fig. 7.4, would result in a delayed transmission minimum since the length available for power evolution between the modes, in which bending affects coupling, is short, while for longer waists, the minimum occurs at lower bending values. The maximum transmitted power was 524 nW, for the taper of Fig. 7.4, and 106.6 nW for Fig. 7.5.

It was also noticed that twisting of tapers affects their transmission. In Fig. 7.5, the dashed bars between circles give the transmission of the taper at 180° twist. This twist was applied to the taper on a length of 20 cm from the end of the grooved holders. Twisting the taper resulted in its breaking at 9 degrees while it withstood a bending of 20 degrees when untwisted. Besides the fact that implementing sensor tapers with a given twist could be impractical the effect of twist on the transmission characteristics is found to be small.

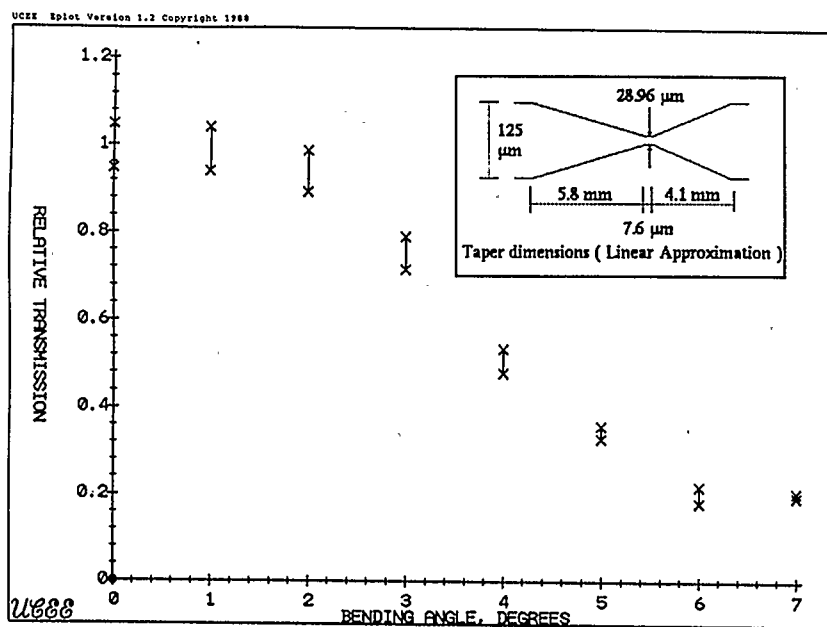


Fig. 7.4. Experimental relative transmission versus bending of the fiber taper

shown in the insert, at 1300 nm

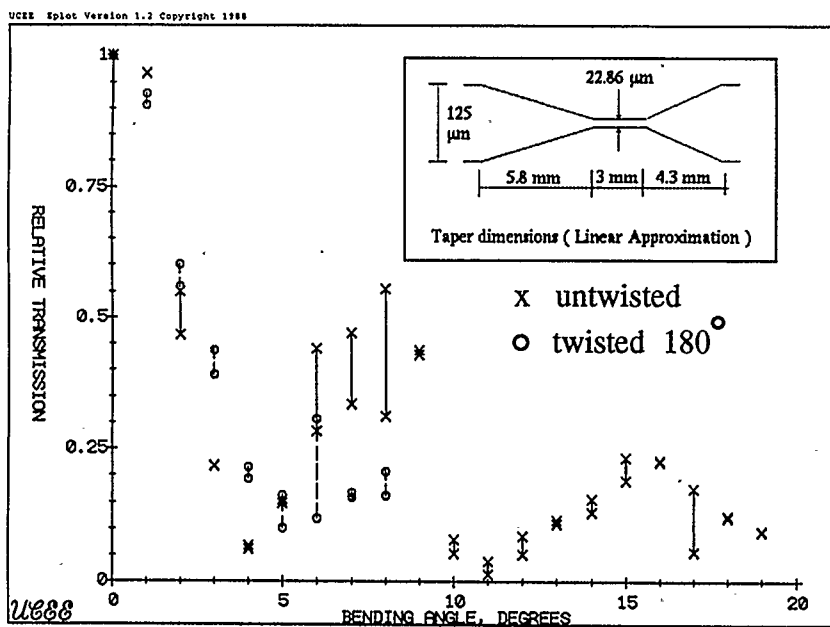


Fig. 7.5. Experimental relative transmission versus bending of the fiber taper

shown in the insert, at 1300 nm

7.2. Theoretical modeling of bent single-mode fiber tapers

As an inhomogeneity of the optical fiber a bent taper can be analyzed by mode coupling techniques where the field is expressed as a combination of different modes, each of which is a self consistent field configuration. Three main approaches of such an analysis use either ideal guide modes, individual section modes, or local normal modes [66]. In the first approach the field at any point inside the bent taper is described in terms of the modes of the ideal, untapered fiber, with coupling coefficients varying along the bent taper. In the second approach, modes of the individual taper section are used, with mode mixing at every cross-section between two sections, to determine relative mode amplitudes due to the presence of bending. In the local normal modes approach, modes of a fictitious fiber that coincides with the local cross-section of a bent taper section are used as the basis to express the field in this section with mode mixing of such modes at the junction between two sections.

The first two approaches are cumbersome and unsuitable for analysis of the bent taper. The differences in shape and orientation between cross-sections of the taper make the use of the modes of the ideal fiber inappropriate. The nature of the modes in each section of the taper is complex and mode mixing at the junctions between these sections could have many serious problems particularly in orthonormalization. Thus the second approach is very difficult to pursue. Local normal modes have the advantage that they are already orthogonal to each other and can be easily normalized and the evolution of the optical field along the taper makes this approach even more intuitively conceivable. Using this approach analytical expressions for the power transmitted through a straight fiber taper are obtainable

when either only two guided modes are considered in the coupling [67], or a single mode is coupled to radiation on a tapered guide with infinite cladding [68]. Analytic expressions for the transmitted power through a dielectric slab guide suffering bending can be derived for the case where only one mode is dominant in propagation [69]. Other cases involving many modes, as for the cladding modes of a fiber taper, can only be treated numerically using the same approach [64, 70, 71].

A bent taper is modeled as being composed of many sections each of which has a constant radius that is generally different from adjacent sections radii and is tilted with respect to them except when the bending angle is zero. The optical field within each section is described in terms of modes of an infinite, straight fiber, with the core and cladding radii of that section. At the junction between two sections modal mixing occurs determining the relative amplitudes of the modes in the next section. The model is illustrated in Fig. 7.6. The modes of a straight optical fiber which are self consistent field configurations capable of propagation along the fiber are expressed in parametric form with the core and cladding radii as parameters.

If the step-wise approximation of the taper is close enough and the bending step is small enough, reflections at the junctions between two sections can be neglected [69, 71]. For such a junction, as illustrated in Fig. 7.7, continuity of the transverse component of the electric field across the junction gives :

$$\begin{aligned} \sum_{\nu} a_{\nu}^i e_{\nu}^i(r, \phi) \exp(-j \beta_{\nu}^i z^i) \exp(j \beta_{\nu}^i r \cos \phi \sin \delta) \\ = \sum_{\mu} a_{\mu}^{i+1} e_{\mu}^{i+1}(r, \phi) \exp(-j \beta_{\mu}^{i+1} z^i) + \Phi(r, \phi) \end{aligned} \quad (7.3)$$

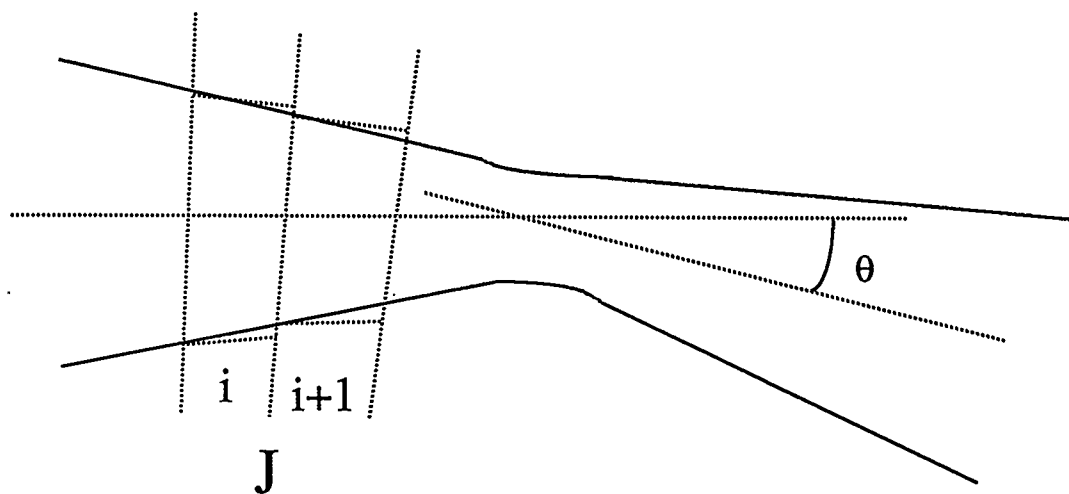


Fig. 7.6. Step - wise approximation of a bent fiber taper

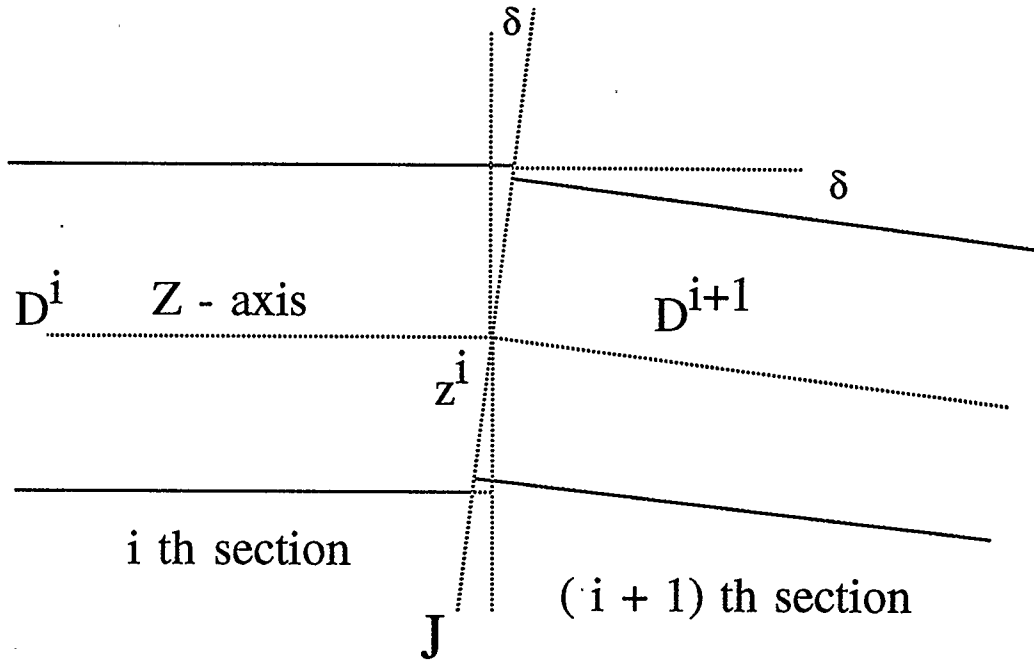


Fig. 7.7. Mixing of local modes at the junction between
two sections of a bent taper

where a_v^i , and a_μ^{i+1} are the amplitude coefficients of the v th guided mode of the i th section, and μ th guided mode of the $(i + 1)$ th section, the transverse electric fields of which are e_v^i and e_μ^{i+1} respectively. r and ϕ are the transverse coordinates in a cylindrical coordinate system with its z -axis coincident with the fiber axis in the i th section. δ is the incremental bending between the taper sections, Φ is the radiation field and j is the square root of -1 .

Taking the cross product of both sides of (7.3) with h_μ^{*i+1} which is the complex conjugate of the transverse magnetic field of the μ th mode of the $(i + 1)$ th section, integrating over the whole interface plane, and making use of the orthonormalization relations between the modes of that section, gives :

$$a_\mu^{i+1} \exp(-j \beta_\mu^{i+1} z^i) = \sum_v a_v^i \exp(-j \beta_v^i z^i) \cdot C_{\mu v} \quad (7.4)$$

where $C_{\mu v}$ is a coupling coefficient given by :

$$C_{\mu v} = \int_0^{2\pi} \int_0^\infty \{ e_v^i \times h_\mu^{*i+1} \} \exp(j \beta_v^i \cdot r \cos \phi \cdot \sin \delta) r dr d\phi \quad (7.5)$$

with \times indicating the cross product. The disappearance of the radiation term of equation (7.3) in equation (7.4) is a consequence of the fact that all guided modes are orthogonal to the radiation field. Since only magnetic fields of these modes are used to get equation (7.4) exact information about the magnitude of radiation is lost

in this step. A more accurate form of (7.4) would contain an integration over radiation modes in addition to the sum over guided modes in the right hand side though this obviously would have complicated the situation much more. Using the set of equations given by (7.4) to get the modal amplitudes a_{μ}^{i+1} , in terms of the amplitudes a_{ν}^i and coupling coefficients $C_{\mu\nu}$, is a valid approximation so long as the amount of radiation is small therefore it can be ignored. This is expected to be the case since the difference in refractive index between the fiber material and the external medium, which is air or water, is relatively high [72]. In matrix form, equation (7.4) casts into :

$$[P_{\mu}] [a_{\mu}] = [C] [P_{\nu}] [a_{\nu}] \quad (7.6)$$

where $[a_{\mu}]$, and $[a_{\nu}]$ are column vectors giving the modal amplitudes a_{μ} and a_{ν} respectively, each of rank M, which is the number of guided modes considered in the analysis. $[P_{\mu}]$, and $[P_{\nu}]$ are diagonal matrices giving the propagation factors :

$$p_{\mu} = \exp(-j \beta_{\mu}^{i+1} z^i) \quad (7.7)$$

$$p_{\nu} = \exp(-j \beta_{\nu}^i z^i)$$

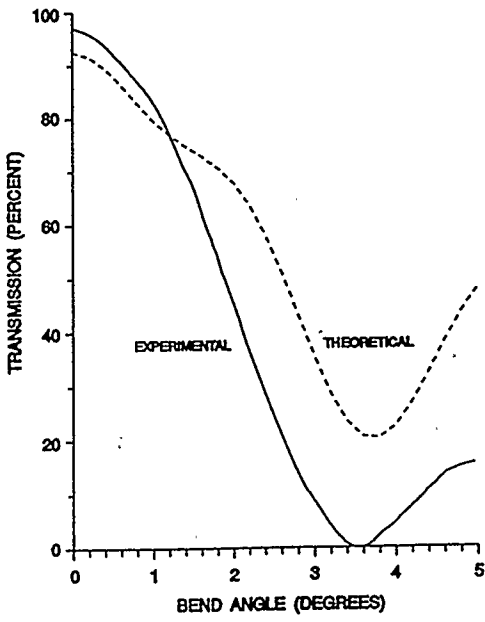
$[C]$ is the coupling coefficients matrix, with $C_{\mu\nu}$ as the element of the μ th row and ν th column. In such an analysis each of ν and μ indicates a two integer

index identifying the angular and radial eigen numbers of the guided mode. If both core and cladding guided modes are to be included, a third integer would be needed for complete mode designation.

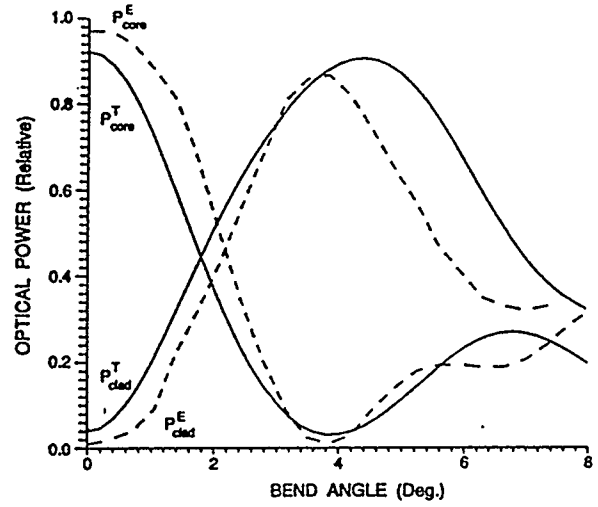
The above analysis simplifies in the case of single mode fiber tapers where the input power is guided initially in the single, core-guided mode. At the taper output, power coupled into this mode is considered to be the transmitted power through the taper since the power coupled to other modes is eventually lost and is not detected at the end of the fiber. For sections of the fiber with V-number given by equation (7.1) less than unity, the field profile of the guided mode is coincident with that of the lowest order cladding-guided mode and the optical power is actually guided by the cladding - external medium interface [73]. Hence, the power guided in a single mode fiber is effectively transferred into this mode at the input section of the taper with V equal to 1. The power remaining in this mode at the output section with V equal to 1 is coupled to the core-guided mode of the fiber and is the portion of power transmitted through the taper. In such a case an intermodal mixing analysis performed only in the taper section with $V < 1$ and including only cladding modes could give an accurate description of the transmitted characteristics of the taper, proving that the coupling between modes in the region of $V > 1$ is only marginally of any effect [71]. The resulting model would then be possible to implement numerically with little complexity and was actually implemented using the C-language. Equations (7.5) and (7.6) are the heart of the program together with a subprogram which computes the modal fields at a given section of the fiber taper. This program was created starting with the Bessel functions with integer orders available in the

standard C-library and was 1057 lines long. Equation (7.5) was computed using a double integration function employing repeated one-dimensional integration. Real and imaginary quantities were treated separately and equation (7.6) was performed repeatedly, starting at $z = 0$ where the propagation matrices are unit ones. We compared our simulation results to those reported by other investigators who used other fibers which are single mode at 633 nm. Fig. 7.8 shows how our computations compare to those of references [53, 71]. In [53] the linearly polarized modes approximation [64] was used in computing modal profiles involved in the computation of the coupling coefficients. In our computations we used the exact modes as in [71]. The modal fields used and their orthonormalization relations are described in detail in [74]. Figs. 7.9, and 7.10 show how the simulation results compare to our experimental investigations at 1300 nm.

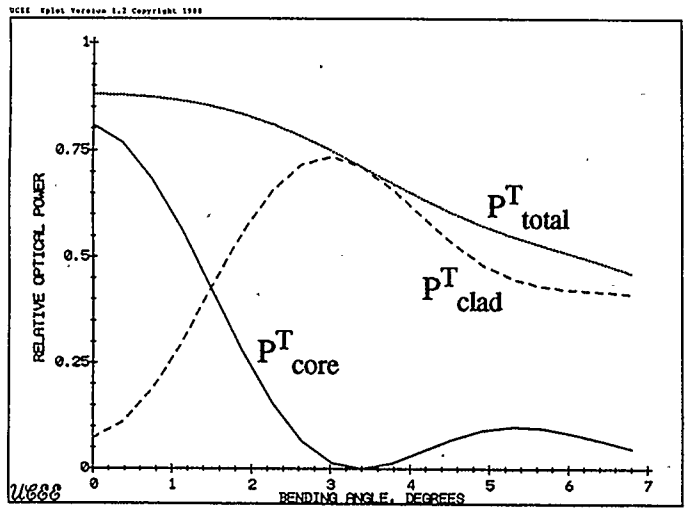
Two important parameters of the simulations are the number of grid points used in computing the integrations of equation (7.5) and the number of sections used in modeling the taper. Unless a reasonable number of grid points is used the coupling coefficients are not actually computed but rather very crudely approximated. This can be seen by checking the orthogonality relations between modes in case of zero bending. Increasing the grid points increases the simulation time almost linearly, with a large proportionality factor, since these integrations are computed every step. An increase in the grid points over 20×20 for the 1300 nm simulations and 32×32 for the 633 nm case reported in the literature was found to give only marginal improvement in the results. The number of sections used in approximating the taper must be large enough so that equation (7.3) is valid and reflections are negligible .



(a)



(b)



(c)

Fig. 7.8. Relative power as a function of bending angle for a taper with 18.75 μm waist diameter made from a fiber that is single mode at 633 nm. Experimental P^E and theoretical P^T results shown as per Ref. [53] (a), [71] (b), and as obtained by our program (c)

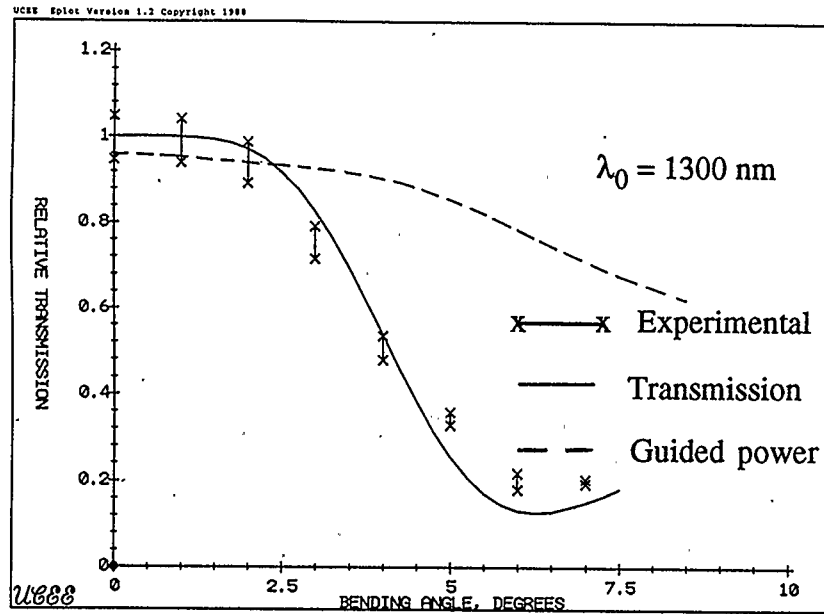


Fig. 7.9. Relative transmission and fractional power guided in the modes considered in the analysis - for the taper of Fig. 7.4

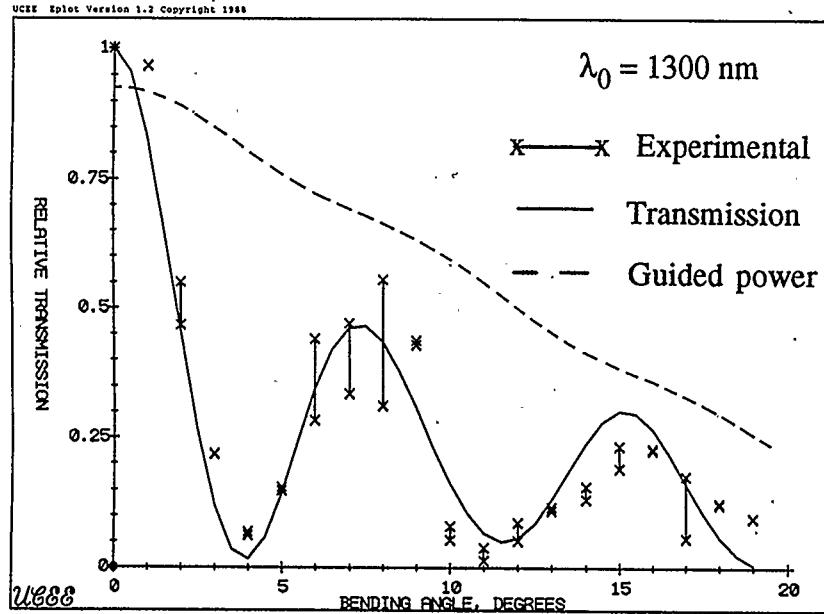


Fig. 7.10. Relative transmission and fractional power guided in the modes considered in the analysis - for the taper of Fig. 7.5

This can not be checked out however, except by comparing the ultimate simulation results with the general shape of the experimental bending characteristics. The distribution of bending increments has a small effect on the location of the minima of the bending curve. Two ways to include bending increments in the analysis were tried, in the first one a bending increment proportional to the axial length of the section was used, which means that physically the taper is assumed to be bent on a circular arc. This generally resulted in minima shifted to values lower than experimental ones. The other way to include bending was to divide the bending angle by the total number of sections used and to vary the proportion of sections in parts of the taper as reported in [64]. Coinciding first minima were generally obtained with more bending in the taper waists than proportional to the axial length of the waist. Since the taper waists have smaller cross-sectional moments of inertia it is expected that more bending is induced at the waists, than at other sections of the taper. The exact bending distribution for any given conditions of a taper is very difficult to define due to the inhomogeneity in radius along the taper axis.

Despite using only a limited number of guided modes in (7.4) an estimate of the relative amount of power coupled to higher order and radiation modes, not included in the analysis, can be estimated by adding up the power guided in all modes considered. The difference between this sum and unity, according to equation (7.4), represents that power. This estimate of course is not exact since reflections at the section interfaces and the rest of equations replacing (7.4) if other guided and radiation modes had been included are just discarded. Nevertheless, it seems that solving the resulting set of equations provides for a good estimate of the power in the

modes surpassed. The dotted lines in Figs. 7.9 and 7.10 give the sum mentioned above. It is noted that the difference between this sum and unity gets larger with increased bending and the fitting of computed transmission to experimental measurements gets poorer. At such small angles the incremental bending at the junctions between sections is too small to affect reflections provided the number of sections is not too small, while coupling to higher order and radiation modes could significantly increase. The model developed thus gives a good fit between simulation and experimental results for a practical range of bending angles beyond which the accuracy of simulation falls off somewhat due to increased coupling to modes not included in the model. Since the modal fields at 1300 nm are less confined to the fiber than at 633 nm and hence more coupling to higher order and radiation modes is expected to take place, the accuracy of simulations at this wavelength deteriorates more rapidly with increasing bending as compared to simulations at 633 nm. This in our opinion may help to explain why previous investigators chose to show comparisons between simulations and experiment only at 633 nm [53], [71], while also reporting experimental investigations at 1150 nm [64].

In our simulations, seven participating modes were used, which is similar to the approach of other investigators. The simulation time was approximately quadratically proportional to the number of modes included. A simulation ran for about 20 hours user's time computing the transmission every half of a degree, over 20 degrees, utilizing about 90 % of the CPU of an AIX supercomputer server with 25.2 million floating point operations per second. The amount of memory used was very small compared to the server capability. Runs at 633 nm lasted roughly three times

longer than those at 1300 nm even though computing only half the number of points. This is due to the increase in grid points and number of sections needed to achieve the same accuracy of simulation.

As we intended to use fiber tapers to detect the frequency of lift forces in a vortex shedding flowmeter arrangement it was important to investigate the effect of changing the external medium from air to water, since this is used to conduct our proof of concept experiments and will be reported in the next section of this chapter. We were unable to investigate experimental taper transmission versus bending in water. Changing the refractive index of the external medium from 1.0 for air to 1.333 for water resulted in small changes in the simulation results, as displayed in Figs. 7.11, and 7.12. The same simulation parameters were used in both cases. At small bending angles the difference between taper transmission in air and in water is very small since the guide composed of the fiber in the fluid is still strongly guiding and most of the field is confined in it. At larger bending angles the change of refractive index starts to be of effect since more spread of the field in the external medium occurs. As the difference between the sum of power contained in the modes and unity is larger for water it is expected that the fit of simulation results to actual taper characteristics will be poorer.

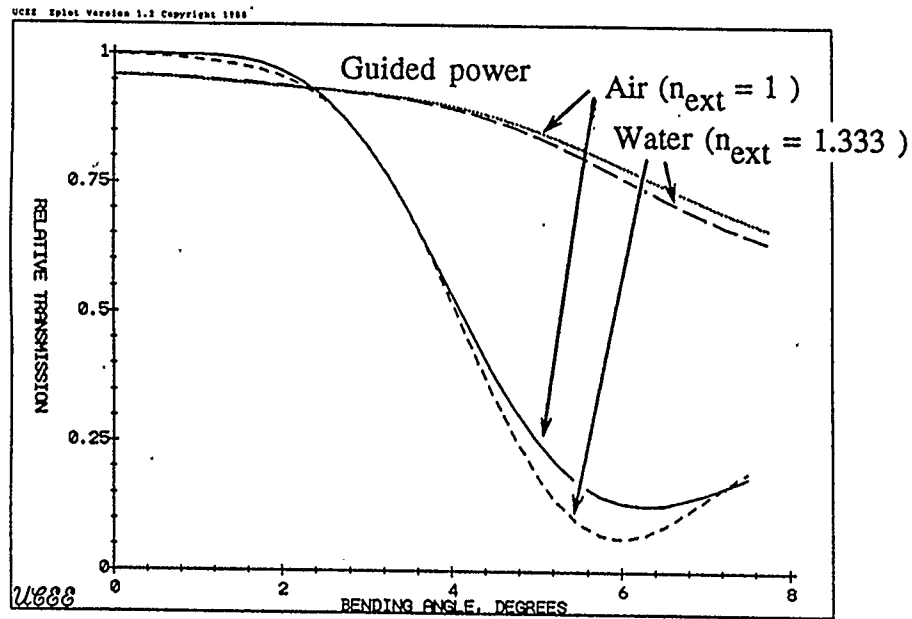


Fig. 7.11. Simulated transmission versus bending characteristics for the fiber taper of Fig. 7.4

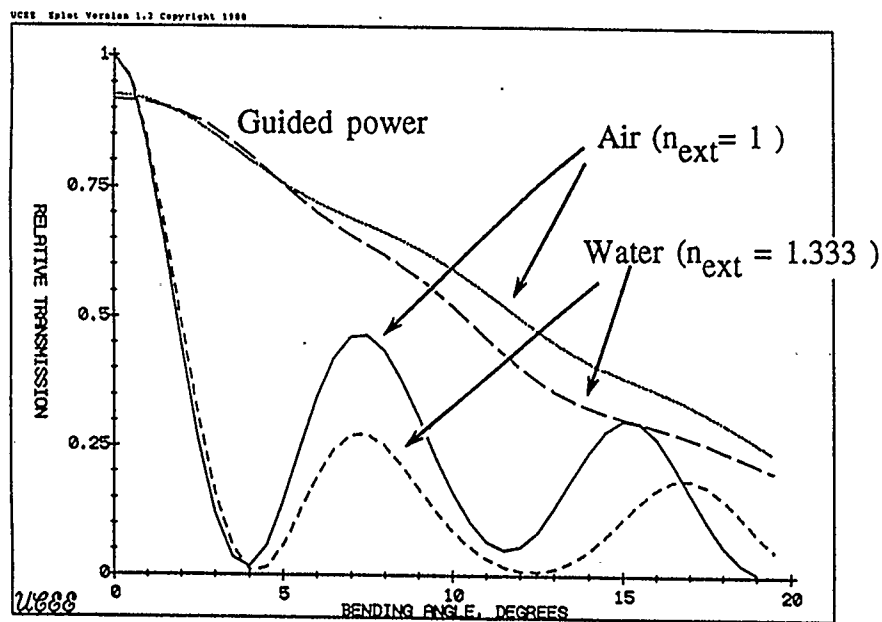


Fig. 7.12. Simulated transmission versus bending characteristics for the fiber taper of Fig. 7.5

7.3. Fiber-taper vortex shedding flowmeters

In order to use a fiber taper to sense the shedding frequency in a vortex shedding arrangement, the fiber taper could be mounted across the flow, so that fluid forces induce oscillation of the taper, causing slight bending, which can be sensed by light travelling through the fiber. The fiber taper could be used as the shedding strut or as a sensing secondary strut located downstream of the primary shedding strut. Both configurations were investigated in this work [75] and results are detailed herein. After conducting our preliminary experiments we recognized the importance of calibrating our flow rig so as to be able to compare the frequencies detected to the theoretically expected values of vortex shedding. This is to be described first in this section. Details of implementation of the vortex shedding flow meter arrangements then follow and discussion of the obtained results, with the arrangement having the fiber itself as a shedding strut discussed first, in order to explain the need for a rigid strut in the vortex shedding meter.

7.3.1. Rig calibration

Calibration of the flow rig was carried out using a weigh tank with piezoelectric S-type load cell, a Western scale DF-1000 indicator and an HP 7132A strip chart recorder. A two inch water line was connected to the rig tank and the connection of the test section back to the rig tank replaced by a two inch hose to the weigh tank. The rig was operated at different flow rates as indicated by the rotameter within its range. Outside of the rotameter range the needle value at the rotameter inlet was kept fully open and the flow controlled by the needle valve at the outlet of

the test section alone, with the pressure reading of the manometer at the outlet of the rotameter taken as indication of the flow. Flow rates within the range of the rotameter using the inlet valve for controlling the flow were also calibrated. The connection to the mains water line supplied water continuously into the rig tank so as to make it possible to run each calibration for a reasonable time and get long enough traces. The traces indicate the weight of water discharged into the calibration tank versus time, enabling direct calculation of the flow rate in kilogram weight per minute. Fig 7.13 gives the result of calibration. Actual flow rates were then converted to volume per unit time to compute the corresponding average flow velocities in meters per second. As will be described shortly the experiments gave frequency peaks scattered around those of a strut with a $125\ \mu\text{m}$ diameter, which is that of the bare fiber. We also used a rigid strut of $750\ \mu\text{m}$ for comparison. Strouhal frequencies for those two values of strut diameter at various flow velocities were calculated using equations (6.4) and (6.5) to provide a reference for our measurements. Fig. 7.14 gives such reference curves and the kink indicates where the flow crosses the border of laminar vortex shedding into the transition region where equation (6.5) is used.

Bare fiber tapers were installed into the test section of the rig in two opposite $300\ \mu\text{m}$ holes spanning a diameter of the flow pipe and glued in with super glue. Since none of the fiber tapers characterized in the previous section survived the handling and characterization, new fiber tapers were installed directly after dimensional measurement. The resulting modulation frequencies of taper transmission with flow were investigated using the HP 5423A Structural Dynamics

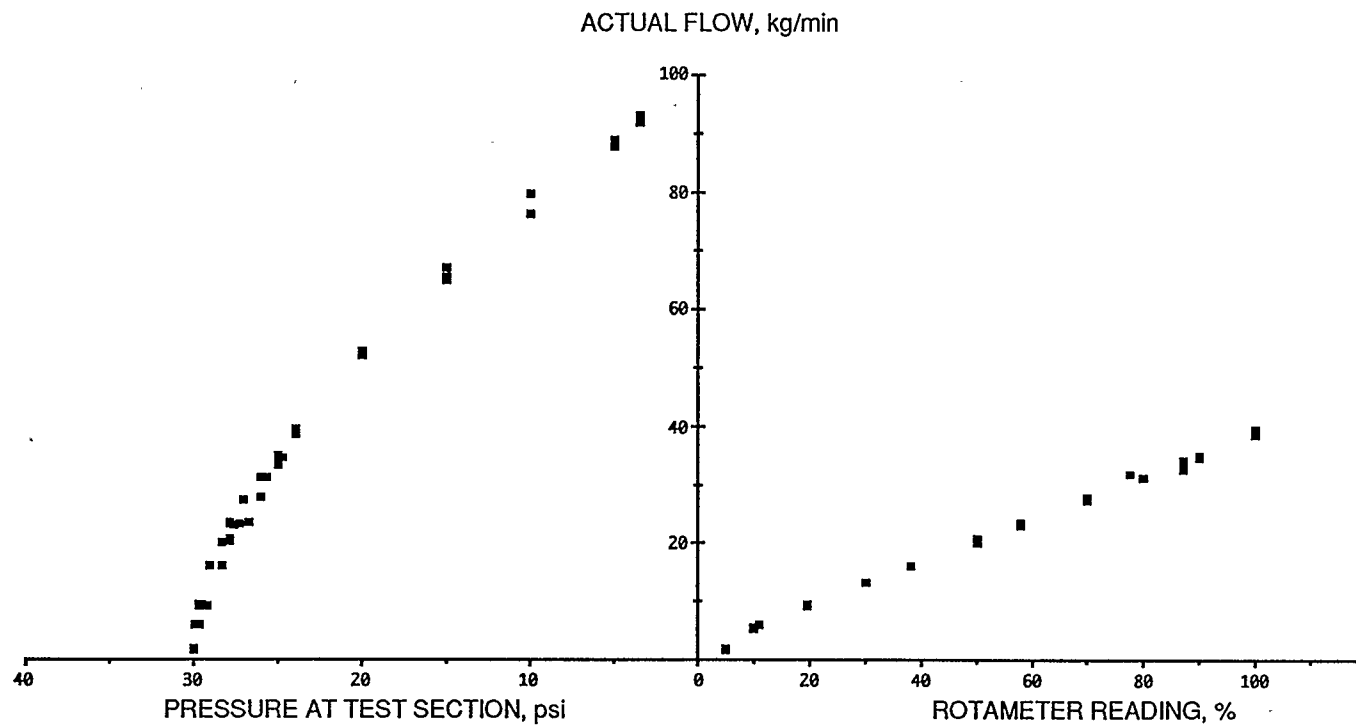


Fig. 7.13. Rig calibration chart

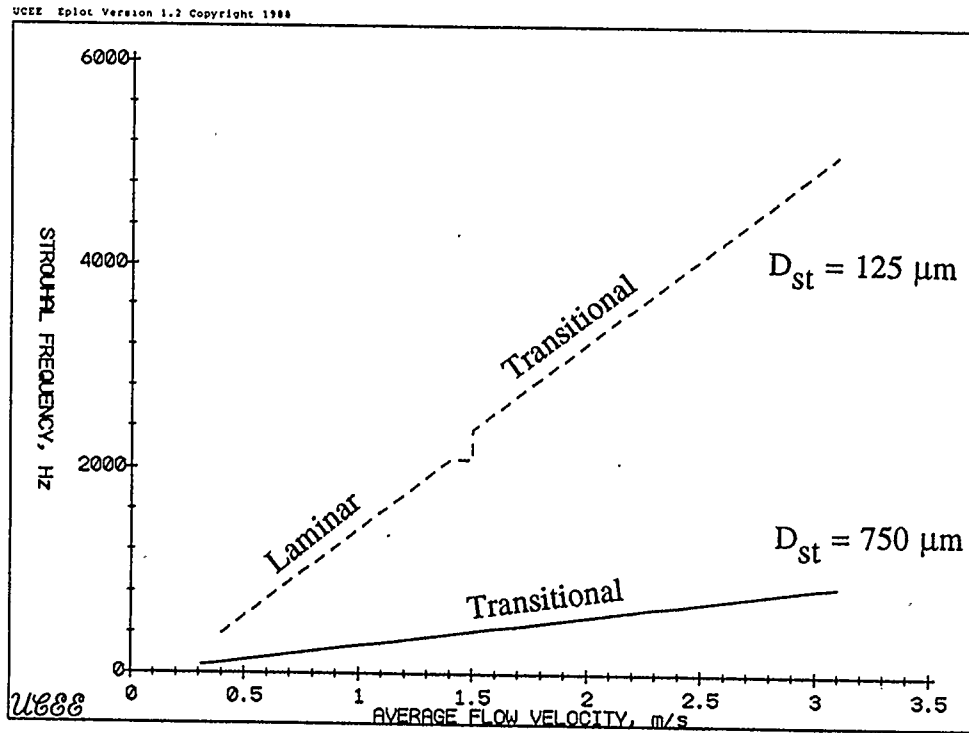


Fig. 7.14. Reference curves; shedding frequencies as obtained by Roshko's formulae (6.4) in the laminar range, and (6.5) in the transitional range of vortex shedding

Analyser for spectral analysis in an arrangement similar to that described previously in Ch. 5, using a He-Ne laser at 633 nm and a semiconductor diode laser at 1300 nm.

7.3.2. The fiber taper as a shedding strut

For minimum flow blockage the fiber taper was used as the shedding strut. The first taper used had dimensions of 25.4 μm waist diameter, 5.2 mm and 6.03 mm to the ends of the taper. The taper waist was not precisely centered inside the pipe it being placed at approximately 1.5 cm from one side and 1 cm from the other of the pipe walls. Two sets of measurements were conducted at 633 nm using the Optikon waveform analyser and at 1300 nm using the analog output of an Ando AQ-2101 power meter as detector and amplifier. These were powered from the mains and the waveform analyser gain set to 100 mV/ μW . Fig. 7.15 gives the display parameters and output traces for the 633 nm experiment. The check signs on the traces indicate the frequency nearest to the Strouhal frequency for the corresponding flow rate. Average flow velocities were computed based on rotameter or manometer indication and using the calibration chart of Fig. 7.13. The occurrence of broad spectral maxima with multiple discrete peaks indicates that the oscillations detected by the fiber taper do not correspond to a simple two dimensional vortex shedding process. Instead the variation of taper diameter, localized flow velocity and the complexity of how individual cell forces couple into the bending vibration of the taper resulted in the obtained spectra [52]. Frequency peaks corresponding to harmonics and mixing of the shedding frequencies are also observed in the traces. This could be the result of having one or more minima of the taper transmission lying within the bending

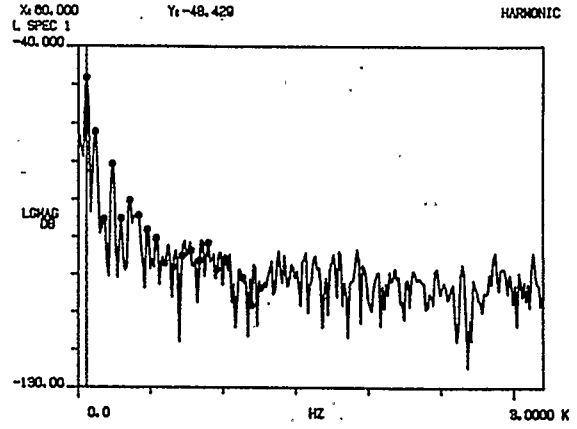
MEASUREMENT STATE

MEASUREMENT :	LINEAR SPECTRUM			
AVERAGE :	1	. STABLE		
SIGNAL :	RANDOM			
TRIGGER :	FREE RUN	. CHNL 1		

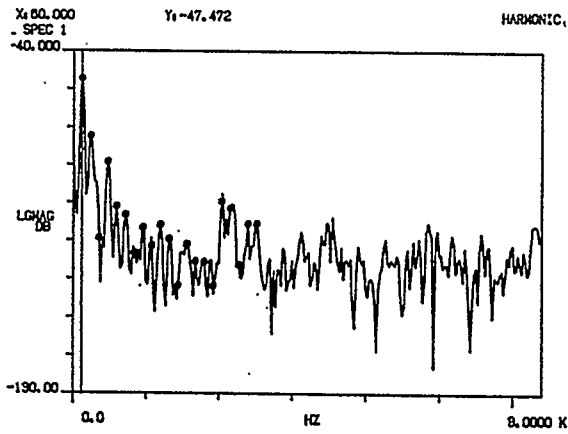
CENT FREQ :	0.0 HZ	ΔF :	12.5000 HZ
BANDWIDTH :	3.20000 KHZ		
TIME LENGTH :	80.0000 μS	ΔT :	78.1250 μS

CHAN #	RANGE	AC/DC	DELAY	CAL GCU/V
1	1 V	AC	0.0 S	1.00000
2	1 V	AC	0.0 S	1.00000

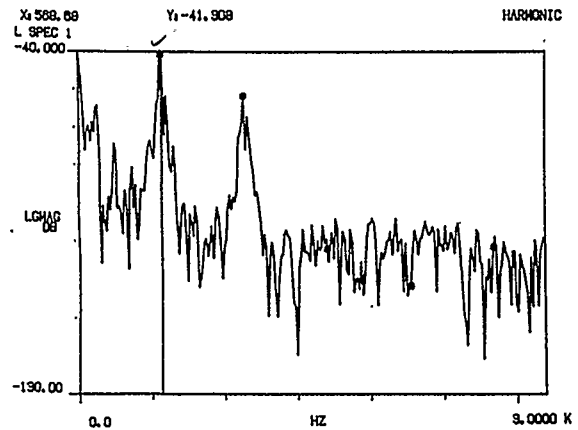
(a) Display parameters



(b) Freq. spectrum, Rig off

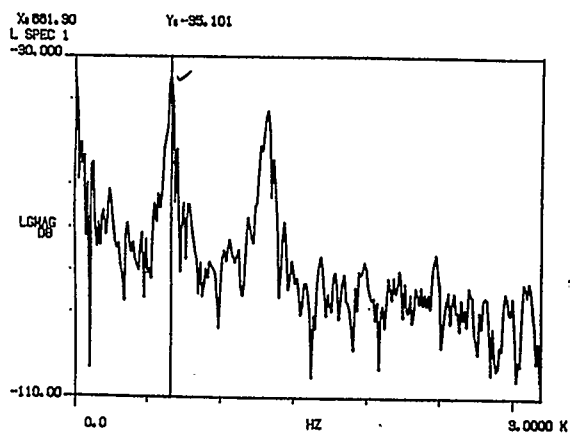
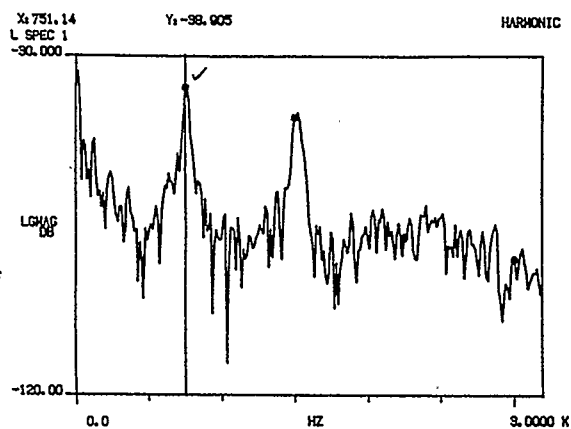
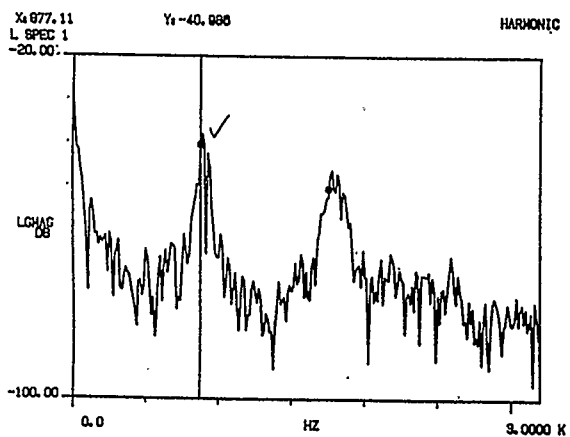
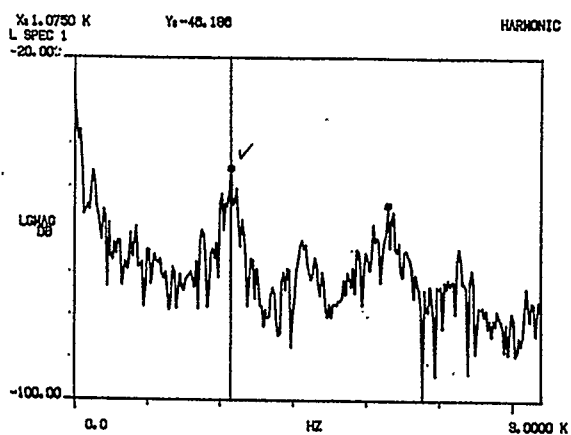


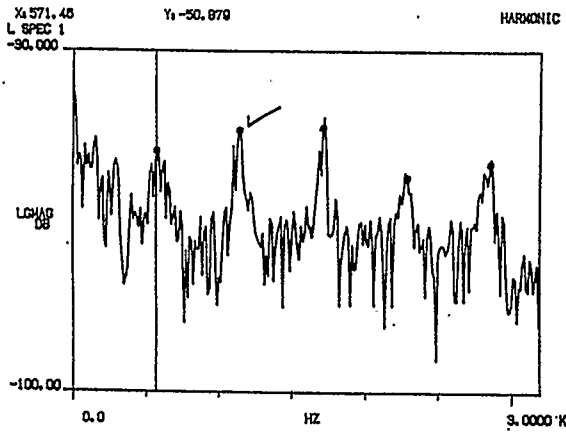
(c) Rig on, zero flow



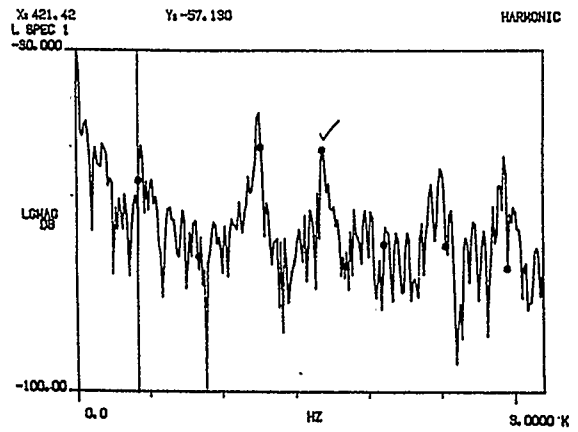
(d) $v = 0.39$ m/s

Fig. 7.15. Spectra of the intensity modulated signal with a fiber taper of 25.4 μ m waist as the shedding strut at 633 nm light wavelength

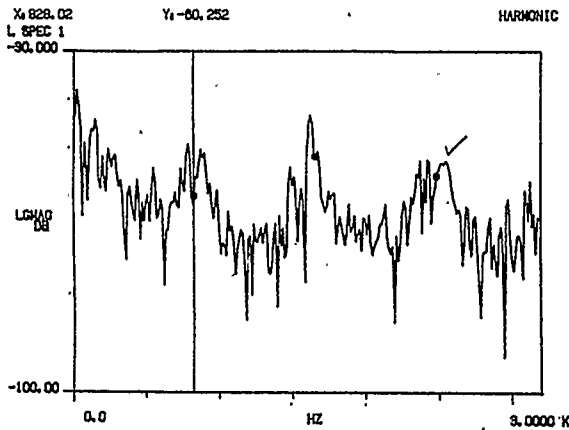
(e) $v = 0.526$ m/s(f) $v = 0.658$ m/s(g) $v = 0.766$ m/s(h) $v = 0.875$ m/s



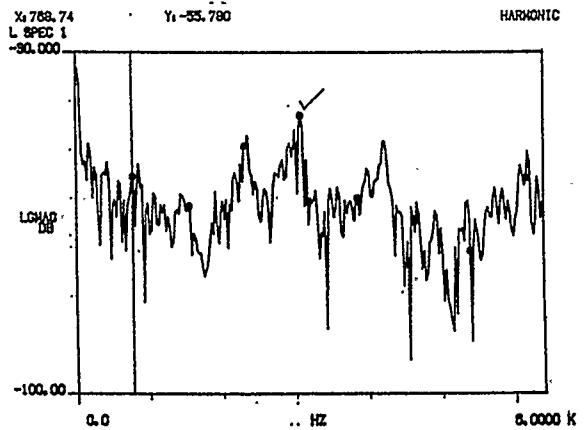
(i) $v = 0.987$ m/s



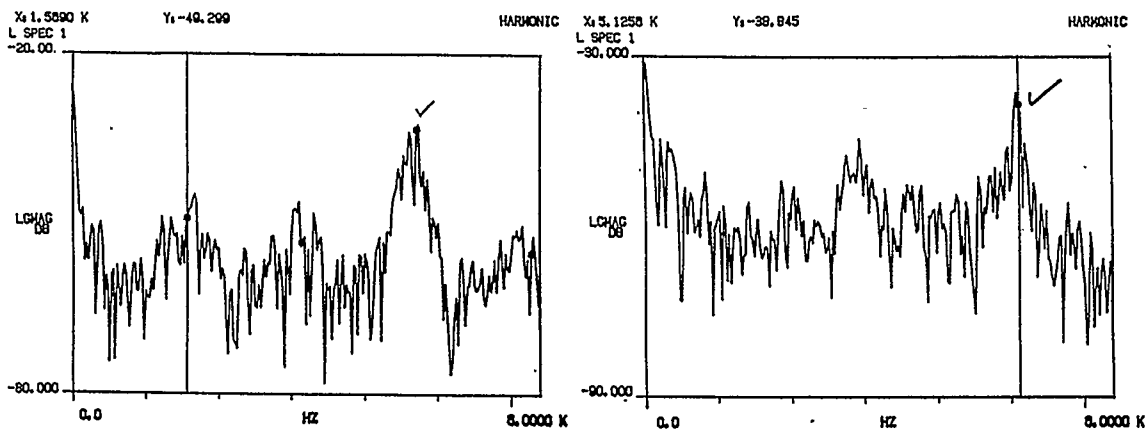
(j) $v = 1.118$ m/s



(k) $v = 1.77$ m/s



(l) $v = 2.23$ m/s



(m) $v = 2.626$ m/s

(n) $v = 3.008$ m/s

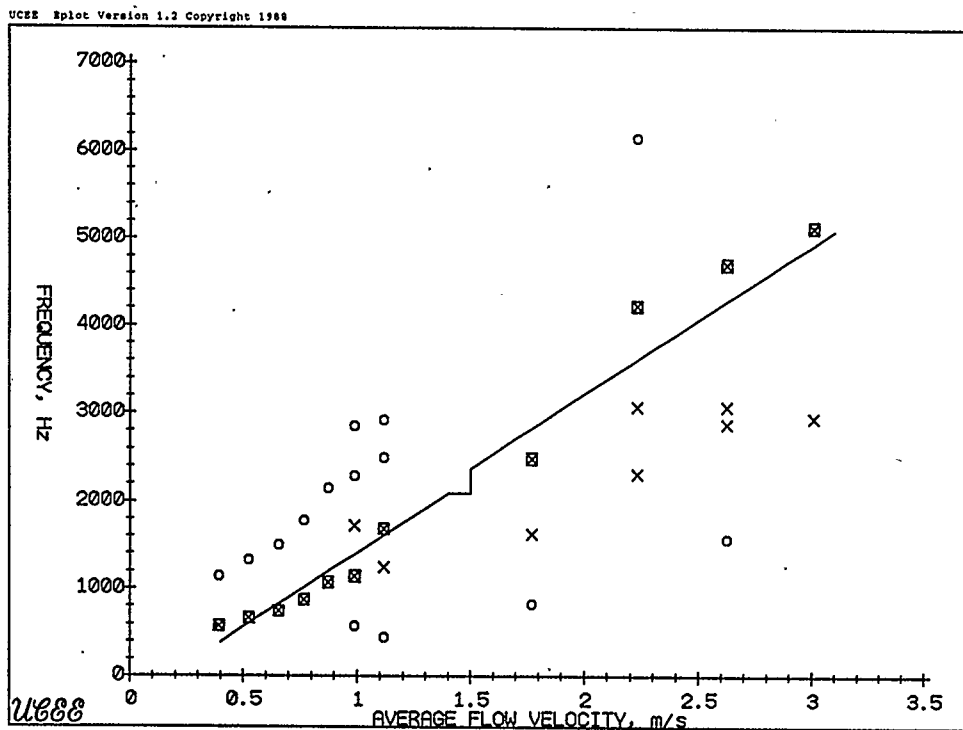
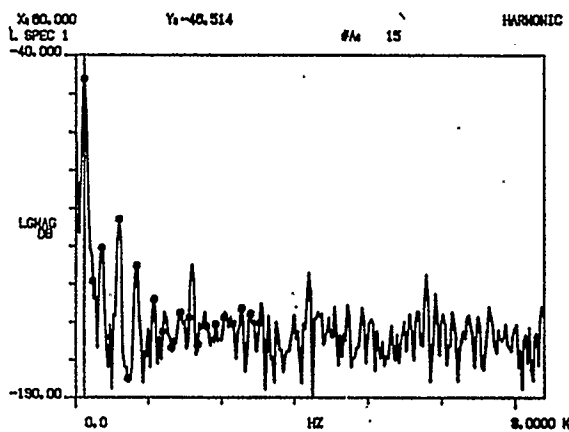


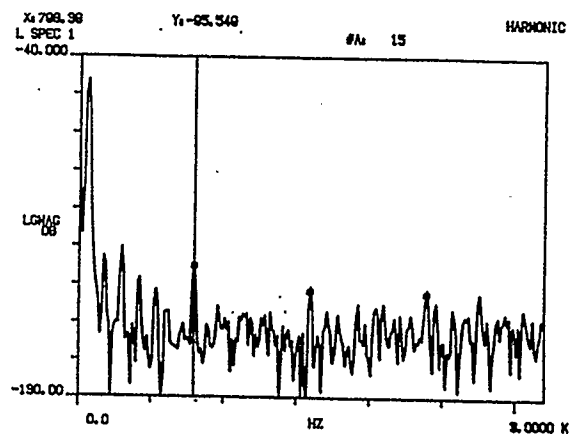
Fig. 7.16. Detected frequency peaks for Fig. 7.15 as compared to the shedding frequencies of a 125 μ m strut

oscillation amplitude as well as the highly non-linear characteristic of the taper at 633 nm. Fig. 7.16 displays the frequency peaks of all traces as compared to the Strouhal frequencies of vortex shedding past a rigid strut of 125 μm diameter. In the figure probable shedding frequencies are given as crosses, harmonics and mixing products as circles while square-crosses represent the checked frequencies on the frequency spectrum figures. Despite peak enhancement over background noise of about 25 dB in most traces the shedding frequency can not always be identified.

At 1300 nm where the fiber is single mode the traces and frequency peaks of Figs. 7.17 and 7.18 are obtained. As can be seen only the shedding frequencies were detected and almost only within the laminar range of vortex shedding. The disappearance of harmonics can be justified by the decreased non-linearity of the characteristics of the taper transmission at 1300 nm thus the transmission minima at larger bending values might be outside the bending vibration range. The disappearance of shedding frequency peaks outside of the laminar range except for one point at a high flow velocity is however difficult to understand. A hiatus in the shedding frequencies of a fiber strut near the end of laminar vortex shedding was previously observed by other investigators who used multimode interference to detect the shedding frequency. This was explained as being due to an antiresonance effect at these flow velocities [6]. Since the detection electronics used at 1300 nm were different from those we used at 633 nm with a frequency response that we were not able to characterize since no modulation of the laser output was available, the flow experiment was repeated at 633 nm with the Ando AQ-2101 power meter as detector and amplifier. The results are given in Figs. 7.19 and 7.20 and the shedding



(a) Rig off



(b) Rig on, zero flow

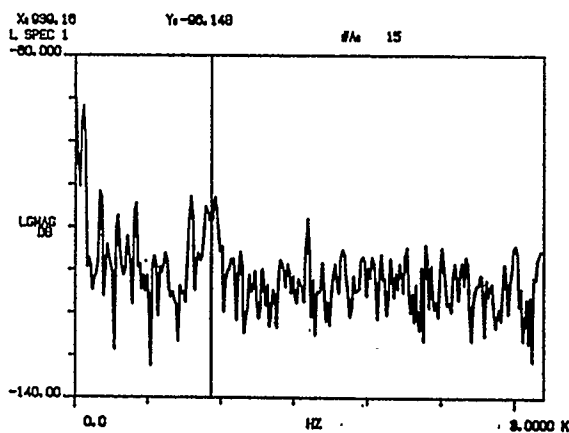
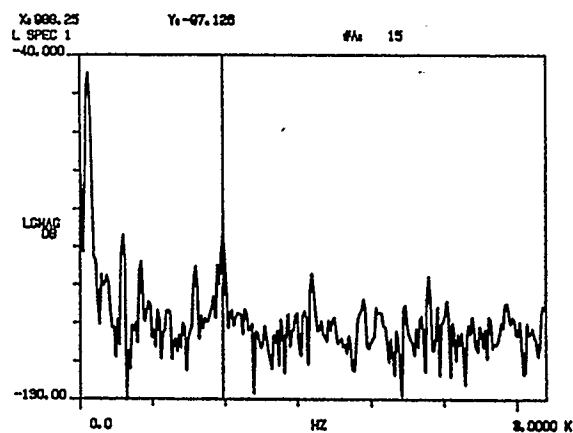
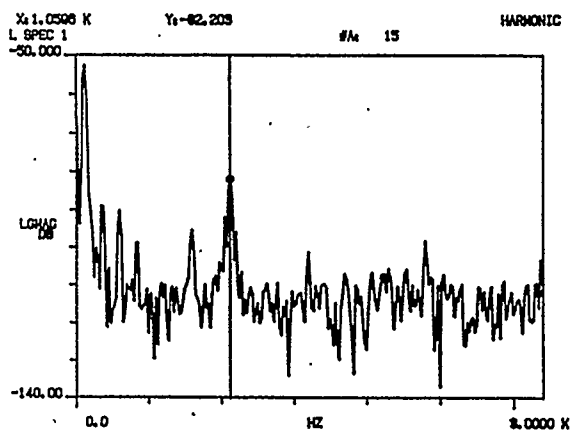
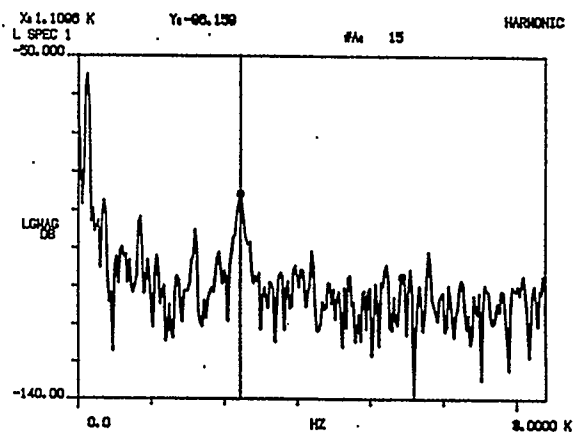
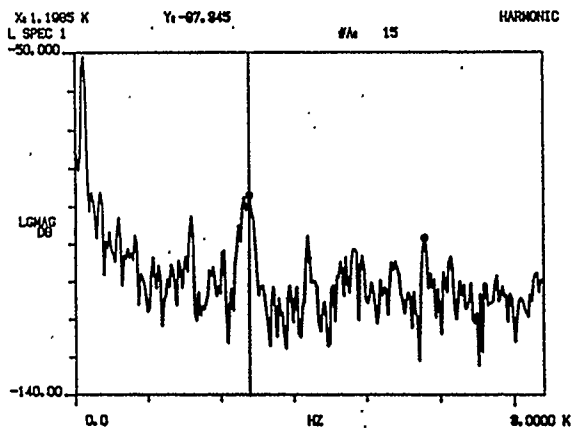
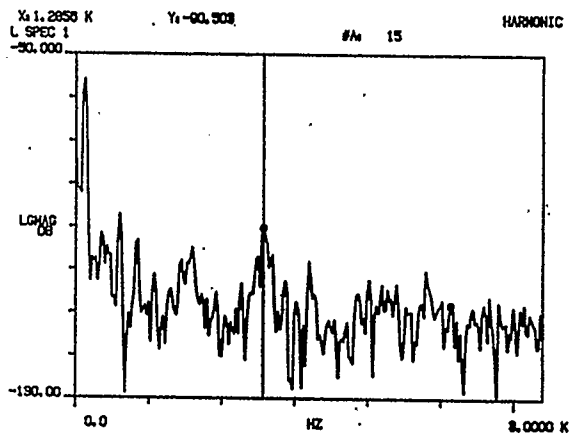
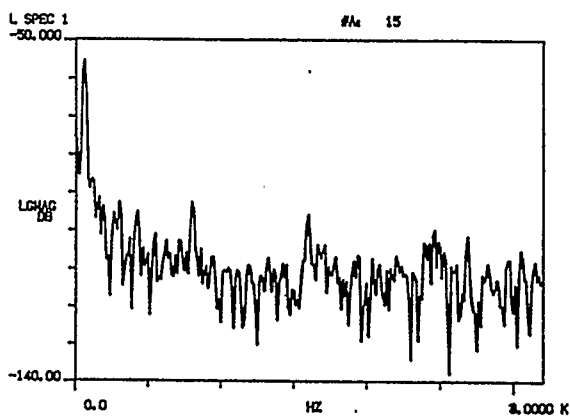
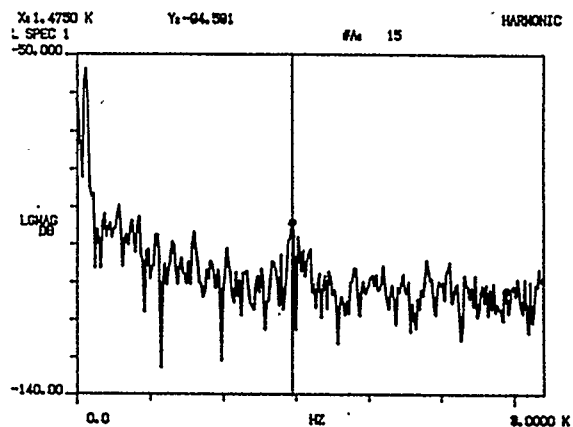
(c) $v = 0.617$ m/s(d) $v = 0.658$ m/s

Fig. 7.17. Spectra of the intensity modulated signal at 1300 nm light wavelength using the same taper as Fig. 7.15

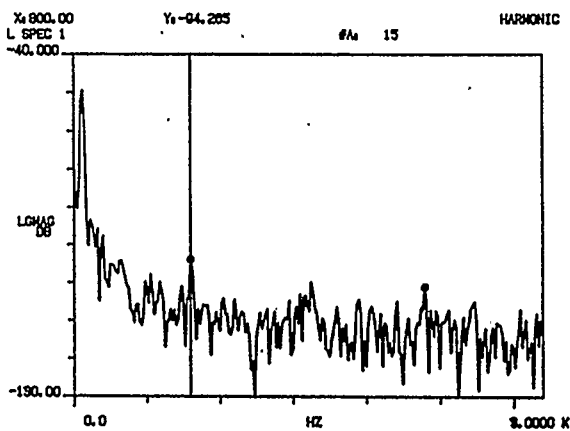
(e) $v = 0.766$ m/s(f) $v = 0.875$ m/s(g) $v = 0.987$ m/s(h) $v = 1.118$ m/s



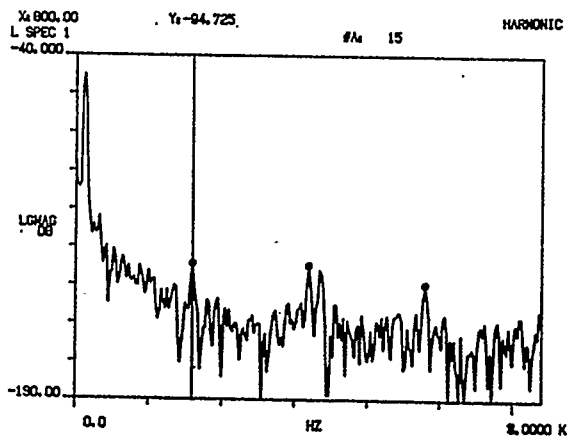
(i) $v = 1.77$ m/s



(j) $v = 2.23$ m/s



(k) $v = 2.626$ m/s



(l) $v = 3.008$ m/s

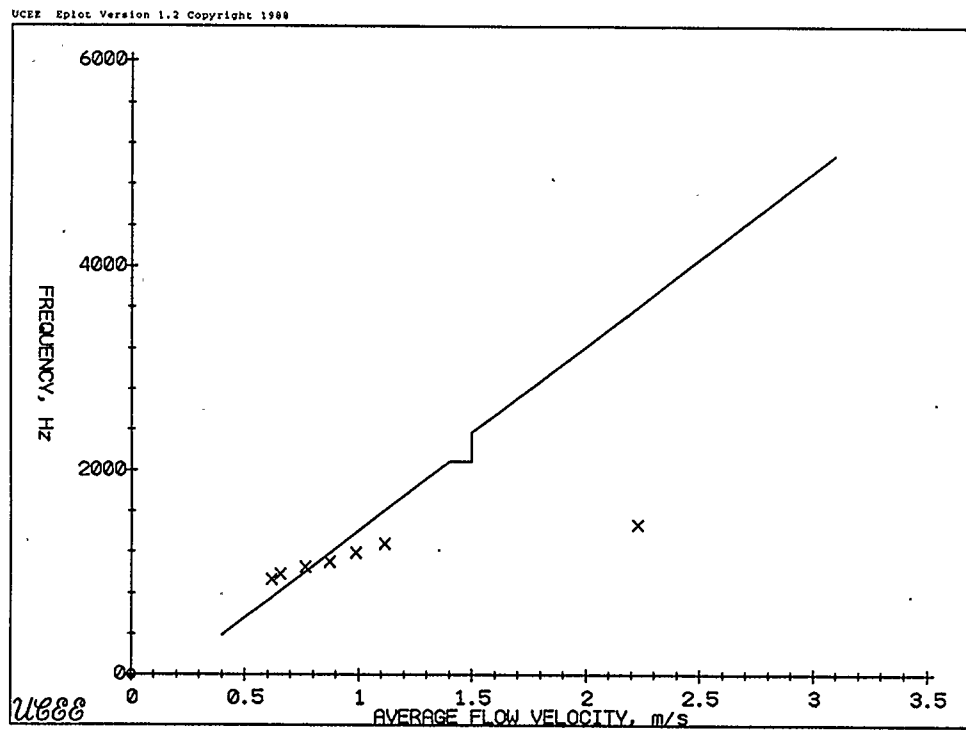
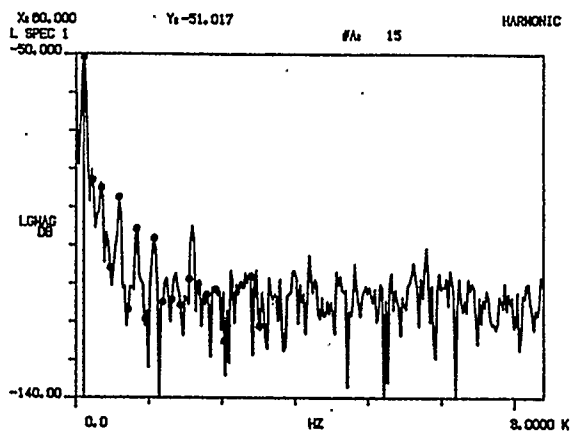


Fig. 7.18. Detected frequency peaks for Fig. 7.17 as compared to the shedding frequencies of a 125 μm strut



(a) Rig on, zero flow

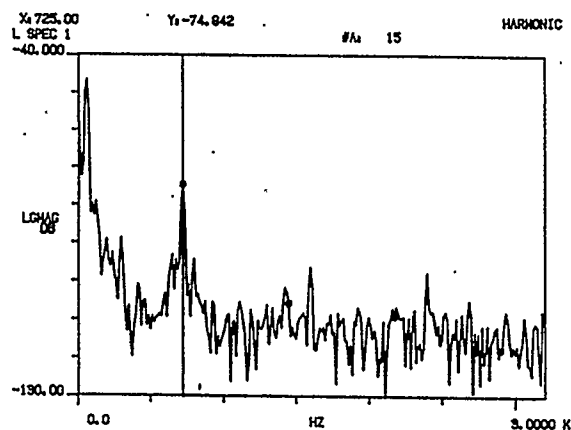
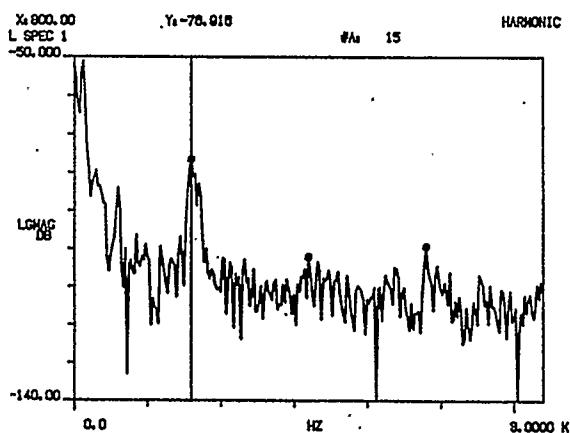
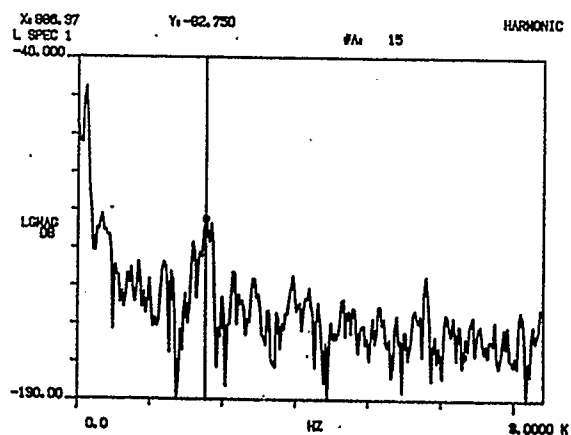
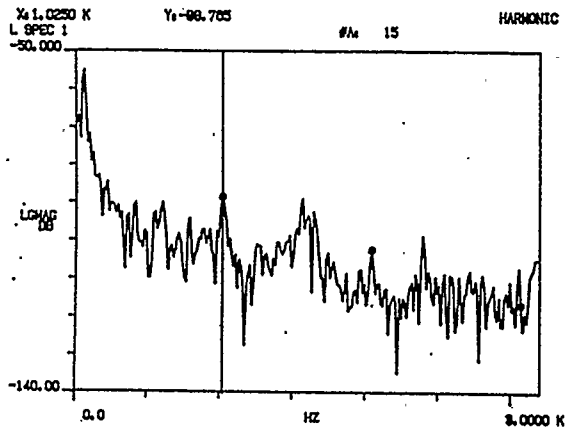
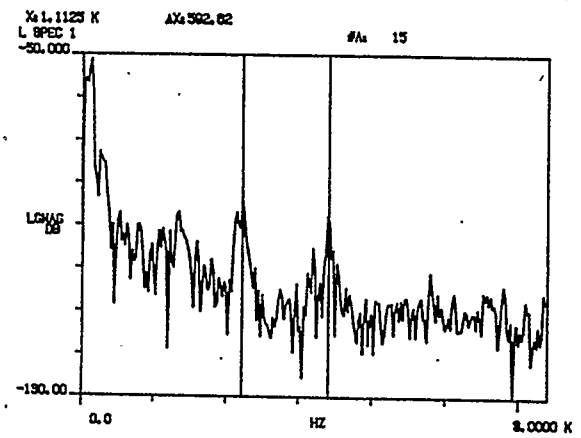
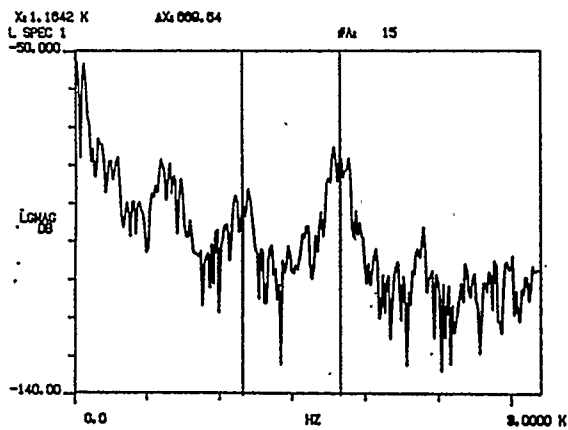
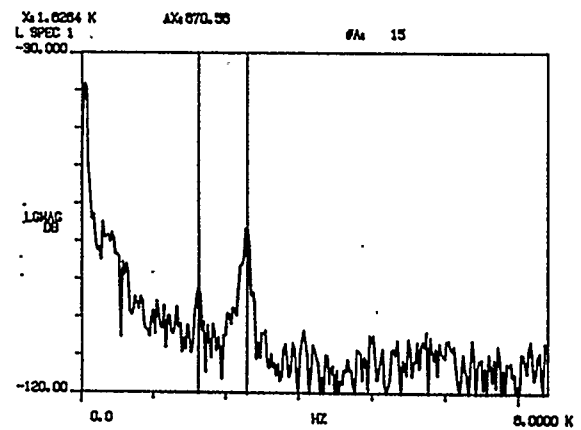
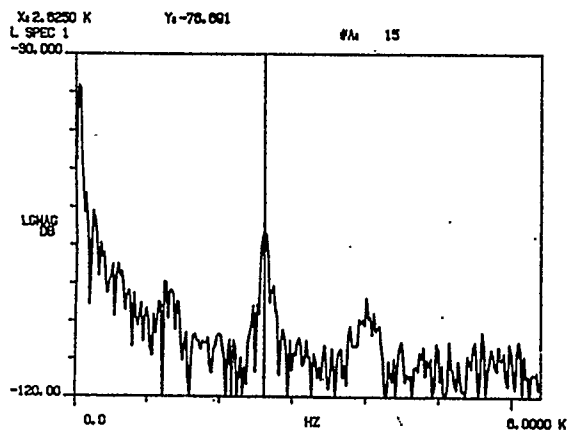
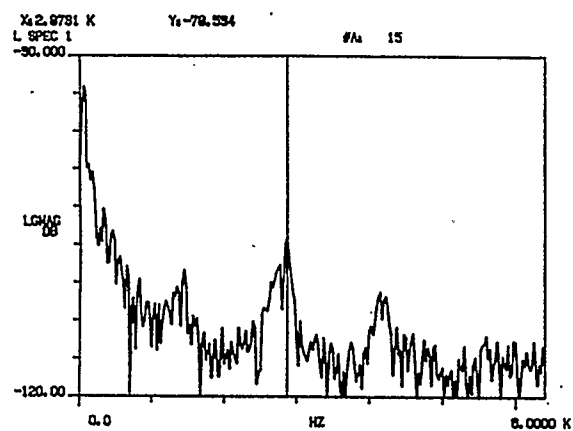
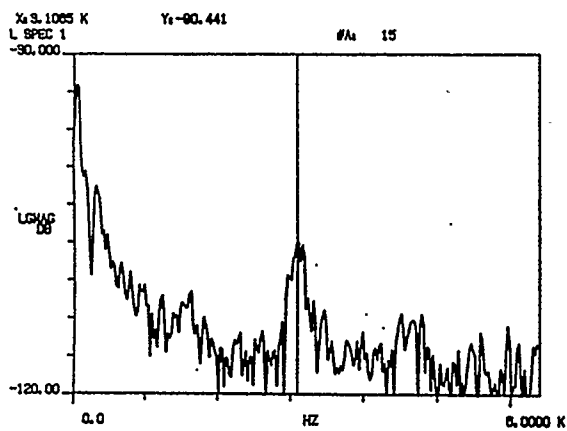
(b) $v = 0.526$ m/s(c) $v = 0.658$ m/s(d) $v = 0.766$ m/s

Fig. 7.19. Spectra of the intensity modulated signal with the same taper of Fig. 7.15 at 633 nm, with a different optical receiver

(e) $v = 0.875$ m/s(f) $v = 0.987$ m/s(g) $v = 1.118$ m/s(h) $v = 1.77$ m/s

(i) $v = 2.23$ m/s(j) $v = 2.626$ m/s(k) $v = 3.008$ m/s

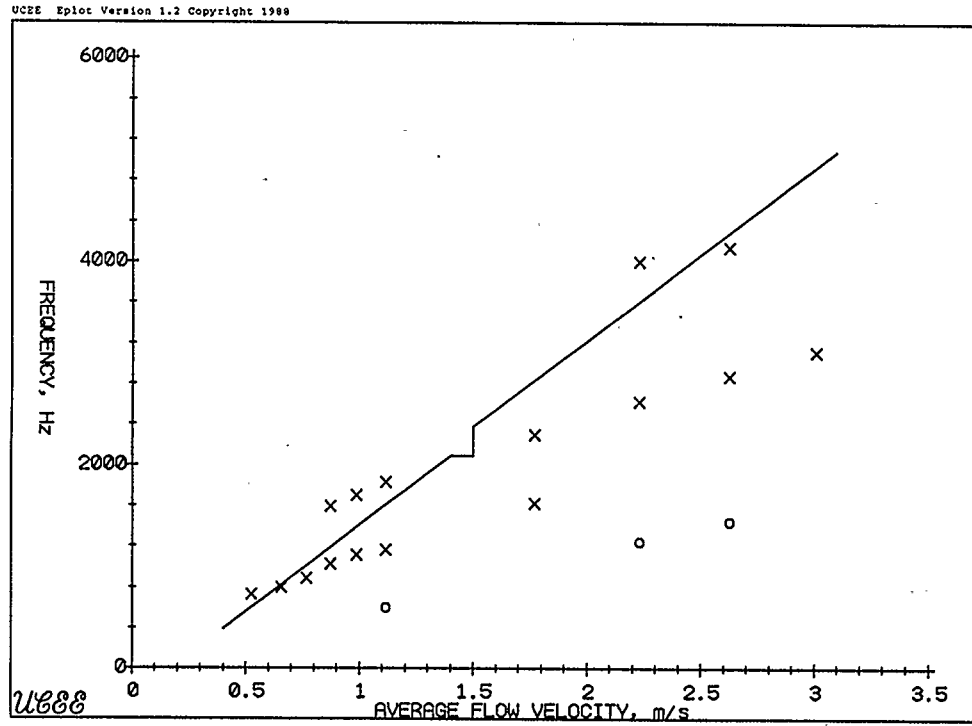


Fig. 7.20. Detected frequency peaks for Fig. 7. 19 as compared to the shedding frequencies of a 125 μm strut

frequencies appear clearly throughout the flow range. Due to the lower sensitivity of the Ando detector / amplifier as compared to the Optikon waveform analyser, shedding frequency peaks at flow velocities lower than 0.617 m/s were not detectable. This contributed as well to the occurrence of harmonics with smaller amplitudes. Comparing the results of all three experiments as for the reproducibility of the shedding frequency with the same taper at the same flow rate as indicated by the rotameter, a variation of 10 % of nominal frequency is typical and this can be attributed to two factors. As can be seen from the calibration graphs of Fig. 7.13 a variation of the actual flow rate at the same indication is typically 5% and can get up to 10% at lower flow rates. Better accuracies can not be attained so long as rotameter indication is used as a reference for the experiments. The second factor is that the development of the dominant cell of vortex shedding which corresponds to the dominant peak of a spectral maximum is somewhat arbitrary. This peak can correspond to any point of the inhomogeneous taper-flow system nearby to the taper waist and can give rise to the observed frequency variations from one run to another, particularly at higher flow velocities where the vortex shedding is in the transitional range. The second taper installed had dimensions of 40.13 μm waist diameter, 110 μm waist length, 5.72 mm and 8 mm to the ends of the taper. The detected peaks with this taper are displayed in Figs. 7.21 and 7.22 for 633 nm and 1300 nm respectively. They show similar trends as for the previous results with large differences due to different taper dimensions. This is justified since the fiber taper as a shedding strut interacts with the flow wake and both taper dimensions and mounting tension are parameters involved in the oscillations. After conducting the

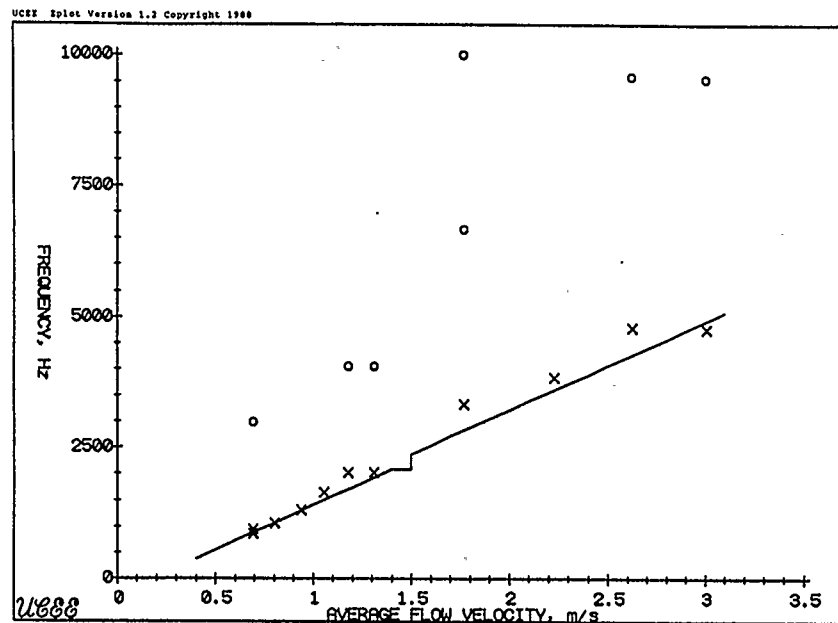


Fig. 7.21. Detected frequency peaks with a fiber taper of $40.13 \mu\text{m}$ waist as the shedding strut at 633 nm light wavelength

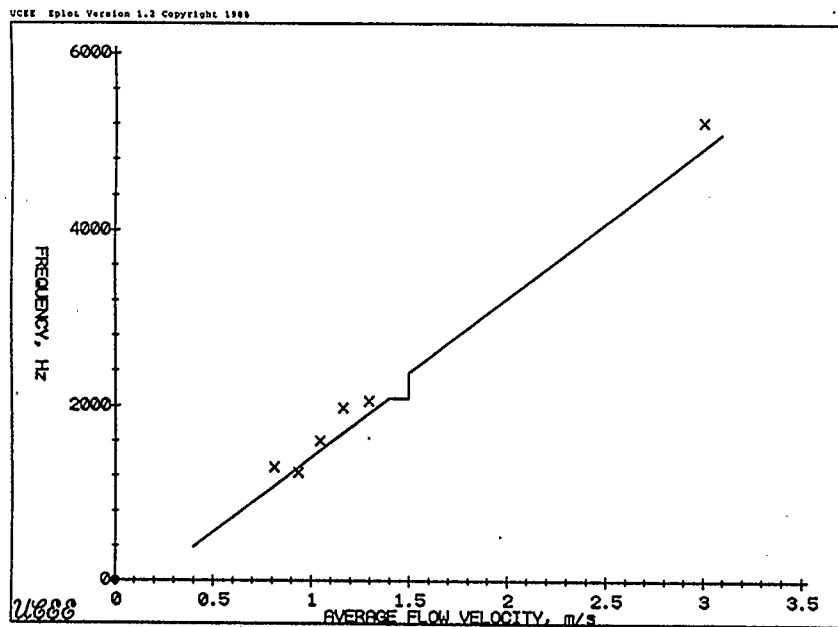


Fig. 7.22. Detected frequency peaks with a fiber taper of $40.13 \mu\text{m}$ waist as the shedding strut at 1300 nm light wavelength

experiments the plexiglass pipe section was dismantled and the fiber found to have caught some dirt that flowed inside the water tank. This was believed to have taken place after the experiments were completed but it indicates a limitation of this version of the flowmeter as it could not be used with dirty flow containing waister material such as textures. Teflon fibers remaining in the tank from the Teflon leak wraps used in rig calibration appeared to be the cause of the problem.

The experiments reported above indicate that having the fiber taper as the shedding strut can not provide for a reliable measurement of the flow since more than one shedding frequency can be detected at a single run and these vary in frequency from one run to another at the same flow rate. Good reasons for that are the inhomogeneity of the fiber taper and the arbitrary nature of vortex shedding cell formation. Harmonic frequencies are generated with bimodal fiber operation and add to the ambiguity of the measurement output. With single mode fiber operation harmonics are suppressed but the shedding frequencies are not detected outside of a small range of flow. The flexibility of the fiber results in shedding frequencies falling away from those predicted using the well-established theory of vortex shedding past a rigid cylinder. The distribution of experimentally obtained shedding frequencies around the theoretically expected values, particularly in the laminar vortex shedding range, suggests that the mechanical flexibility of the fiber taper has a significant effect on the ultimate oscillation frequency of the compound wake-fiber system [50]. With the involvement of the taper in wake oscillation variations in the shedding frequencies with taper dimensions are expected to be significant. Since taper dimensions are very hard to control this apparently rules out the practicality of this particular flowmeter

design. The applicability of fiber tapers to the measurement of shedding frequency is however supported since this is assured by the large enhancement in signal level at the frequency peak over the noise level which in some cases exceeded 30 dB.

7.3.3. The fiber taper as a secondary strut

Installing a separate rigid rod acting as a primary shedding strut in front of the taper would result in one shedding frequency except for the multiple peaking of the frequency maximum due to the flow velocity profile. Even in the transitional vortex shedding range all cells formed away from the pipe walls would have very near shedding frequencies [19]. The interaction of the fiber with the wake can be minimized by choosing a strut much larger in diameter than that of the fiber, yet small enough to keep end effects to a minimum. In this case the fiber acts only as a secondary detecting strut and shedding frequencies of the primary strut would dominate the detected frequency spectrum.

As discussed previously in chapter 6 a strut with a diameter of less than one thirtieth of the flow-pipe diameter would have a region free from end effects at its middle. This gives a value of 847 μm in our case and since smaller values will get nearer to the fiber diameter of 125 μm they are not preferred. The fiber taper waist is required to be as centered in the pipe as possible in order to detect the shedding frequency of the cell at the mid-point of the strut. Another design would be to use end effects to induce a single cell all over the strut. In this case the strut must be larger than 8.47 mm and would result in more flow blockage and deviation of the shedding frequencies from those of a two dimensional vortex shedding process. For

larger flow pipes the latter design would need to incorporate larger struts whereas the former can be applied as is. We thus selected to implement the former design and used a steel rod of diameter $0.0294 \text{ " } = 746.76 \text{ }\mu\text{m}$ as the primary strut since this was the nearest to $847 \text{ }\mu\text{m}$ from our selection of standard drill blanks. The fiber taper was mounted 4 strut diameters downstream of the primary strut. This is the nominal value used by authors who investigated vortex shedding past cylinders and spheres using other techniques [1,52,76,77].

With this arrangement, the results displayed in Figs. 7.23 and 7.24 were obtained at 633 nm, and those of Figs. 7.25 and 7.26 at 1300 nm. The taper used had dimensions of $23 \text{ }\mu\text{m}$ waist diameter, 0.98 mm waist length, and 9.15 mm and 4.7 mm to the ends of taper. The shedding frequencies of the primary strut were clearly detected and unambiguously identified at both wavelength. At 633 nm shedding frequencies corresponding to both the strut and the fiber were observed, as well as some harmonics and mixing products. At 1300 nm these were suppressed compared to the primary strut shedding frequencies. Since the fiber is now forced into vibration at a frequency far from its own Strouhal frequency, the vibration peaks are generally wider than those obtained when the fiber alone acted as the shedding strut and particularly when lock-in occurred and the fiber self-resonated with the wake vibration at around 1 or 3 kHz. The amplitude of forced vibration of the fiber past the strut is also expected to be smaller and smaller enhancement in the signal level over background noise is obtained. Nevertheless, the signal peaks are still about 15 dB or more over noise and with simple low pass filtering secondary shedding frequencies of the fiber can be eliminated. The frequency peaks for the primary strut follow closely

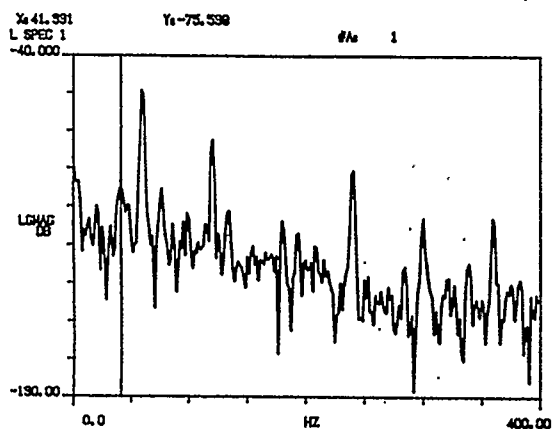
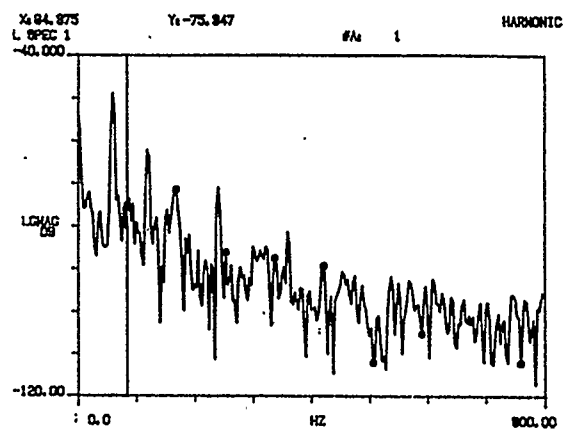
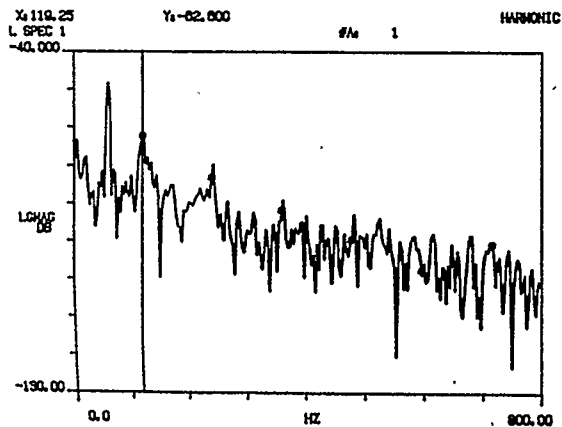
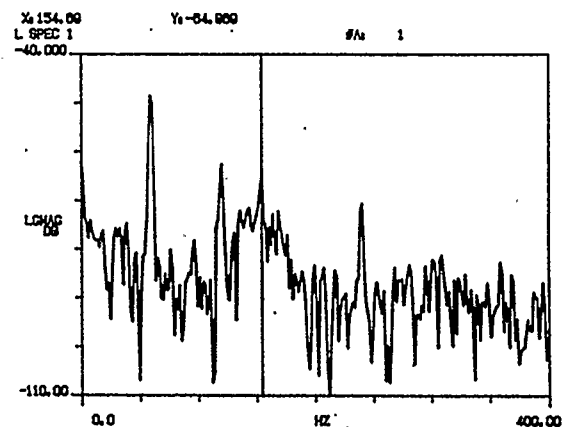
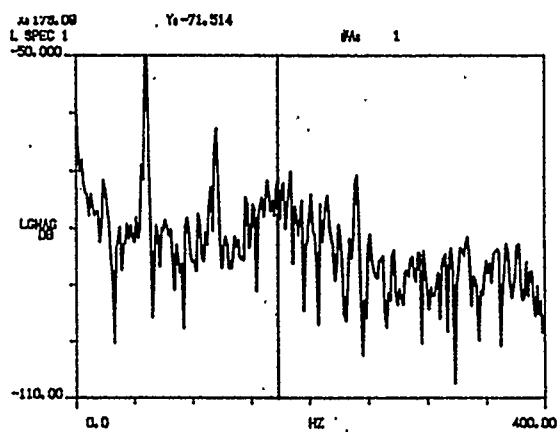
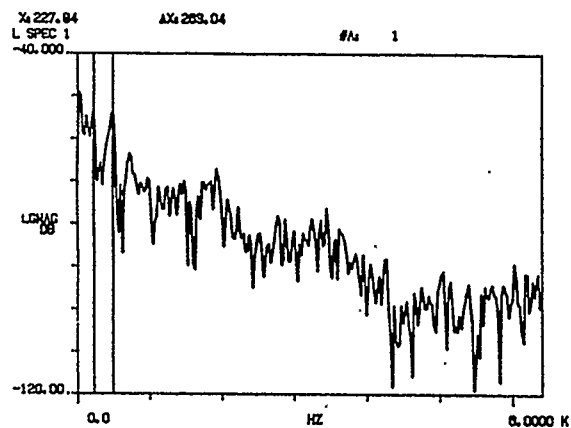
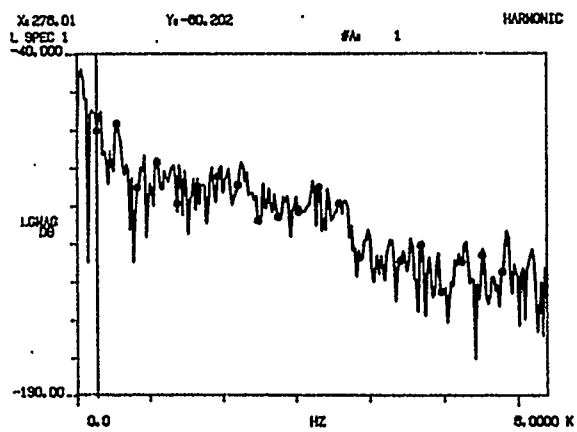
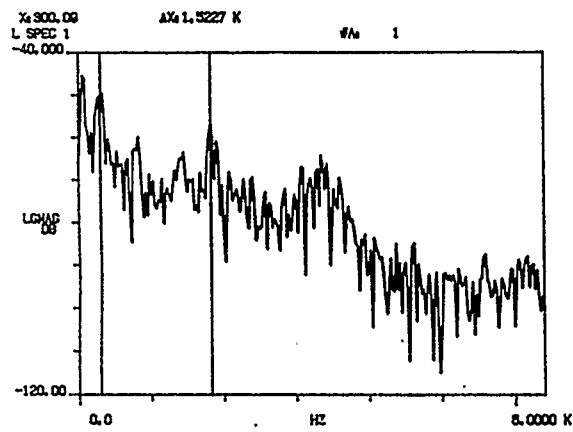
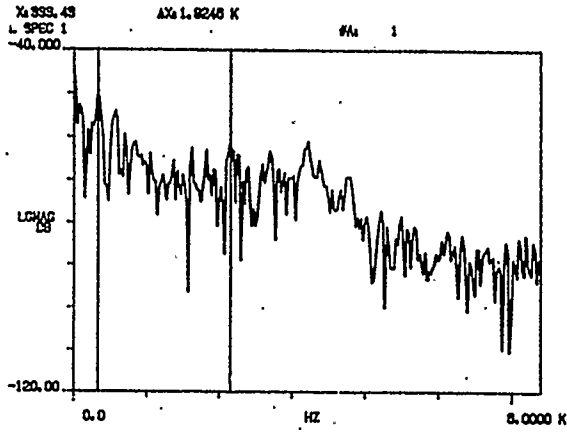
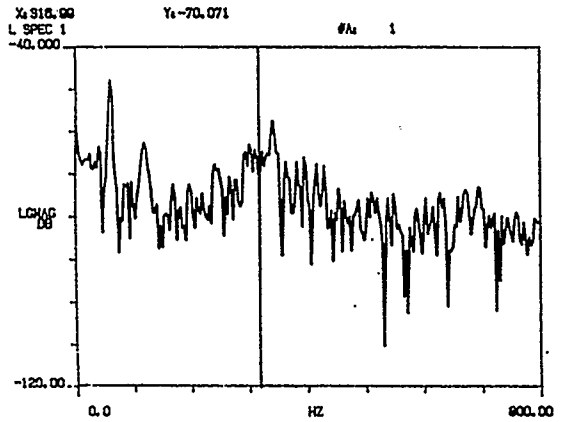
(a) $v = 0.191$ m/s(b) $v = 0.314$ m/s(c) $v = 0.438$ m/s(d) $v = 0.561$ m/s

Fig. 7.23. Spectra of the intensity modulated signal with a fiber taper of 23 μm waist as a secondary strut past a 750 μm primary strut, at 633 nm light wavelength

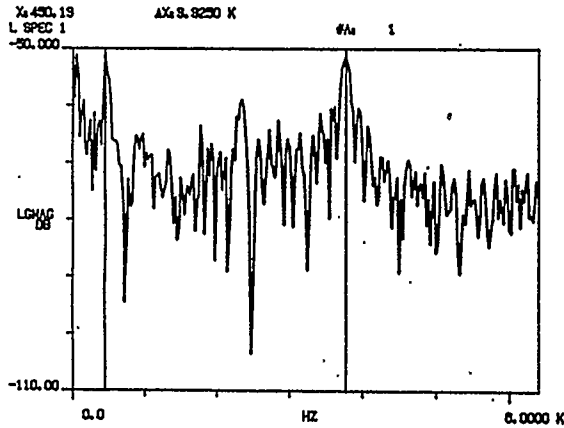
(e) $v = 0.696$ m/s(f) $v = 0.808$ m/s(g) $v = 0.943$ m/s(h) $v = 1.055$ m/s



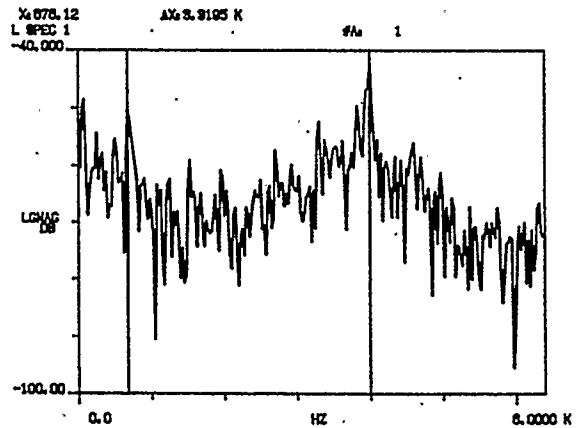
(i) $v = 1.179$ m/s



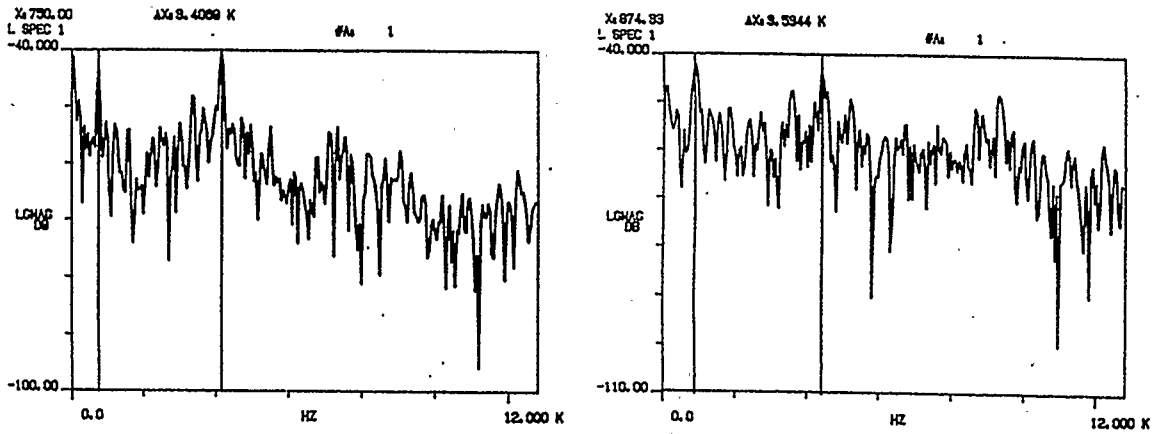
(j) $v = 1.313$ m/s



(k) $v = 1.77$ m/s



(l) $v = 2.23$ m/s



(m) $v = 2.626 \text{ m/s}$

(n) $v = 3.008 \text{ m/s}$

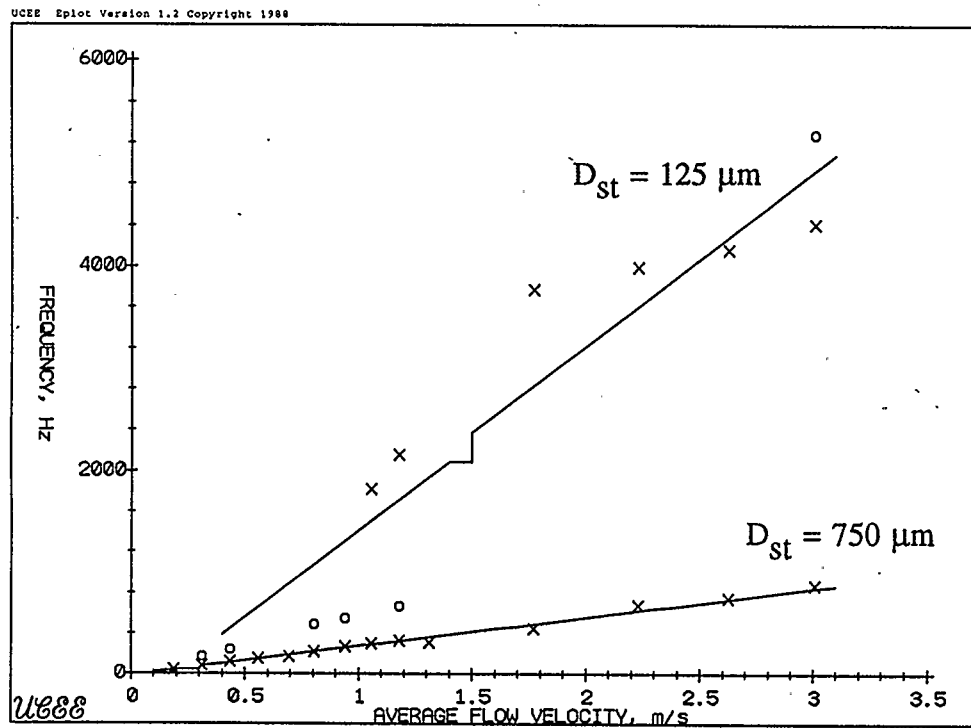


Fig. 7.24. Detected frequency peaks for Fig. 7.23 as compared to the shedding frequencies of 125 μm and 750 μm struts

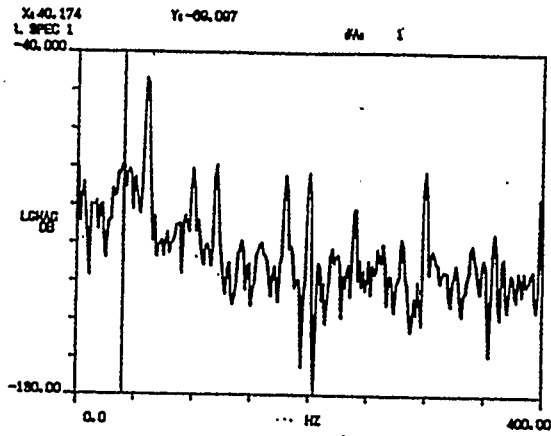
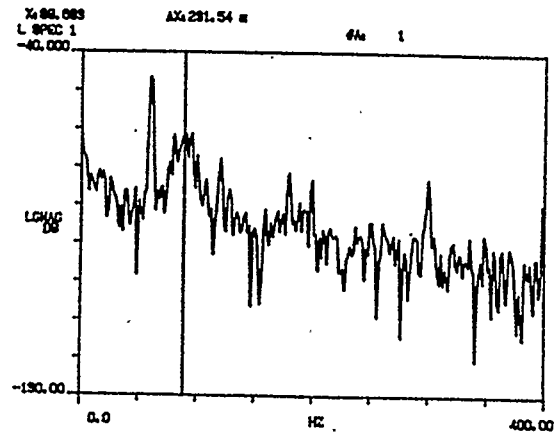
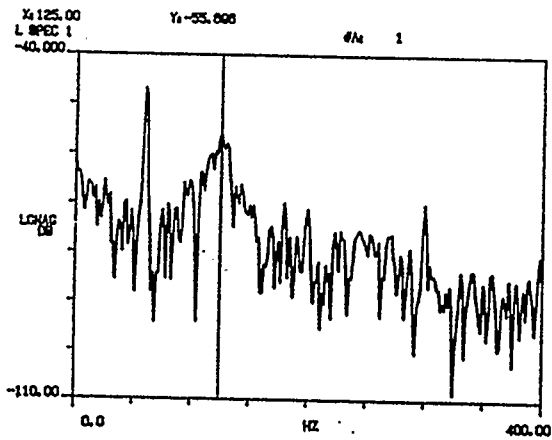
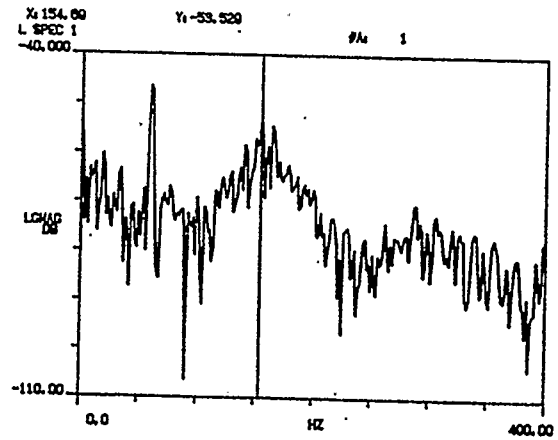
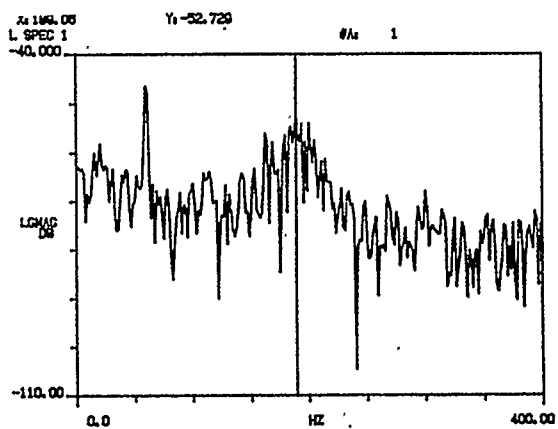
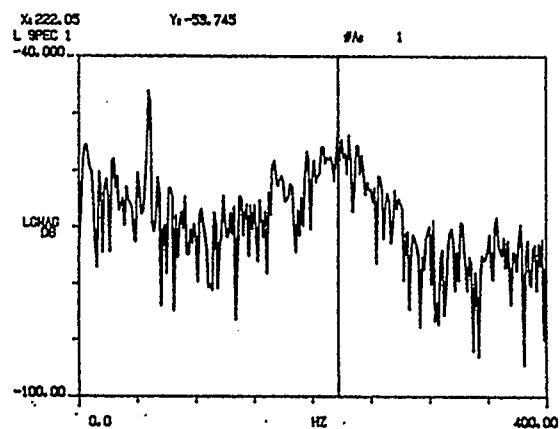
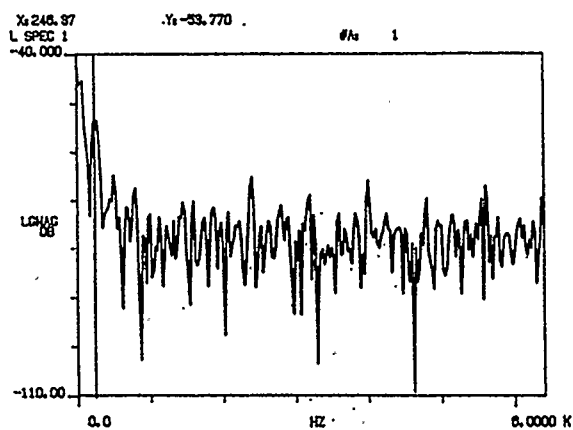
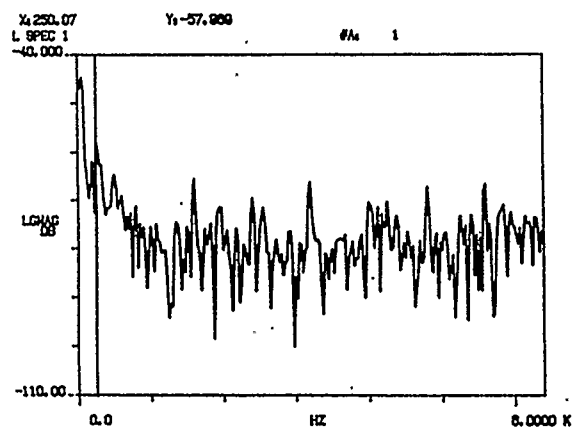
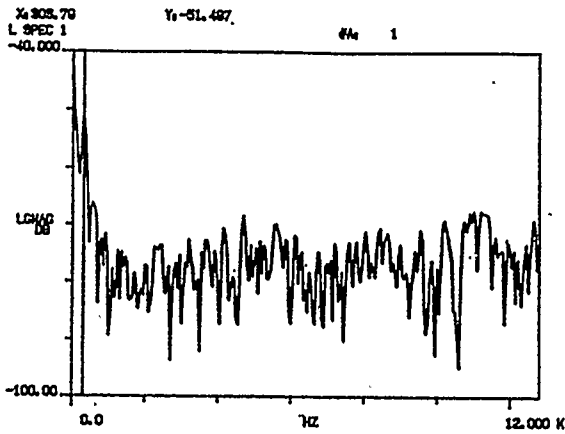
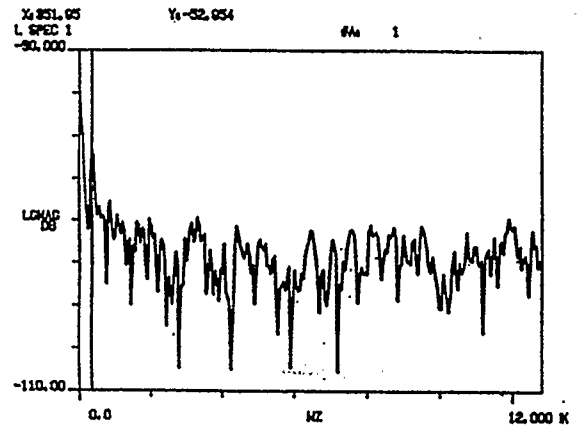
(a) $v = 0.191$ m/s(b) $v = 0.314$ m/s(c) $v = 0.438$ m/s(d) $v = 0.561$ m/s

Fig. 7.25. Spectra of the intensity modulated signal with the same taper of Fig. 7.23 as a secondary strut past a $750 \mu\text{m}$ primary strut, at 1300 nm light wavelength

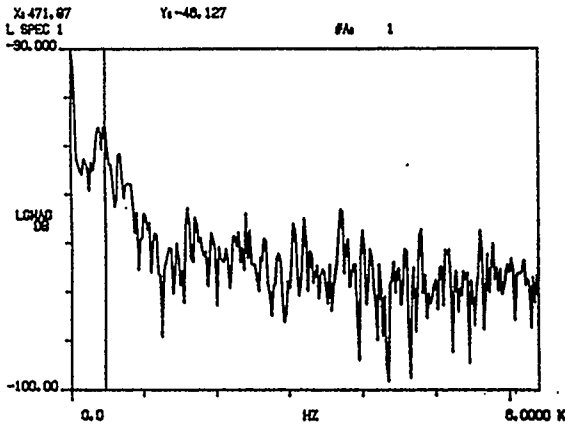
(e) $v = 0.696$ m/s(f) $v = 0.808$ m/s(g) $v = 0.943$ m/s(h) $v = 1.055$ m/s



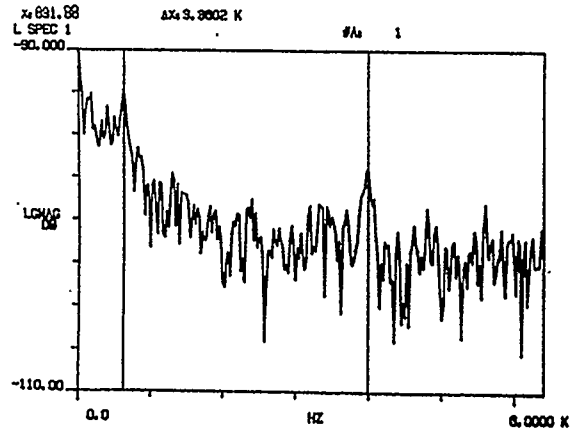
(i) $v = 1.179$ m/s



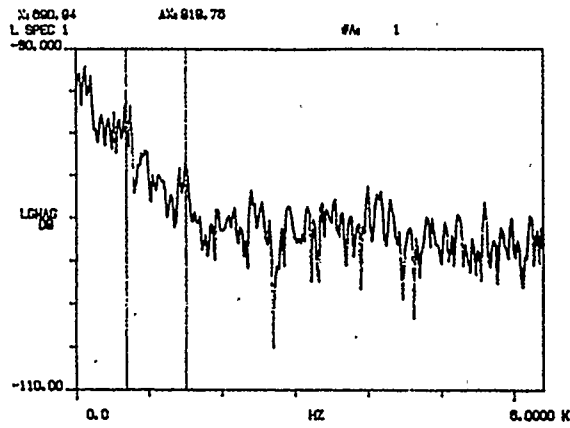
(j) $v = 1.313$ m/s



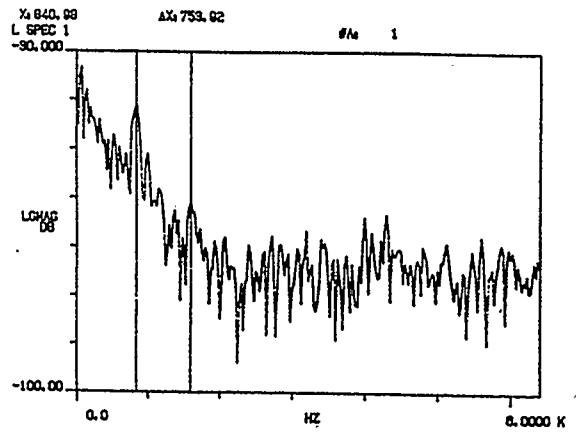
(k) $v = 1.77$ m/s



(l) $v = 2.23$ m/s



(m) $v = 2.626$ m/s



(n) $v = 3.008$ m/s

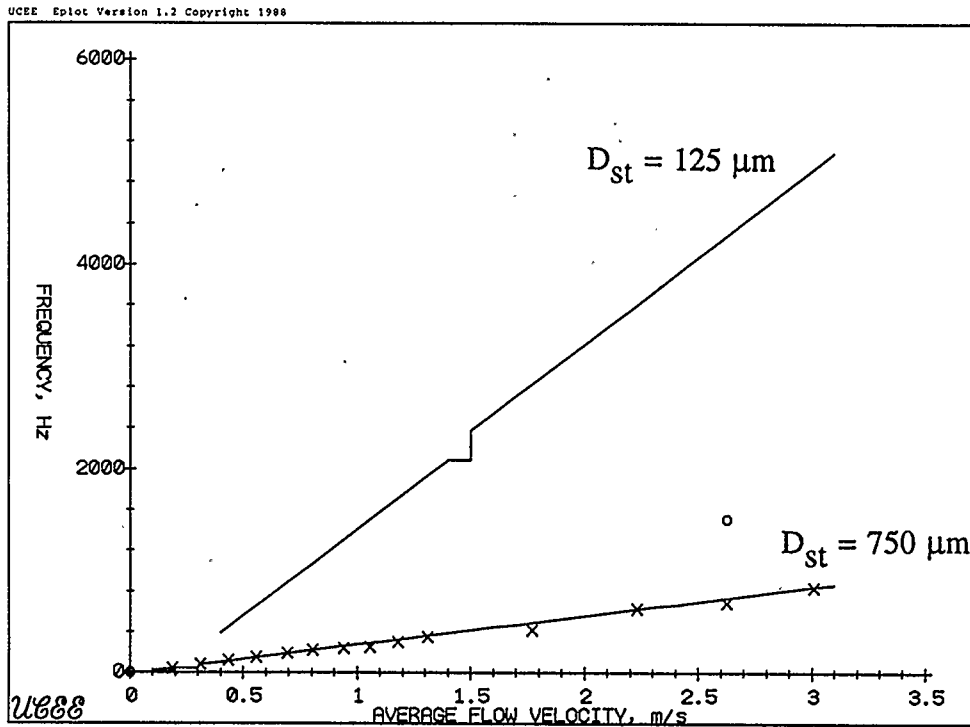


Fig. 7.26. Detected frequency peaks for Fig. 7.25 as compared to the shedding frequencies of 125 μm and 750 μm struts

those expected theoretically as can be seen from the figures. Using another fiber taper of 29 μm waist diameter, 3.48 mm waist length, 5.7 mm and 5 mm to the taper end resulted in the traces and frequency peaks shown in Figs. 7.27 - 7.30. The secondary shedding frequencies vary widely as a result of the different taper dimensions and the almost arbitrary mounting tensions. The generation of detectable harmonics and mixing products depends as well on the taper used. The primary shedding frequencies were however detectable with both tapers throughout the investigated range of flow at values close to those expected theoretically. Fig. 7.31 displays the experimentally detected primary shedding frequencies in all our experiments including two more experiments conducted with a fiber taper of 29.3 μm waist and 5.3 mm and 5.7 mm to the ends of taper. Fig. 7.32 displays peaks detected with the fiber tapers at 1300 nm. The enhanced linearity of taper transmission versus bending characteristics at this wavelength resulted in suppressed harmonics except at flow velocities near the upper end of the investigated range, giving rise to the frequency peak displayed as a circle at 2.626 m/s. The secondary shedding frequencies were also suppressed. The scattering of the experimental primary shedding peaks around values obtained by equation (6.5) is 5% for most of the flow range, which is the limited accuracy of the rotameter used to indicate flow rate as obtained by rig calibration.

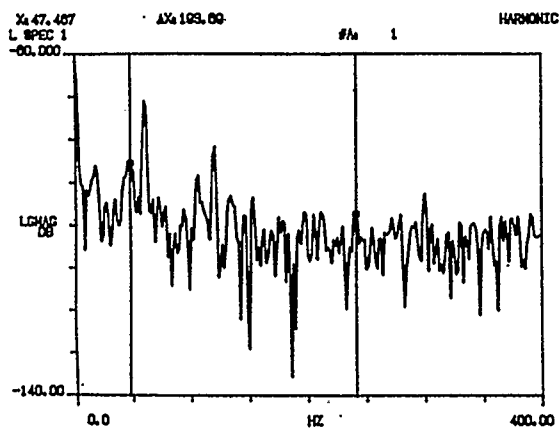
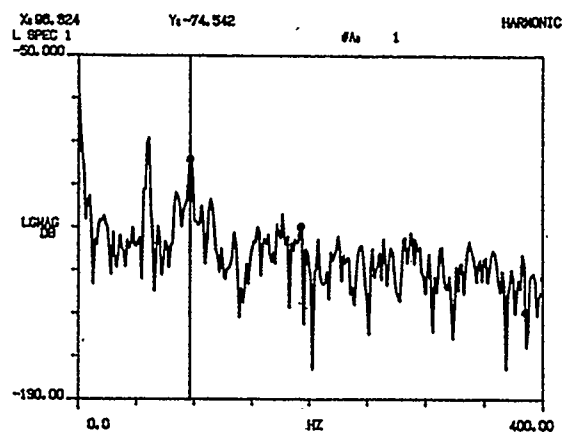
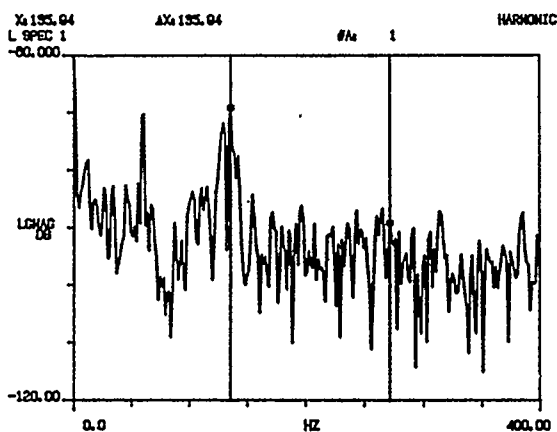
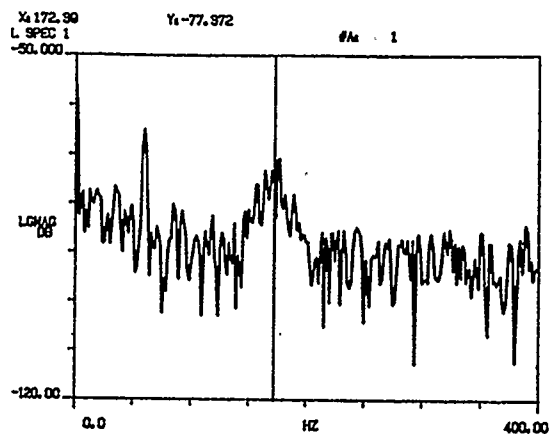
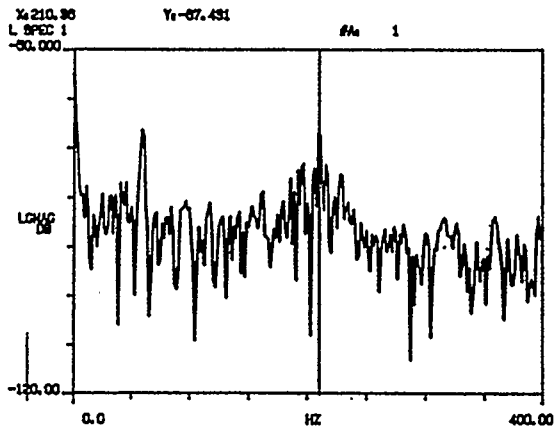
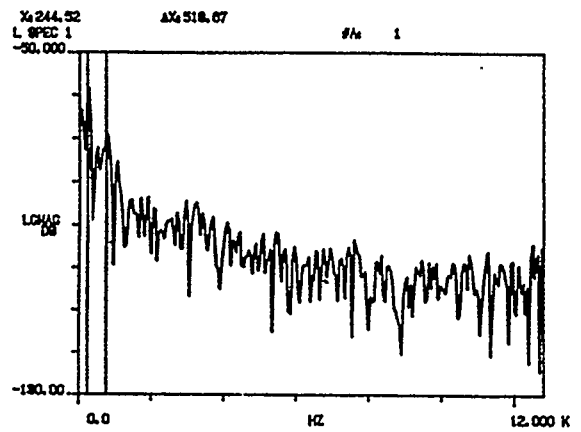
(a) $v = 0.191$ m/s(b) $v = 0.314$ m/s(c) $v = 0.438$ m/s(d) $v = 0.561$ m/s

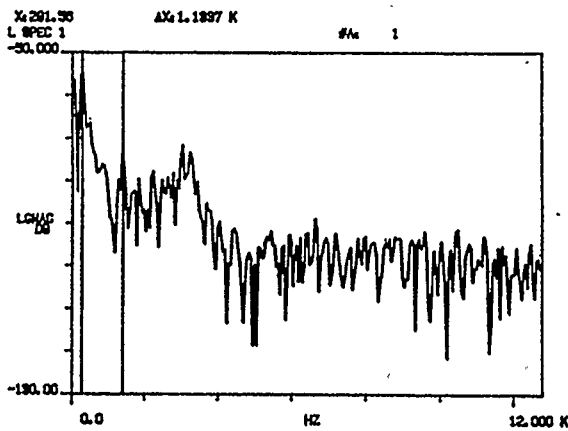
Fig. 7.27. Spectra of the intensity modulated signal with a fiber taper of $29 \mu\text{m}$ waist as a secondary strut past a $750 \mu\text{m}$ primary strut, at 633 nm light wavelength



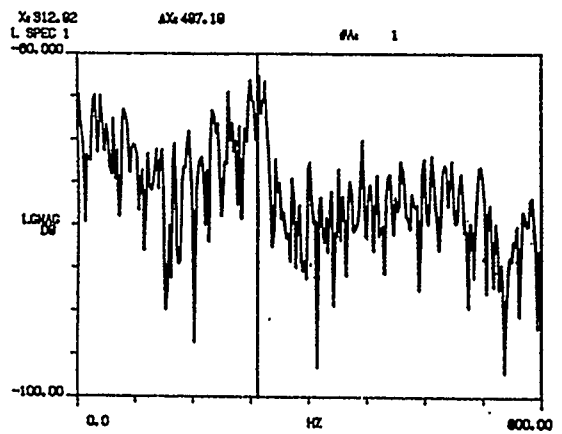
(e) $v = 0.696$ m/s



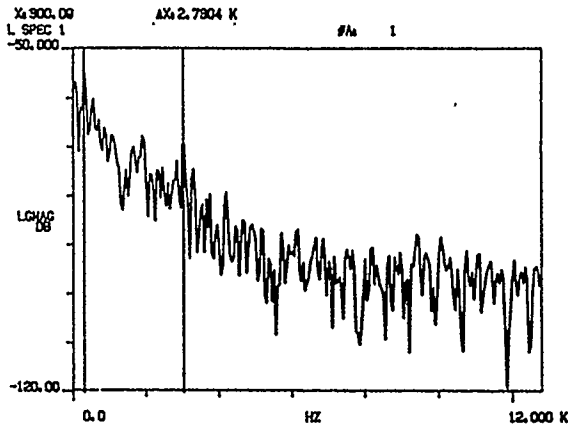
(f) $v = 0.808$ m/s



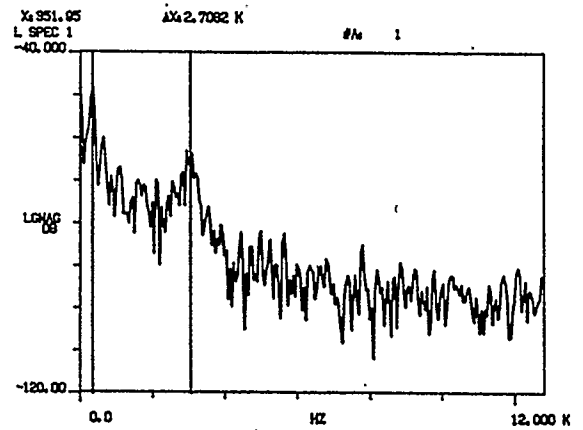
(g) $v = 0.943$ m/s



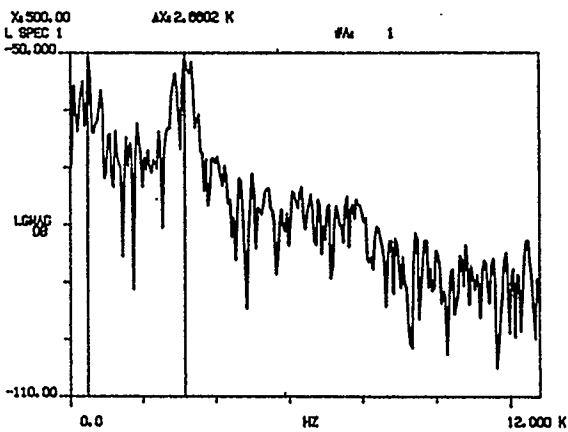
(h) $v = 1.055$ m/s



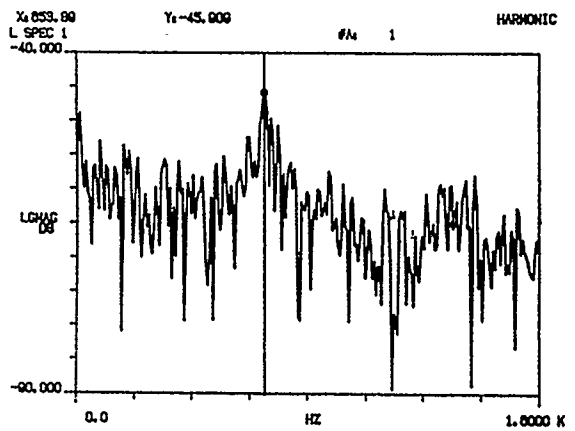
(i) $v = 1.179$ m/s



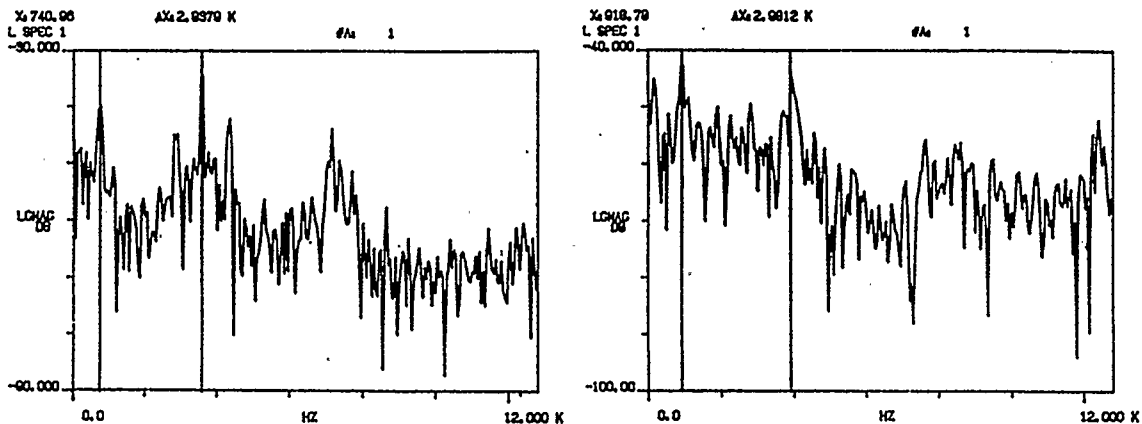
(j) $v = 1.313$ m/s



(k) $v = 1.77$ m/s



(l) $v = 2.23$ m/s



(m) $v = 2.626 \text{ m/s}$

(n) $v = 3.008 \text{ m/s}$

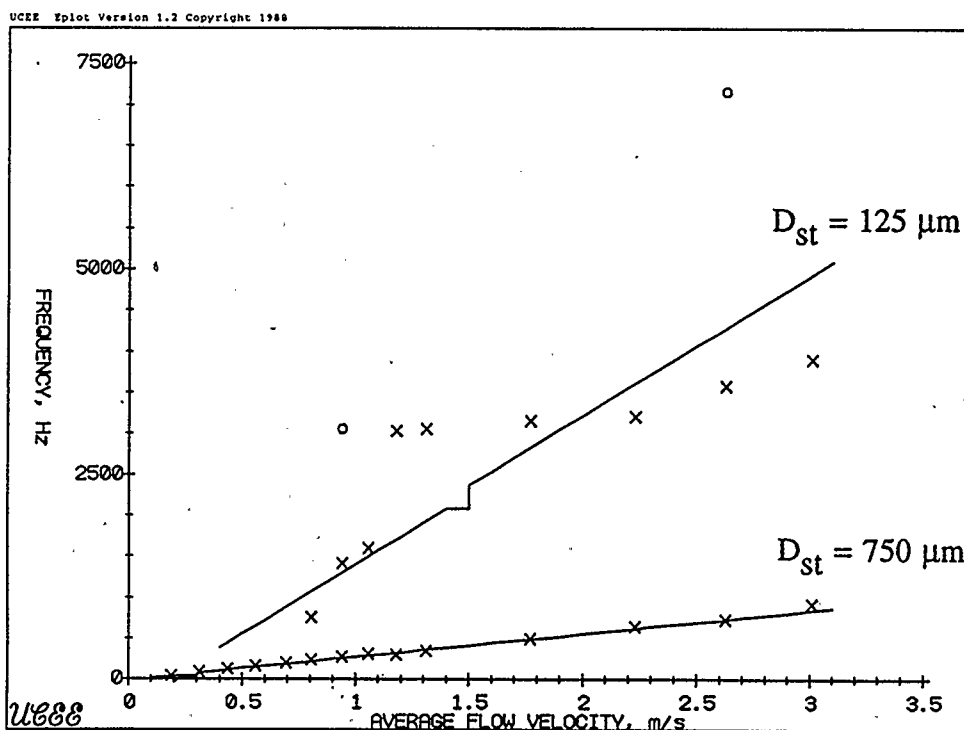


Fig. 7.28. Detected frequency peaks for Fig. 7.27 as compared to the shedding frequencies of 125 μm and 750 μm struts

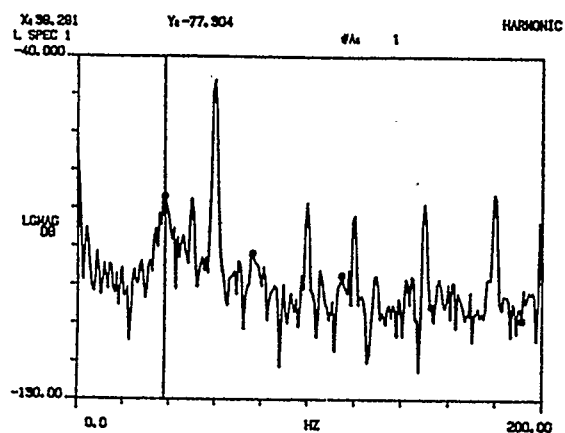
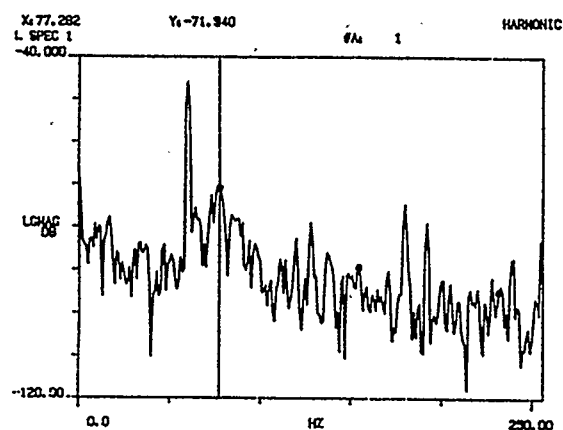
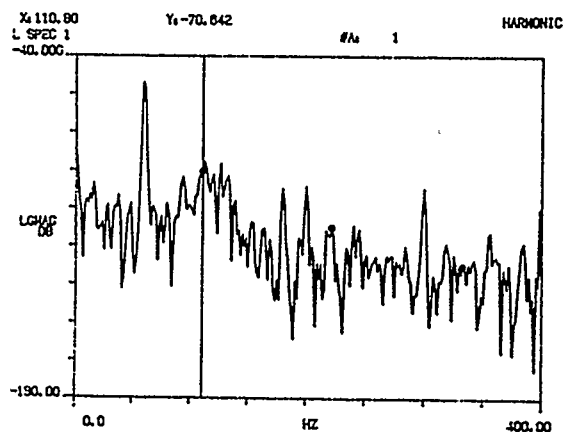
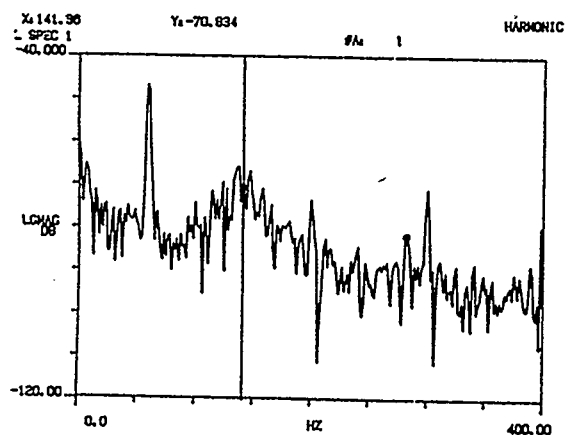
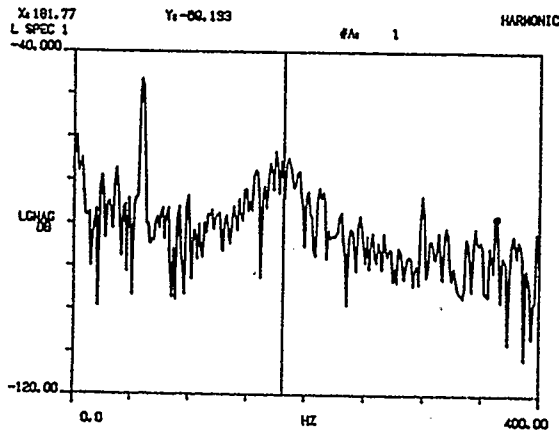
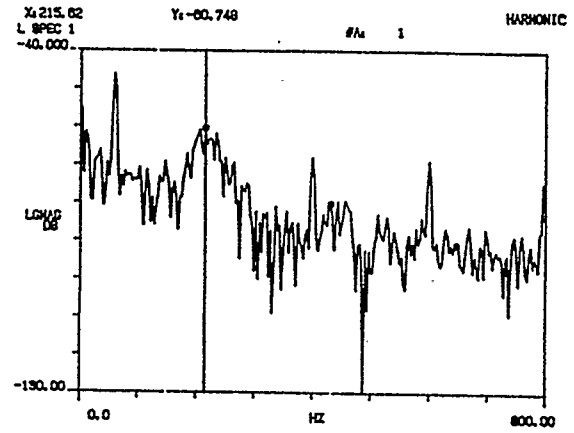
(a) $v = 0.191$ m/s(b) $v = 0.314$ m/s(c) $v = 0.438$ m/s(d) $v = 0.561$ m/s

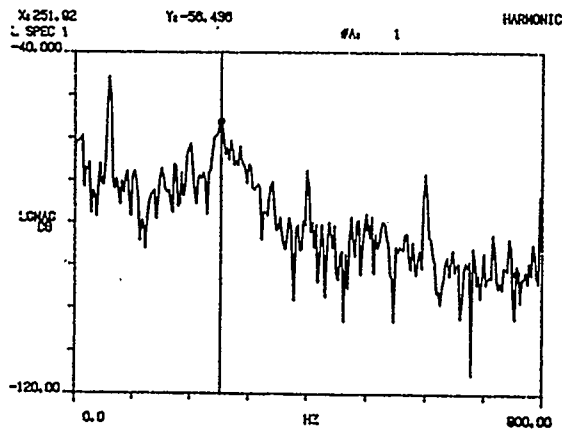
Fig. 7.29. Spectra of the intensity modulated signal with the same taper of Fig. 7.27 as a secondary strut past a 750 μm primary strut, at 1300 nm light wavelength



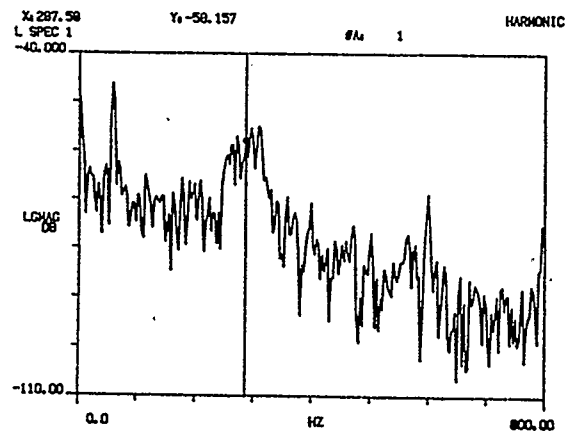
(e) $v = 0.696$ m/s



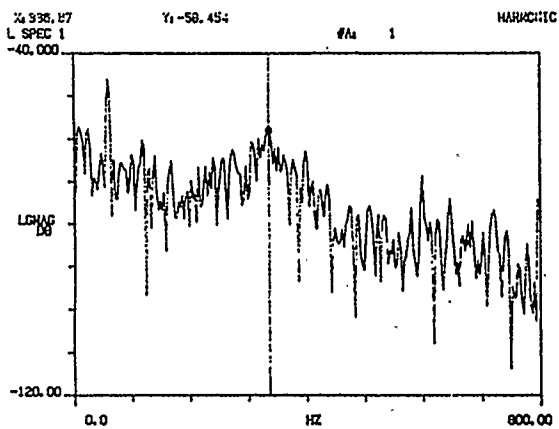
(f) $v = 0.808$ m/s



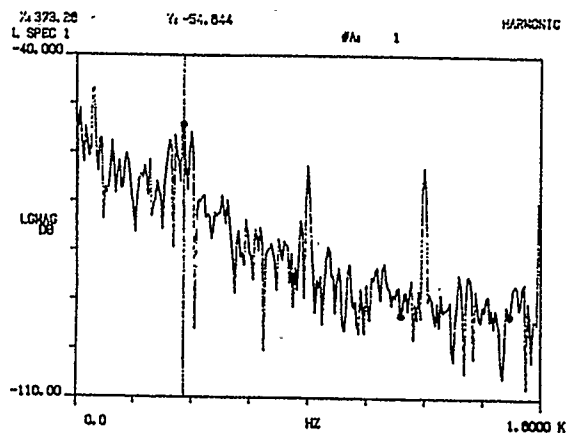
(g) $v = 0.943$ m/s



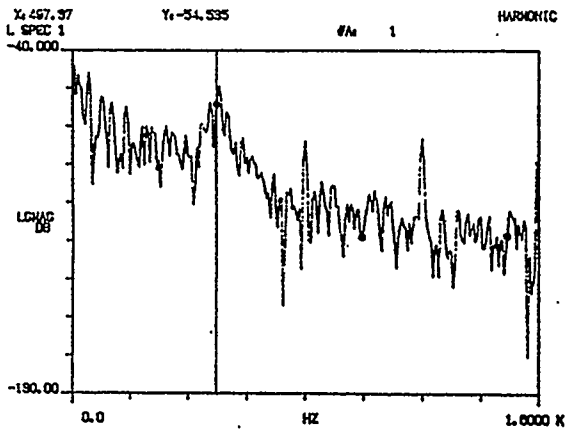
(h) $v = 1.055$ m/s



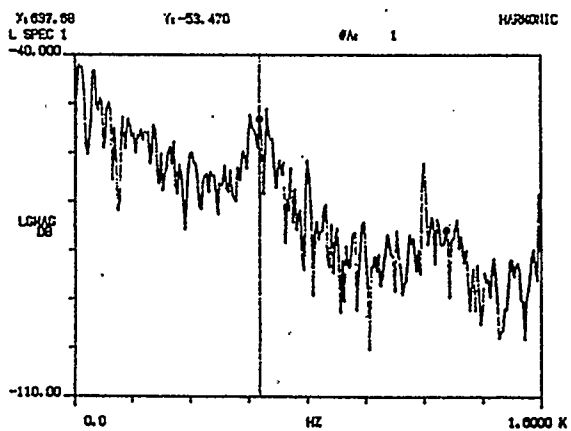
(i) $v = 1.179$ m/s



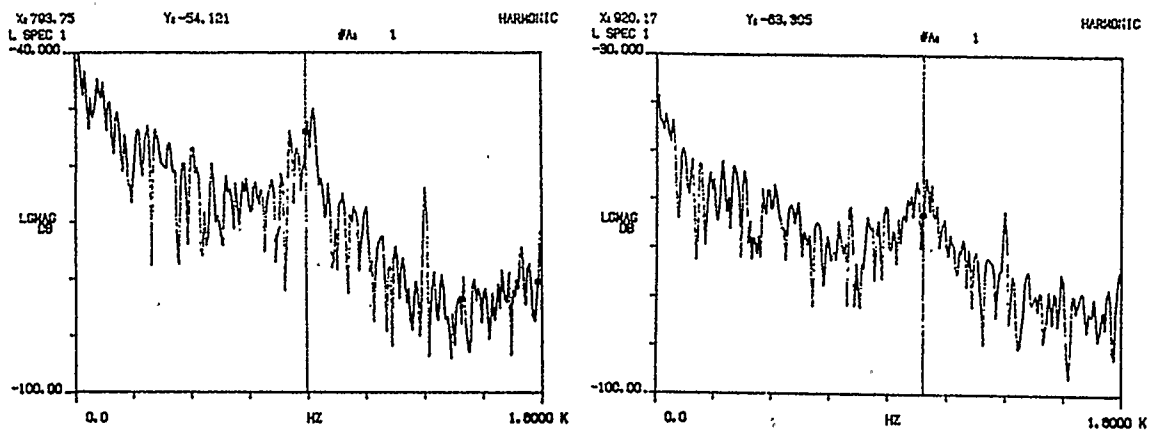
(j) $v = 1.313$ m/s



(k) $v = 1.77$ m/s



(l) $v = 2.23$ m/s



(m) $v = 2.626 \text{ m/s}$

(n) $v = 3.008 \text{ m/s}$

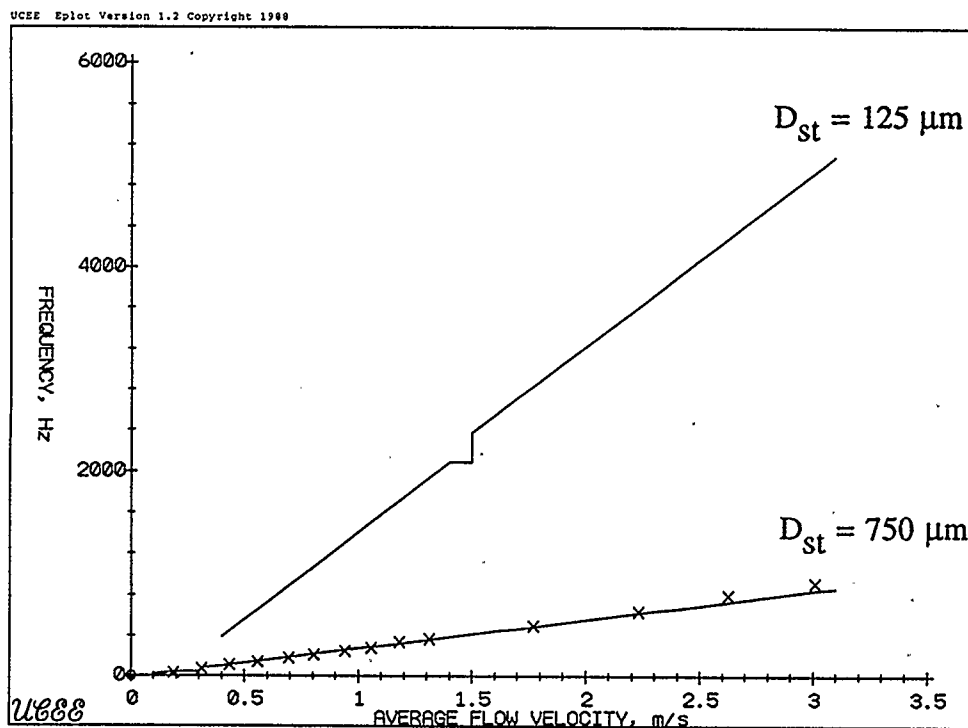


Fig. 7.30. Detected frequency peaks for Fig. 7.29 as compared to the shedding frequencies of 125 μm and 750 μm struts

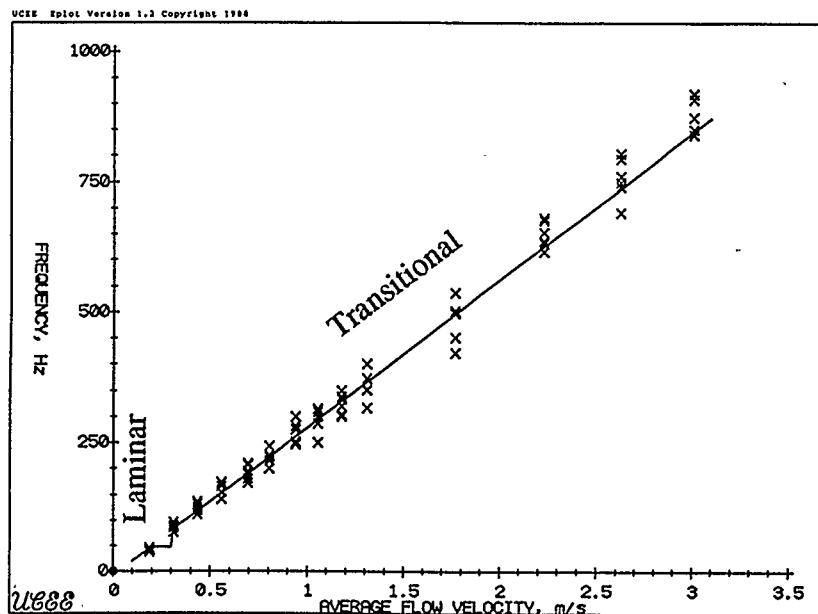


Fig. 7.31. Detected primary strut shedding frequencies with four different tapers as secondary struts at both 633 nm and 1300 nm wavelengths as compared to theoretical shedding frequencies

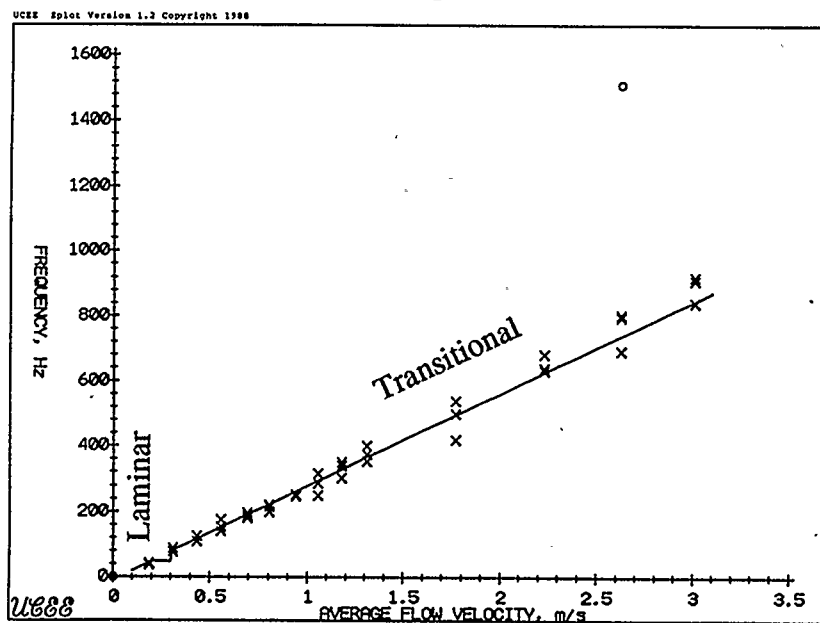


Fig. 7.32. Detected frequency peaks with three different fiber tapers as secondary struts at 1300 nm light wavelength as compared to theoretical shedding frequencies of the primary strut

Chapter 8

CONCLUSION

In this work optical fiber fluid flow rate measurement techniques were studied. Intensity modulated sensing of flow rate was experimentally investigated using an in-house fabricated flow rig and proof of concept experiments conducted on simple arrangements using fiber tapers to sense vibrations in a vortex shedding flowmeter.

Brief reviews of optical fiber sensing schemes, conventional fluid flow rate measurement techniques and optical fiber flowmeters reported in the literature were provided. Theoretical and experimental investigations of the effect of pressure on the intensity of light propagating in an exposed fiber were reported and it was concluded that a special fiber part is needed to enable the sensing of flow effects on intensity.

Fiber tapers as sensing fiber parts were studied and used in the proposed flowmeter. These tapers were made using available equipments and characterized for their transmission versus bending at two operating wavelengths where they act as multimode and single mode light guides. Single mode fiber tapers having a normalized frequency of less than unity at the taper waist were found to be the most useful for bending sensor application as they have less non-linearity and a wider range of monotonic decrease in transmission with bending. These tapers were modeled for their transmission characteristics using local normal modes and mode coupling

techniques and the simulation results compared very well to experimental taper characteristics.

Fiber tapers were installed across the flow in a test section of our rig and the resulting flowmeter was investigated experimentally at two transmission wavelengths with the fiber acting as a multimode and a single-mode guide. The shedding frequencies were detected as well as harmonics and frequency mixing products throughout the investigated flow range at the shorter wavelength where the fiber is multimode. Shedding frequencies alone were detected at the longer wavelength with a single mode fiber operation through the laminar range of vortex shedding. In both cases the shedding frequencies deviate largely from those of a rigid strut of the fiber diameter and vary widely with taper dimensions.

Fiber tapers were then used as secondary sensing struts past a rigid primary shedding strut. With this flowmeter design shedding frequencies following closely those predicted for the rigid shedding strut were detected throughout the range of flow.

Under multimode fiber operation other frequencies corresponding to vortex shedding from the fiber were detected as well as harmonics and mixing products, while under single-mode operation these were suppressed. Measurements made with different tapers gave an accuracy of about 5% in flow rate measurement which is the same figure obtained by rig calibration for the accuracy of the rotameter indication used as a reference for flow rate.

The proposed flowmeter using fiber tapers to sense vortex shedding oscillations has thus been realized and investigated and showed to be viable for flow rate measurement over a practical range of water flow speeds, from 0.3 to 3 m/s [78].

The flow rig used limited the extent of our investigations in two ways; firstly and most importantly it did not allow investigation of the full accuracy of our flowmeter. The rotameter used depends on direct flow float-position reading and it has an accuracy of 2% of full scale as reported in the accompanying literature. In calibration we obtained variations in actual flow rate of 3.3% of full flow for most of the flow range and for 70% flow this error is 5% of the indicated flow. The range of flow rates readable by the rotameter was limited by its full scale which corresponds to only 1.313 m/s. Beyond this rate the manometer reading was used to indicate the flow. Practically, one had to adjust for a flow giving the average reading wanted since the manometer reading used to vibrate around some value and particularly at higher flow rates thus deteriorating the accuracy of flow rate referencing at these rates. More accurate flowmeters with accuracies of 1% of full scale are commercially available [79] such as magnetic and vortex shedding flowmeters. A flowmeter of one of these types with extended scale would have enabled a more accurate investigation. Secondly, the range of flow was limited by the pipe sizing and pump power. A bigger rig using both 1" and 2" piping and a larger horse-power pump would allow for larger flow velocities so that the range of application of the proposed flowmeter could be determined. For future investigations, these two enhancements of the flow rig could enable a comparison of flowmeter designs using different primary shedding struts as

well as an investigation of the effect of taper dimensions on the measurement accuracy.

If fiber tapers could be made in a controllable way as now is the case for tapers used in optical couplers the flowmeter design could be optimized for taper dimensions and placement past the rigid strut. The complicated situation created when the fiber is the shedding strut could be studied and explained so as to maybe give rise to designs with only the fiber taper installed in the flowmeter.

Fiber tapers can also be used in a number of other sensors. A pressure sensor using a simple fixture and a pressure sensitive bellow, and a magnetometer using magneto-strictive material have already been reported [53, 64, 80]. A stress and crack sensor using a plexiglass block has been suggested for smart skins application [62] where such a sensor would be embedded in the skin of a large structure to monitor stresses and strains.

The program code developed for the simulation of the taper characteristics can easily be applied to other types of single-mode fiber tapers and it can also be used to simulate multimode fiber taper characteristics, if modified to include power distribution among the modes at the taper input and both core-guided and cladding-guided modes in the modal mixing within the taper. It can be applied to other waveguide tapers by including the local normal modes of these waveguides in place of those of the round fiber guide. The modal mixing technique applied in the program can also be used in a wide variety of waveguide problems including bent guides, modal transformers and waveguide-Y branches [81]. The effect of coupling to radiation

modes can be assessed by comparing with other techniques that include radiation in field presentation such as the Beam Propagation Method [82]

Multiplexing of fiber taper sensors is a very interesting issue and a number of multiplexing techniques can be applied to address and read a network of these sensors [83]. For the vortex shedding flowmeter studied in this thesis a series connection of meters can be used for a multi-point flow rate measurement along a pipeline of descending flow. This system would give frequency components corresponding to all different readings at the detecting end. Individual shedding frequencies could be identified by the apriori known relation between flow rates at different measuring sites. Wavelength and time-division multiplexing can be applied for a star-connected network of flowmeters using optical filters and high speed demultiplexers, respectively. Optical time domain reflectometry can be used for the read-out of a complex network of flowmeters provided the total duration of a scanning period is very small compared to the period of the frequency being detected by the flowmeter. This is possible since shedding frequencies lie in the low audio-frequency range. A novel multiplexing technique for intensity modulated sensors using fiber loops has recently been proposed [84] and is applicable to fiber taper sensors.

The author of this thesis wishes that at some time in the future he will be involved in further study and development on fiber optic sensors at the University of Calgary.

References

- [1] G. D. Pitt, A. M. Prabakaran, R. J. Williamson, D. Wilson and D. Batchelder, "Optical Fiber Flowmeters", Proc. 2nd Int. Conf. on Optical fiber Sensors, Liederhalle, Stuttgart, Germany, 1984, pp. 23-28.
- [2] C. A. Wade and A. Dandridge, "Fiber-Optic Coriolis Mass Flowmeter for Liquids", Electron. Lett., Vol. 24, No. 13, 1988, pp. 783-784.
- [3] J. P. Herzog, P. Rotti and P. Meyrueis, "Optical Fiber Flowmeter with Temperature Correction", Sensors and Actuators, Vol. A25-27, 1991, pp. 219-223.
- [4] B. C. B. Chu, T. P. Newson and D. A. Jackson, "An Optically Addressed Vortex Shedder Flow Meter", Proc. 7th Optical Fiber Sensors Conf., OFS'7, Sydney, Australia, 1990, pp. 179-182.
- [5] P. A. Leilabady, J. D. C. Jones, A. D. Kersey, M. Corke and D. A. Jackson, "Monomode Fibre Optic Vortex Shedding Flowmeter", Proc. 2nd Int. Conf. on Optical Fiber Sensors, Liederhalle, Stuttgart, Germany, 1984, pp. 35-38.
- [6] J. H. Lyle and C. W. Pitt, "Vortex Shedding Fluid Flowmeter Using Optical Fiber Sensor", Electron. Lett, Vol. 17, No. 6, 1981, pp. 244-245.
- [7] J. W. Berthold, "Industrial Applications of Fiber Optic Sensors", Fiber Optic and Laser Sensors III, E.L. Moore and O.G. Ramer, Editors, Proc. SPIE 566, 1985, pp. 37-45.
- [8] E. Udd, "Fiber Optic Sensors, An Introduction for Engineers and Scientists", John Wiley & Sons, New York, 1991.

- [9] R. P. De Paula and E. L. Moore, " Fiber Optic Sensor Overview ", Fiber Optic and Laser sensors III, E.L. Moore and O.G. Ramer, Editors, Proc. SPIE 566, 1985, pp. 2-17.
- [10] F. Bucholtz, and A. M. Yurek, " Fiber interferometric sensors: Technology and applications ", Optics news Nov.1989, pp. 20-27
- [11] R. H. Stolen and R. P. DePaula, " Single - Mode Fiber Components" , Proc. IEEE, Vol. 75, No. 11, 1987, pp. 1498-1511.
- [12] T. Okoshi," Polarisation-state control schemes for heterodyne or homodyne optical fiber communications ", J. Lightwave Tech., Vol. LT-3, No. 6, 1985, pp. 1232-1236.
- [13] A. D. Kersey, A. Dandridge, and W.K. Burns," Fiber optic gyroscope technology ", Optics news Nov. 1989, pp. 12-19.
- [14] T. P. Lee, and C. Zah," Wavelength-tuneable and single-frequency semiconductor lasers for photonic communications networks ", IEEE Comm.Mag. Oct.1989, pp. 42-52.
- [15] N. Lagakos, T. R. Hickman, P. Ehrenfeuchter, J. A. Bucaro and A. Dandridge, "Planar Flexible Fiber Optic Acoustic Sensors", J. Lightwave Tech., Vol. LT-8, No. 9, 1990, pp. 1298-1303.
- [16] N. Lagakos and W. Trott, " Microbend Fiber Optic Sensor as Extended Hydraophone", IEEE J. Quantum Electron., Vol. QE-18, No. 10, 1982, pp. 1633-1638.
- [17] N. Lagakos, J. H. Cole, and J. A. Bucaro, " Microbend Fiber Optic Sensor ", Appl. Optics, vol. 26, No. 11, 1987, pp. 2171-2180.

- [18] F. Durst, " Discharge Measuring Methods in Pipes ", Discharge and velocity measurements, A. Muller, Editor, Balkema and Rotterdam, Netherlands, 1988, pp.3-15.
- [19] R. L. Daugherty and A. C. Engersoll, " Fluid Mechanics With Engineering Applications ", McGraw Hill, New York, 1954.
- [20] A. J. Macfadyen and B. R. Jennings, " Fiber-Optic Systems for Dynamic Light Scattering - a review", Optics and Laser Technology, Vol.22, No.3, 1990, pp. 175-187.
- [21] D. Kilpatrick, J. V. Tyberg and W. W. Parmley, "Blood Velocity Measurement by Fiber-Optic Laser Doppler Anemometry", IEEE Trans. Bio-Med. Eng., Vol.29, 1982, pp.142-145.
- [22] J. J. Peters, " Field Measurement of Discharge and Velocity ", Discharge and velocity measurements, A. Muller, Editor, Balkema and Rotterdam, Netherlands, 1988, pp.179-185.
- [23] F. Durst, " Alternative Measuring Techniques and New Developments ", *ibid*, pp.187-207.
- [24] T. Tanaka and G. B. Benedek, "Measurement of the velocity of Blood flow (in vivu) using a fiber optic catheter and optical mixing spectroscopy", Appl. Optics, Vol. 14 , No. 1, 1975, pp. 189-196.
- [25] K. Kyuma, S. Tai, K. Hamanaka and M. Nunoshita, "Laser Doppler Velocimeter with a Novel Fiber Probe", Appl. Optics, Vol. 20, No. 14, 1981, pp. 2424-2427.
- [26] K. Kyuma, K. Kojima, M. Nunoshita and T. Nakayama, "Signal Enhancement of a Fiber-Optic LDV using a High Power Ar-Ion Laser Oscillating in Multi-Longitudinal Modes", Proc. 2nd Int. Conf. on Optical fiber Sensors, Liederhalle, Stuttgart, Germany, 1984, pp. 39-42

- [27] H. Toda, M. Haruna and H. Nishihara, "Optical Integrated Circuit for a Fiber Laser Doppler Velocimeter", *J. Lightwave Tech.*, LT-5, No. 7, 1987, pp. 901-905
- [28] R. Battig, R. Stierlin, P. D. Henchoz and H. P. Weber, "New Monostatic Balanced Doppler Velocimeter Using a High Birefringence Fiber", *J. Lightwave Tech.*, Vol. LT-6, No. 1, 1988, pp. 8-11.
- [29] W. Boyle, A. Palmer, K. Grattan and B. Meggitt, "A Fluid Flow Measuring System Using Low Coherence Optical Fiber Doppler Anemometry", *Proc. 7th Optical Fiber Sensors Conference, OFS'7, Sydney, Australia, 1990*, pp. 357-360.
- [30] E. N. Goodyer, "Novel Sensors for Measuring Fuel Flow and Level" In-*Process Optical Measurements*, K.H. Spring, Editor, *Proc. SPIE 1012*, 1989, pp. 150-154.
- [31] R. J. G. Carr, "Fiber Optic Sensors for the characterization of Particle Size and Flow Velocity", *Sensors and Actuators*, Vol. A 21-23, 1990, pp. 1111-1117.
- [32] P. R. Ball, B. Culshaw and S. A. Kingsley, "Recovery of Phase Modulated Signals in Multimode Optical Fibers", *Proc. Int. Optical Computing Conf., SPIE Vol 232*, 1980, pp. 216-223.
- [33] G. B. Hocker, "Fiber-Optic Sensing of Temperature and Pressure", *Appl. Optics*, Vol. 18, No. 9, 1979, pp. 1445-1448.
- [34] V. S. Sudarshanam and K. Srinivasan, "Static Phase Change in a Fiber Optic Coil Hydrophone", *Appl. Optics*, Vol. 29, No. 6, 1990, pp. 855-863.
- [35] A. Bertholds and R. Dandliker, "Determination of the Individual Strain-Optic Coefficients in Single-Mode Optical Fibers", *J. Lightwave Tech.*, Vol. LT-6, No. 1, 1988, pp. 17-20.

- [36] B. Budiansky, D. C. Drucker, G. S. Kine, and J. R. Rice, "Pressure Sensitivity of a clad Optical Fiber", *Appl. Optics*, Vol. 18, No. 24, 1979, pp. 4085-88.
- [37] R. Hughes and J. Jarzynski, "Static Pressure Sensitivity Amplification in Interferometric Fiber-Optic Hydrophones", *Appl. Optics*, Vol. 19, No. 1, 1980, pp. 98-107.
- [38] J. Gowar, "Optical Communication Systems", Prentice Hall, New Jersey, 1984.
- [39] W. P. Mason, Editor, "Physical Acoustics, Principles and Methods; Vol. XVI", Academic Press, New York, 1982.
- [40] R. I. MacDonald and B. E. Swekla, "Frequency Domain Optical Reflectometer using a Ga As Optoelectronic Mixer", *Appl. Optics*, Vol. 29, No. 31, 1990, pp. 4578-82.
- [41] R. Bohm and R. Ulrich, "High Accuracy Fiber Optic Refractometer for Fluids", *Proc. 7th Optical Fiber Sensors Conf., OFS '7, Sydney, Australia, 1990*, pp. 353-356.
- [42] G. D. Fraser and R. I. MacDonald, "A Swept Frequency Remote Refractometer for Liquids", Private Correspondence, 1990.
- [43] A. E. Perry, M. S. Chang and T. Lim, "The Vortex Shedding Process Behind Two Dimensional Bluff Bodies", *J. Fluid Mechanics*, Vol. 116, 1982, pp. 77-90.
- [44] B. S. Massey, "Mechanics of Fluids", Von Nostrand Reinhold, London, 1970.
- [45] C. H. K. Williamson, "Defining a Universal and Continuous Strouhal-Reynolds number relationship for the Laminar Vortex Shedding of a Circular Cylinder", *Phys. Fluids*, Vol. 31, No. 10, 1988, p.2742-44.
- [46] A. Roshko, "On the Development of turbulent wakes from Vortex Streets", *Natl Advisory Comm. Aeronaut.*, TN 1191, 1954. See also Ref [51].

- [47] A. Richter and E. Naudascher, "Fluctuating Forces on a Rigid Circular Cylinder in Confined Flow ", J. Fluid Mechanics, Vol. 78 part 3, 1976, pp.561-576.
- [48] D. W. Sallet, " The Drag and Oscillating Transverse Force on Vibrating Cylinders due to Steady Fluid Flow ", Ingenieur Archiv, Vol. 44, 1975, pp. 113-122.
- [49] W. D. Iwan, " The Vortex Induced Oscillation of Elastic Structural Elements ", Trans. ASME, J. Eng. for Industry, Nov.1975, pp. 1378-82.
- [50] W. D. Iwan and R. D. Blevins, "A Model for Vortex Induced Oscillation of Structures ", J. Appl. Mech., Sept.1974, pp. 581-586.
- [51] D. Gerich and H. Eckelmann, " Influence of End Plates and Free Ends on the Shedding Frequency of Circular Cylinders ", J. Fluid Mechanics, Vol. 122, 1982, pp. 109-121
- [52] B. R. Noack, F. Ohle and H. Eckelmann, " On Cell Formation in Vortex Streets " J. Fluid Mechanics, Vol. 227, 1991, pp. 293-308.
- [53] L. C. Bobb, H. D. Krumboltz and P. M. Shankar, "Pressure sensor that uses Bent Biconically Tapered Single-Mode Fibers", Optics Lett., Vol. 16, No. 2, 1991, pp. 112-114.
- [54] A. W. Snyder, "Coupling of Modes on a Cylindrical Tapered Dielectric Rod", Proc. IEEE, Apr. 1968, pp. 737-739.
- [55] D. Marcuse, "Mode conversion in Optical Fibers with Monotonically Increasing Core Radius", J. Lightwave Tech., Vol. LT-5, No. 1, 1987, pp. 125-133.
- [56] N. Amitay and H. M. Presby", Optical Fiber Up-Taper Modelling, and Performance Analysis", J. Lightwave Tech., Vol. LT-7, No. 1, 1989, pp. 131-137.

- [57] N. Amitay, H. M. Presby, F. V. Dimarcello and K. T. Nelson, "Single Mode Optical Fiber Tapers for Self-Aligned Beam Expansion", *Electron. Lett.*, Vol. 22, 1986, pp. 702-703.
- [58] N. Amitay, H. M. Presby, F. V. Dimarcello and K. T. Nelson, "Optical Fiber Tapers, A Novel Approach to Self-Aligned Beam Expansion and Single Mode Hardware", *J. Lightwave Tech.*, Vol. LT-5, No. 1, 1987, pp. 70-76.
- [59] K. P. Jedrzejewski, F. Martinez, J. D. Minelly, C. D. Hussey and F. P. Payne, "Tapered Beam Expander for Single Mode Optical Fiber Gap Devices", *Electron. Lett.*, Vol. 122, No. 2, 1986, pp. 105-106.
- [60] A. C. Boucouvalas and G. Georgiou, "A Method of Beam Forming, and Fabricating Optical Fiber Gap Devices", *Proc. Euro. Conf. Opt. Comm.*, Barcelona, Spain, 1986, pp. 361-364.
- [61] I. Andonovic and D. Uttamchandani, "Principles of Modern Optical Systems", Artech House, Norwood, MA, 1989.
- [62] P. Raiti, "Fiber Optic Sensors for Smart Skins Applications", *SPIE Vol. 1370, Fiber Optic Smart Structures and Skins III*, 1990, pp. 6-19.
- [63] A. H. Cherin, "An Introduction to Optical Fibers", McGraw Hill, New York, 1983.
- [64] L. C. Bobb, P. M. Shankar and H. D. Krumboltz, "Bending Effects in Biconically Tapered Single-Mode Fibers", *J. Lightwave Tech.*, Vol. 8, No. 7, 1990, pp. 1084-1090.
- [65] D. T. Cassidy, D. C. Johnston and K. O. Hill, "Wavelength-Dependent Transmission of Monomode Optical Fiber Tapers", *Appl. Optics*, Vol. 24, No. 7, 1985, pp. 945-950.

- [66] D. Marcuse, "Theory of Dielectric Optical Waveguides", Academic Press, New York, 1974.
- [67] A. W. Snyder, "Coupling of Modes on a Tapered Dielectric Cylinder", IEEE Trans. on Microwave Theory and Tech., Vol. MTT-18, No. 7, 1970, pp. 383-392.
- [68] A. W. Snyder, "Radiation Losses Due to Variations of Radius on Dielectric or Optical Fibers", IEEE Trans. Microwave Theory and Tech., Vol. MTT-18, No. 9, 1970, pp. 608-615.
- [69] H. F. Taylor, "Power Loss at Directional Change in Dielectric Waveguides", Appl. Optics, Vol. 13, No. 3, 1974, pp. 642-647.
- [70] H. F. Taylor, "Bending Effects in Optical Fibers", J. Lightwave Tech. Vol. LT-2, No. 5, 1984, pp. 617-628.
- [71] P. M. Shankar, L. C. Bobb, and H. D. Krumboltz, "Coupling of Modes in Bent Biconically Tapered Single-Mode Fibers", J. Lightwave Tech., Vol. 9, No. 7, 1991, pp. 832-836.
- [72] D. Marcuse, "Radiation Losses of the Dominant Mode in Round Dielectric Waveguides", Bell Sys. Tech. J., Oct. 1979, pp. 1665-1693.
- [73] P. J. B. Clarricoats and K. B. Chan, "Propagation Behaviour of Cylindrical-Dielectric Rod Waveguides", Proc. IEE, Vol. 120, No. 11, 1973, pp. 1371-1378.
- [74] A. W. Snyder and J. D. Love, "Optical Waveguide Theory", Chapman and Hall, New York, 1983
- [75] A. H. Morshed and D. Irvine - Halliday, "Fiber Optic Vortex Shedding Flowmeter", Selected for presentation at the 11th Symp. Eng. Appl. Mech., Regina, Saskatchewan, May 11-13, 1992.

- [76] P. A. Eibeck, "An Experimental Study of the Flow Downstream of a Circular and Tapered Cylinder", *J. Fluids Engineering*, Dec. 1990, Vol. 112, pp. 393-401.
- [77] H. Sakamoto and H. Haniu, "A Study on Vortex Shedding From Spheres in a Uniform Flow", *Trans. ASME*, Vol. 112, Dec. 1990, pp. 386-392.
- [78] A. H. Morshed and D. Irvine - Halliday, "Intensity Modulated Optical Fiber Vortex Shedding Flowmeter", To be submitted to *Electron. Lett.*
- [79] "The flow and Level Handbook", Omega Technologies Inc., 1991 Catalog.
- [80] L. C. Bobb, H. D. Krumboltz and P. M. Shankar, " An Optical Fiber Alternating - Gradient Magnetometer ", *Proc. 8th Optical Fiber Sensors Conf., OFS'8*, Monterey, California, 1992, pp. 410-413.
- [81] A. B. Buckman, " Guided - Wave Photonics ", Saunders College Publishing, Toronto, 1992.
- [82] A.H. Morshed, " S-Shaped Etalon Single Mode Semiconductor Laser ", M.Sc. Thesis, Ain Shams University, Cairo, Egypt, 1989.
- [83] B. Culshaw, " Distibuted and Multiplexed Fiber Optic Sensor Systems ", *Optical Fiber Sensors*, A.N. Chester, S. Martelluci and A.M. Scheggi, Editors, Martinus Nijhoff Publishers, Dordrecht, 1987.
- [84] R. I. MacDonald and R. Nychka, " A Differential Measurement Technique for Optical Fiber Sensors Using Intensity Modulation ", *Proc. 8th Optical Fiber Sensors Conf., OFS'8*, Monterey, California, 1992, pp. 301-304.

Appendix

Table A.1. Rig calibration data

Rotameter reading %	Actual flow, Kg / min = 1.0236 Lit / min	Pressure at test piece, psi
5	1.81, 1.9	30
10	5.382, 5.55	
11	5.95, 5.917,	29.7, 29.9
	5.89	
19.5	9.135,	29.2, 29.7
	9.47,	29.5, 29.7
	9.231	
30	13.2867	
38.1	16.129, 15.984,	29
	16.03	28.3
50	20.192,	28.3
	20.652, 20.357	27.8
58	23.026,	27.6
	23.388,	27.3, 27.8
	23.56	26.7, 27.8
70	27.344,	27
	27.778	26
77.5	31.82	
80	31.25,	25.7
	31.14	26
87	33.33,	25
	34, 33.02, 32.7, 34.09	
90	34.722, 35,	25
	34.6154	24.7
100	39.474, 38.571	23.9
	52.679, 52.08, 52.381	20
	67.1, 65, 65.625	15
	79.74, 76.316	10
	87.719, 88.983	5
	93.182, 91.98	3.5